FINITE ELEMENT ANALYSIS OF STRESS CONCENTRATION IN TUBULAR T-JOINTS

Final Report

by

M. Arockiasamy, P.Eng.
G.S. Bhuyan
K. Munaswamy

DSS CONTRACT OSU 83-00033

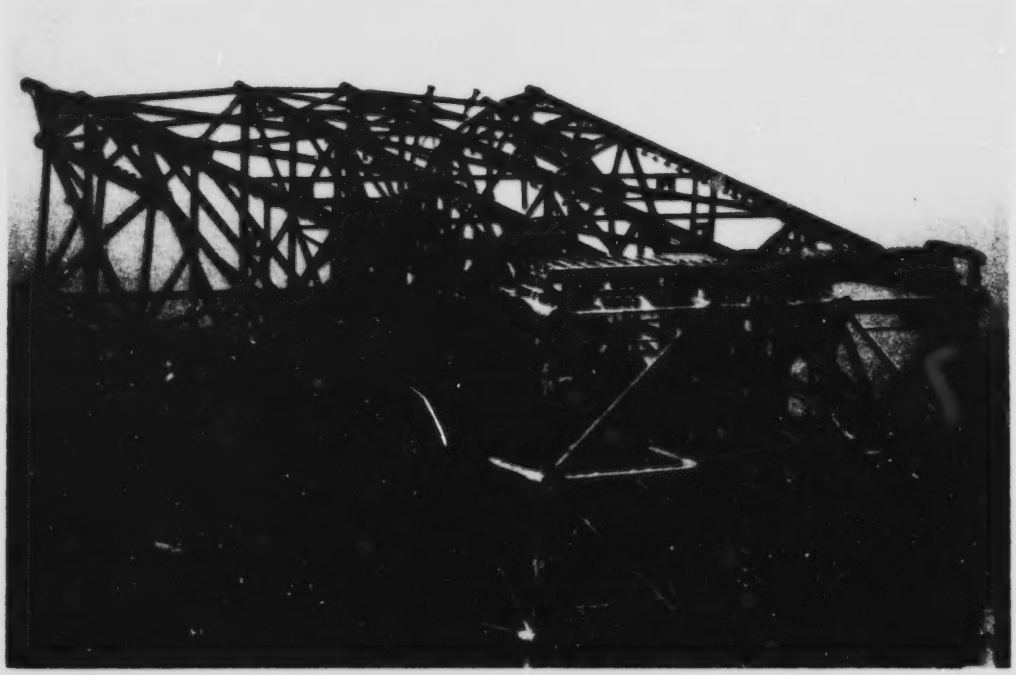

Faculty of Engineering and Applied Science
Memorial University of Newfoundland
St. John's, Newfoundland, Canada A1B 3X5

December 1984

FINITE ELEMENT ANALYSIS OF STRESS CONCENTRATION IN TUBULAR T-JOINTS

Final Report

by

M. Arockiasamy, P.Eng.
Associate Professor of Engineering

G.S. Bhuyan
Graduate Student

K. Munaswamy
Post-doctoral Fellow

Faculty of Engineering and Applied Science
Memorial University of Newfoundland
St. John's, Newfoundland, Canada A1B 3X5

Work on this project was conducted under the auspices of the Canada Centre for Mineral and Energy Technology, Energy, Mines and Resources, Canada.

DSS FILE NUMBER: 24 SU. 23440-3-9055

DSS CONTRACT SERIAL NUMBER: OSU 83-00033

CANMET PROJECT NUMBER: 23440

CANMET SCIENTIFIC AUTHORITY: Dr. O. Vosikovsky

143pp

December 1984

This report should be cited as Contract Report No. OSU83-00033

DISCLAIMER

All opinions expressed in this report are those of the authors and should not be considered to represent the position of CANMET or the Department of Energy, Mines and Resources.

ABSTRACT

The report describes the analytical investigation of stress distribution in tubular T-joint for axial and in-plane bending load cases. The results of the study on distribution of surface stresses along the brace-chord intersection, including through-thickness variation and hot spot stress concentration factors are presented and compared with those reported in the literature. The effect of shallow weld toe cracks (both hair-line crack and crack depth equal to half the chord wall thickness) on stress redistribution are discussed.

ACKNOWLEDGEMENTS

The financial support received from Canada Centre for Mineral and Energy Technology, Department of Energy, Mines and Resources, Ottawa, is gratefully acknowledged. Special thanks are due to Dr. Vosikovsky for his helpful suggestions, discussions and constructive criticism. The authors thank Prof. G. Ross Peters, Dean, Faculty of Engineering and Applied Science, Memorial University of Newfoundland for his continued interest and encouragement. The partial support provided by the Natural Sciences and Engineering Research Council of Canada Grant A1799 is gratefully acknowledged. The generous support from VAX 11/780 computing services at Memorial University is very much appreciated. Grateful acknowledgement is due to Mrs. Marilyn Warren and Mrs. Levinia Vatcher for the considerable care and patience in typing the manuscript.

CONTENTS

	Page
TITLE	i
DISCLAIMER	ii
ABSTRACT	iii
ACKNOWLEDGEMENTS	iv
CONTENTS	v
LIST OF TABLES	vii
LIST OF FIGURES	viii
NOMENCLATURE	xii
CHAPTER I	
INTRODUCTION	1
1.1 Background	1
1.2 Scope	3
1.3 Outline of the Project	3
1.3.1 Two dimensional finite element stress analysis	4
1.3.2 Three dimensional finite element stress analysis	4
1.3.3 Three dimensional finite element stress analysis with shallow weld toe crack	4
CHAPTER II	
LITERATURE REVIEW	6
2.1 Analytical Investigation	6
2.1.1 Introduction	6
2.1.2 Discretization of the joint	7
2.1.3 Stress analysis	8
2.1.4 Finite element analysis of crack problems	10
CHAPTER III	
TWO DIMENSIONAL FINITE ELEMENT ANALYSIS	13
3.1 Mesh Generation	13
3.2 Element Stiffness Formulation	15

		Page
3.2.1	Plate bending element	18
3.2.2	Membrane element	23
3.2.3	Assembly of six degrees of freedom	25
3.3	2-Dimensional Results and Discussions	28
3.3.1	General	28
3.3.2	Chord stresses	34
3.3.3	Brace stresses	47
	CHAPTER IV	
	THREE DIMENSIONAL STRESS ANALYSIS INCLUDING REZONE TECHNIQUE	54
4.1	Introduction	54
4.2	Modelling of the Entire T-joint	54
4.2.1	Element stiffness formulation	54
4.3	Modelling of Hot Spot Region Using Rezone Technique	60
4.3.1	Introduction	60
4.3.2	Rezone sections	62
4.4	Results and Discussions	79
4.4.1	General	79
4.4.2	Entire joint analysis	84
4.4.3	Rezoned analysis	98
	CHAPTER V	
	STRESS DISTRIBUTION AROUND SHALLOW CRACK NEAR THE WELD TOE	101
5.1	Introduction	101
5.2	Formulation of Singular Element	101
5.3	Discretization of the Crack Region	105
5.4	Results and Discussions	105
	CHAPTER VI	
	CONCLUSIONS	122
	REFERENCES	

LIST OF TABLES

Table		Page
3.1	Joint Parameters	29
3.2	Stress Concentration Factors	35
3.3	Hot Spot Stress Concentration Factors	85

LIST OF FIGURES

Figure		Page
3.1	Regions of T-Joint Model for Mesh Generation	14
3.2	Node Numbering Sequences	16
3.3	Rotation of Coordinate System Axes for Mesh Generation	17
3.4	Triangular Area Coordinate	19
3.5	Bending Element	21
3.6	Membrane Element	24
3.7	Assembly of Six-degrees of Freedom	26
3.8	Assembly of Triangular Elements to form Quadrilateral Element	30
3.9	Schematic of T-Joint Model	31
3.10	Finite Element Mesh for Different Regions	32
3.11	Finite Element Mesh Generation for the Joint	33
3.12	Deformed Joint due to Axial Compressive Load	36
3.13	Deformed Joint due to In-plane Bending Load	37
3.14	Characteristic Lines of the Joint	38
3.15	Principal Stress Distribution: brace, line 1	39
3.16	Principal Stress Distribution: brace, line 1	40
3.17	Principal Stress Distribution: brace, line 2	41
3.18	Principal Stress Distribution: brace, line 2	42
3.19	Principal Stress Distribution: chord, line 3	43
3.20	Principal Stress Distribution: chord, line 3	44
3.21	Principal Stress Distribution: chord, line 4	45
3.22	Principal Stress Distribution: chord, line 4	46
3.23	Schematic of Displacements on the Plane of Symmetry	48

Figure		Page
3.24	Modified Principal Stress Distribution after Axial Shifting: Brace, line 1	50
3.25	Modified Principal Stress Distribution after Axial Shifting: Brace, line 2	51
3.26	Modified Principal Stress Distribution after Axial Shifting: Brace, line 2	52
3.27	Modified Principal Stress Distribution after Axial Shifting: Brace, line 2	53
4.1	Three Dimensional 8-Node Element	55
4.2	6-Node Prism Element	61
4.3	Rezone Section at Saddle Point	63
4.4	Rezone Section at Crown Point	64
4.5	Plate-to-Solid Element Transition	65
4.6	Expanded View of Plate-to-Solid Element Transition	66
4.7	Definition of Surface Normal for a Cylindrical Surface	67
4.8	Shell Surface Local Coordinate System Definition	69
4.9	Translation of Surface Node due to Rotation of Plate Node about Y-Axis	70
4.10	Translation of Surface Node due to Rotation of Plate Node about Z-Axis	72
4.11	Forces Transformed to Local Shell Surface Coordinate System	74
4.12	Use of Spherical Trigonometry to Solve for Azimuth Angle b	76
4.13	Modelling of Weld at Chord/Brace Intersection	80
4.14a	3-Dimensional Finite Element Mesh for the Joint with Plug	81
4.14b	3-Dimensional Finite Element Mesh for the Joint without Plug	82

Figure		Page
4.15	3-Dimensional Finite Element Mesh for Rezoned Section of the Joint at Saddle Point	83
4.16a	Maximum Surface Stress Variation at Saddle Point due to Axial Load	86
4.16b	Stresses Along Line 4 [Ref. 38]	87
4.16c	Stresses Along Line 2 [Ref. 38]	88
4.16d	Transverse Midsection Strain Levels for the Texgap - 3D Solutions [Ref. 39]	90
4.16e	Strain Distribution along Line-4 due to Axial Load	91
4.16f	Strain Distribution along Line-2 due to Axial Load	92
4.17	Stress Distribution Across the Weld and Brace Wall at Saddle Point due to Axial Load	93
4.18	Maximum Surface Stress Variation at Crown Point due to Axial load	94
4.19	Stress Distribution Across the Weld and Brace Wall at Crown Point due to Axial Load	95
4.20	Maximum Surface Stress Variation at Crown Point due to In-plane Bending Load	96
4.21	Stress Distribution Across the Weld and Brace Wall at Crown Point due to In-plane Bending Load	97
4.22	Comparison of Entire Joint Model and Rezoned Section Analyses Results Along Line-4	99
4.23	Comparison of Entire Joint Model and Rezoned Section Analyses Results Along Line-2	100
5.1	Singular Wedge Element	102
5.2	Various Singular Elements Developed to Model Crack Front Region	104
5.3	Schematic Arrangement of Three Types of Element Around Crack Front (Cross Section of the Shell around Crack Region)	106
5.4	Finite Element Discretization of the Region in front of the Weld Toe Crack	107

Figure		Page
5.5a	Stress Variation Along Chord Surface at Saddle Point in Presence of Shallow Weld Toe Crack due to Axial Load (Without Plug)	109
5.5b	Stress Variation Along Chord Surface at Saddle Point in Presence of Shallow Weld Toe Crack due to Axial Load (With Plug)	110
5.6a	Stress Variation Along Brace Surface at Saddle Point in Presence of Shallow Weld Toe Crack due to Axial Load (Without Plug)	111
5.6b	Stress Variation Along Brace Surface at Saddle Point in Presence of Shallow Weld Toe Crack due to Axial Load (With Plug)	112
5.7a	Through Thickness Stress Variation in front of Shallow Weld Toe Crack at Saddle Point due to Axial Load (Without Plug)	113
5.7b	Through Thickness Stress Variation in Front of Shallow Weld Toe Crack at Saddle Point due to Axial Load (With Plug)	114
5.8a	Stress Variation along Chord Surface at Crown Point in Presence of Shallow Weld Toe Crack due to In-plane Bending Load (Without Plug)	116
5.8b	Stress Variation Along Chord Surface at Crown Point in Presence of Shallow Weld Toe Crack due to In-Plane Bending Load (With Plug)	117
5.9a	Stress Variation along Brace Surface at Crown Point in Presence of Shallow Weld Toe Crack due to In-plane Bending Load (Without Plug)	118
5.9b	Stress Variation Along Brace Surface at Crown Point in Presence of Shallow Weld Toe Crack due to In-Plane Bending Load (With Plug)	119
5.10a	Through Thickness Stress Variation in front of Shallow Weld Toe Crack at Crown Point due to In-plane Bending Load (Without Plug)	120

Figure		Page
5.10b	Through Thickness Stress Variation in Front of Shallow Weld Toe Crack at Crown Point due to In-Plane Bending Load (With Plug)	121

NOMENCLATURE

$[D]$	Elasticity matrix
E	Young's modulus of elasticity
F_x, F_y, F_z	Forces at plate nodes at transition
F_{xi}, F_{yi}, F_{zi}	Forces at inner surface nodes of solid elements at transition
F_{xo}, F_{yo}, F_{zo}	Forces at outer surface nodes of solid element at transition
$\{f\}$	Force vector
$\{f_b\}$	Flexural force vector
$\{f_m\}$	Membrane force vector
g_j	Incompatible shape function
K_I, K_{II}, K_{III}	Stress intensity factors
$[k]$	Element stiffness matrix
$[k_b]$	Flexural element stiffness matrix
$[k_m]$	Membrane element stiffness matrix
L_1, L_2, L_3	Triangular area coordinates
M_x, M_y, M_z	Moments about x, y and z axes
N_i	Shape function
p	Small positive correction factor
q	Small positive correction factor for weld profile
r	Radial distance from the crack front
T	Chord wall thickness
t	Thickness of shell
V	Element volume
u, v, w	Displacements in x, y and z directions
$\Delta x, \Delta y, \Delta z$	Displacements in x, y and z directions of plate node at transition
$\Delta x_i, \Delta y_i, \Delta z_i$	Displacements in x, y and z directions of inner surface nodes at transition

$\Delta x_o, \Delta y_o, \Delta z_o$	Displacements in x, y and z directions of outer surface nodes at transition
α, β, γ	Angles made by position vectors with x, y and z axes
$\alpha_j, \beta_j, \gamma_j$	Generalized displacement coordinates
Δ	Area of triangle
ν	Poisson's ratio
$\{\varepsilon\}$	Strain vector
$\{\sigma\}$	Stress vector
$\theta_x, \theta_y, \theta_z$	Rotations about x, y and z axes
$\{\delta\}$	Displacement vector
ΔK	Stress intensity range

CHAPTER I

1. INTRODUCTION

1.1 Background

The oil exploration in rough seas offshore has confronted the designers of fixed and floating structures with enhanced fatigue problems. These offshore structures are subjected to alternating wave loads. In particular the joints (intersections of tubular members) experience very high alternating stresses. Due to the geometric discontinuities in the welded connections, the stress concentration at brace-chord intersections plays a major role in the welded joint design. The design of steel offshore structures against fatigue requires all the accurate knowledge of stress distribution in tubular joints. For traditional design, based on S-N curves, only the calculation of maximum hot spot stress or strain is necessary. Existing literature on the analysis of tubular joints is limited to the use of two dimensional plate/shell elements, which neglect the displacement variation through the wall thickness direction.

The method currently employed for fatigue life estimation assumes that no defects or flaws are present in the structure prior to service and consequently makes allowance for both crack initiation and propagation. The nature of offshore structures is such that regions of high stress concentration and residual stress are likely to coincide with the areas where flaws are most likely. In addition, the stress required for fatigue crack initiation is much higher than that necessary for fatigue propagation so that if a flaw is present, prior to service, crack growth will be rapid.

In view of the above, it would be more appropriate to assume that small surface or embedded cracks are always present and that these will grow during service to form through-the-thickness cracks and eventually cause failure of the member. Computations based on this assumption could be used to estimate the structure life or the inspection interval before repair is necessary. The fracture mechanics approach based on the stresses existing near the crack tip and the use of a suitable fatigue crack growth expression provides a realistic method for fatigue life determination.

The theoretical stress analyses produced so far have shown that the stresses can be characterized by a term known as the stress intensity factor K. The uncertainty in predicting the stresses at the intersection and the fatigue life, due to the extremely complex geometry near the intersection, has prompted initiation of extensive research programmes. In view of the difficulties in obtaining a closed-form anlaysis, several approximate three-dimensional methods, such as direct potential and finite elements have been used for the stress analysis of finite-thickness fracture specimens containing through-the thickness cracks. But these solutions were for different specimen configurations and the results cannot be directly compared.

The stress distribution close to the crack front is dominated by the presence of the stress-free, crack surfaces at the crack tip. The square root singularity $1/\sqrt{r}$ is present in the existing solutions, regardless of the other features of geometry of the member. The magnitude of the components of crack tip stresses is directly proportional to stress intensity factor K. Thus the determination of

stress distributions and finally stress intensity factors for cracks located at the weld toes, is the prerequisite for determination of fatigue crack propagation life of a tubular joint.

1.2 Scope

The present investigation describes analytical studies on the stress distribution in tubular T-joints for two load cases: i) axial and ii) in-plane bending. The main objectives of the program are to determine:

a) Distribution of surface stresses along the brace-chord intersection, and hot spot stress concentration factors.

b) Stress fields at the weld toe in the hot spot area, including through thickness distribution, assuming an idealized shape of weld reinforcement.

c) The effect of shallow weld toe crack in the hot spot area on the stress redistribution.

This report presents the results of the study on distribution of surface stresses along the brace-chord intersection, including through thickness variation, the hot spot stress concentration factors and stress redistribution around shallow weld toe cracks using finite element methods.

1.3 Outline of the Project

The study includes two and three dimensional finite element stress analyses of the T-joint including the effect of shallow weld toe crack.

1.3.1 Two dimensional finite element stress analysis

For 2-D analysis the joint is discretized using automatic mesh generation. The triangular elements along with the general quadrilateral elements are used for the two dimensional stress analysis of the joint. The shell analysis includes the membrane stiffness representation by the plane stress element and the flexural stiffness by the plate bending element. The distribution of surface stresses along the critical sections and the hot spot stress concentration factors are investigated.

1.3.2 Three dimensional finite element stress analysis

Using force and displacement methods, the regions of high stress gradient and the weld zone are reanalysed using three dimensional isoprametric elements across the thickness. For the three dimensional mesh generation of the brace-chord intersection region including weld, an automatic mesh generation scheme is used. The boundary values at the plate to solid element transition zone, obtained from the two dimensional analysis, are distributed between the outer and inner surface nodes of the solid elements in such a way as to maintain boundary force equilibrium displacement compatibility.

1.3.3 Three dimensional finite element stress analysis with shallow weld toe crack

The entire models with shallow weld toe crack are reanalyzed. The joint is discretized using special singular elements around the crack front surrounded by solid elements. The singular elements produce a

singular stress field at the crack front. The effect of the weld toe cracks on surface stress distribution is investigated.

CHAPTER II

2. LITERATURE REVIEW

2.1 Analytical Investigation

2.1.1 Introduction

Because of the relative complexity of the geometrical configuration of tubular intersections as well as the thin-shell theory governing their behaviour, reliable, prediction of the stresses in such joints by analytical techniques has been proven to be difficult. The finite element method seemed to offer a natural solution for modelling complex geometries and boundary conditions. Early attempts to apply finite elements to the stress analysis of tubular intersections were somewhat hindered by the computational demands generated by too many elements. The difficulty was overcome by the third-generation computers with its larger central memory and faster computing speed.

The finite element method would at first appear to be ideal for studying elastic behaviour of structures containing crack-like defects. However, problems arise in modelling the near crack tip stress field using finite elements. This is due to the singularity at the crack tip resulting from the linear elastic analysis of a crack, which in practice has a small plastic region at its tip. Finite elements in their basic form are unable to represent this crack tip singularity, and thus produced poor results when applied to fracture problems, unless extremely fine meshes are used. Many attempts have been made to overcome the inability of finite elements to represent the crack tip singularity by developing special elements which incorporate the required stress singularity in their formulation.

2.1.2 Discretization of the joint

A procedure for the interactive modelling of two or three dimensional finite element grids has been presented by Hoffman[1]. The grids are generated by specifying the key points, boundary or intersection lines, surfaces and regions. The general process of displaying a two dimensional representation of a three dimensional model has been discussed. Based on the maximum model dimension, the dimensions of the display area, and the position on the screen at which the object is to be placed, an initial screen/object orientation ratio is determined. An interactive graphic system was developed by Bousquet and Yates [2] for use with finite element programs in a production analysis environment.

A relatively straight forward mesh generation program based on isoparametric mapping concept has been developed by Durocher [3]. The program generates node numbers, coordinates, and element connectivity information for five commonly used two-dimensional elements. User-defined superelements are subdivided into 3-noded or 6-noded triangular or into 4-noded or 8-noded isoparametric quadrilateral elements. Felippa [4] developed a FORTRAN subroutine to generate an alphanumeric image of an arbitrary two-dimensional finite element mesh on the line printer. The plotting can be used for fast on-line display of nodal points, elements, boundary conditions and loads during the input data processing stage of a finite element analysis. A code was devised for automatic mesh generation schemes, utilizing the techniques of mapping from a local non-dimensional system of reference into the global cartesian system of reference [5].

2.1.3 Stress analysis

Clough and Tocher [7] studied the relative accuracy provided by seven different types of finite elements in the approximate analysis of plate bending. The stiffness matrices for three rectangular and four triangular elements are considered. Analyses are made with each of these elements for the central deflection in eight different rectangular plate systems, using five different mesh sizes. Some rectangular and triangular elements are found to give results which converge towards the correct answer as the mesh size is refined. Ahmad et al. [8] presented a general formulation for the curved, arbitrary shape of thick shell finite elements. A new process using curved, thick shell finite elements is developed overcoming the approximation of the geometry of the structure and the neglect of shear deformation. Several illustrated examples ranging from thin to thick shell applications are given to assess the accuracy of solution attainable.

Clough and Johnson [9] have presented an approximate numerical analysis procedure for solving thin shells. The shell is idealized as an assemblage of triangular finite elements representing both membrane and flexural stiffness properties. Five examples are presented demonstrating the versatility of the procedure for analysing different shell configurations. Liaw et al. [10] described the application of three-dimensional isoparametric elements to the analysis of welded tubular connections. It is concluded that the three-dimensional isoparametric elements, when implemented in an efficient and versatile computer program, can provide more accurate resolution of stress concentration factors than would be possible using flat plate finite elements.

A computer program has been developed [11] as a design tool for analyzing a ring-stiffened tubular joint with multiple non-intersecting branch members. Radenkovic [12] obtained the stresses for a T-joint in tension using three types of elements. Several large codes i.e. ASAS, SESAM 69, SATE, and TITUS are used for the stress analysis during the course of the research. But little direct comparison has been done between the codes. Five typical joint designs were modelled by finite elements [13]: three by manually laying out the mesh and two using an automatic mesh generation program. The finite element idealizations were then used as input in the computer program STARDYNE. The results are compared with experimental stress analysis of scale models.

The degenerated 20-noded isoparametric brick element is used for the stress analysis of the T-joint [14]. The ill conditioned stiffness matrix due to the higher stiffness properties in the thickness direction in comparison to other two directions is eliminated. The stiffness formulation of the joint is done by ignoring the strain energy of the stresses normal to the midsurface of the shell.

Two types of three-dimensional isoparametric elements are used for tubular joint analysis [15]. Various incompatible modes are introduced into the stiffness formulations of these elements to improve their flexural behaviour. The 8-noded brick and 16-noded thick shell elements utilize three and one incompatible even shape functions respectively. In the irregular mesh, the incompatible brick element is more satisfactory than the basic element.

2.1.4 Finite element analysis of crack problems

For three-dimensional elastic continua with cracks, the stress field near the crack front is obtained by solving the Navier's equations of equilibrium subjected to appropriate boundary conditions [16]. Due to the complexity of the solution, stress fields around the crack front in three-dimensional continua are available for only a few restricted classes of problems such as penny-shaped and elliptic cracks in an infinite solid. For fracture specimens of finite thickness with through-thickness cracks, some attempts have been made to obtain stress distribution close to the crack front [17], but the solutions have been found to be intractable in closed-form [17,18]. Hartranft and Sih [17] showed that the stresses σ_x, σ_y, and σ_{xy} had a square-root singularity at the crack front and σ_z and the two transverse shear stresses σ_{yz} and σ_{xz} were finite throughout the plate. In view of the difficulties in obtaining a closed-form analysis, several approximate three-dimensional methods have been used for the stress analysis of finite-thickness fracture specimens containing through-thickness cracks.

A finite element model has been formulated [19] for three-dimensional analysis of a general crack problem with a crack front state in combined modes I and II. Special elements have been suggested which embed the inverse square root singularity along the crack front. The singularity element used is a six node wedge focused onto the front. The crack front has been taken as rectilinear and a group of singularity elements are used about each segment. Adjacent to the singularity elements eight-node isoparametric brick elements are used.

A compact tension plate specimen has been treated based on the above formulation. The displacement function for either element has been suggested in the general form. Using the triangular singularity elements [20] near the tip together with quadrilateral isoparametric elements, stress intensity factors within 5 per cent of accepted values were obtained for two typical cracked configurations.

Raju and Newman [21] calculated the stress intensity factors for most of the commonly used fracture specimens using a three-dimensional finite element elastic stress analysis. A three-dimensional singularity element in the shape of a pentahedron, similar to that developed by Tracy [20], was used at the crack front. A nodal force method was developed and used to evaluate the mode-I stress intensity factors along the crack front. The effects of specimen thickness and length on stress intensity distributions were investigated. Blackburn and Hellen [22] have calculated the stress intensity factors for an edge-cracked plate subjected to both modes I and III loading, containing a penny-shaped crack and a semi-circular surface crack in long square prism under tension. The displacements are compared with those computed at the vertex and mid-side nodes around the crack tip by the finite element analysis. Special elements are used at the tip to represent the variation of the displacement with respect to the square root of the distance from the tip and compatible with surrounding quadratic elements.

Alwar and Ramachandran [23] investigated the variation of the stress intensity factors for finite plates across the plate thickness using finite element technique. The crack tip region is represented by

degenerate triangular quarter-point prism elements, which have the required $1/\sqrt{r}$ singularity for all normal stresses and in-plane shear stress at the crack tip. A convergence study for the variation of the stress intensity factors has been made using two, three and four layers of elements across half the thickness of the plate and also by reducing the crack tip element size and increasing the degrees-of-freedom for a single layer. For a thin plate, variation is found to be linear and as thickness increases the variation has been shown to be nonlinear.

Without sacrificing the advantage of simplicity and conformability of Blackburn's six node element for modelling the crack tip, a minor adjustment in the interpolation field has been proposed by Morris and Becker [24], which permits quadratic variation in the singular part of the displacement. Using a convenient co-ordinate system, the integrations are done exactly in the radial co-ordinate direction. The shape functions provide both constant strain capability and conformability with quadratic isoparametric elements. A finite element method utilizing quadrilateral elements has been developed by Kuang, et al.[25] to determine the stress intensity factor K_I for a single-edge notch beam. Hermitian interpolation functions are used to describe the displacements in the regular elements and Williams stress function [26] is used to develop the singular element.

The welded plate T-joint has been analysed for a series of crack shapes and crack depth [27]. The crack tip regions are modelled using degenerate isoparametric element devoped by Barsoum [28]. The effects of crack shape, crack depth and weld angle on the stress intensity factors are presented.

CHAPTER III

3. TWO DIMENSIONAL FINITE ELEMENT ANALYSIS

3.1 Mesh Generation

The tubular T-joint is discretized using an automatic mesh generation technique. Since the loads acting on the tubular T-joint could be either axial or in-plane bending, the advantage of symmetry is taken into consideration in discretization and only half of the T-joint is considered for modelling. The following procedures are adopted for the mesh generation:

a) A fine mesh is utilized near the intersection between the chord and brace, where the stress gradient is sharp.

b) Coarser mesh is used at the ends of both chord and brace where the stresses are small.

c) The nodes are numbered in such a way to minimize the incidence of elements and thereby reduce the band width of the global stiffness matrix.

The complete model has been divided into seven sections (Fig. 3.1). The oxyz coordinate system is defined at the left of the model. For each section some key points are defined by either a cartesian coordinate or an angle. Considering the mesh sizes, the y-coordinates for bottom nodes of section 1, section 2, section 6, and lower curve nodes of section 3, and z coordinates for the side nodes of section 4 are defined. The coordinates of the nodes at the intersection of brace and chord are generated. The nodal coordinates are generated section-wise and the node numbers by assigning proper indices corresponding to a particular section. All sections are combined together using the common node matching technique between the

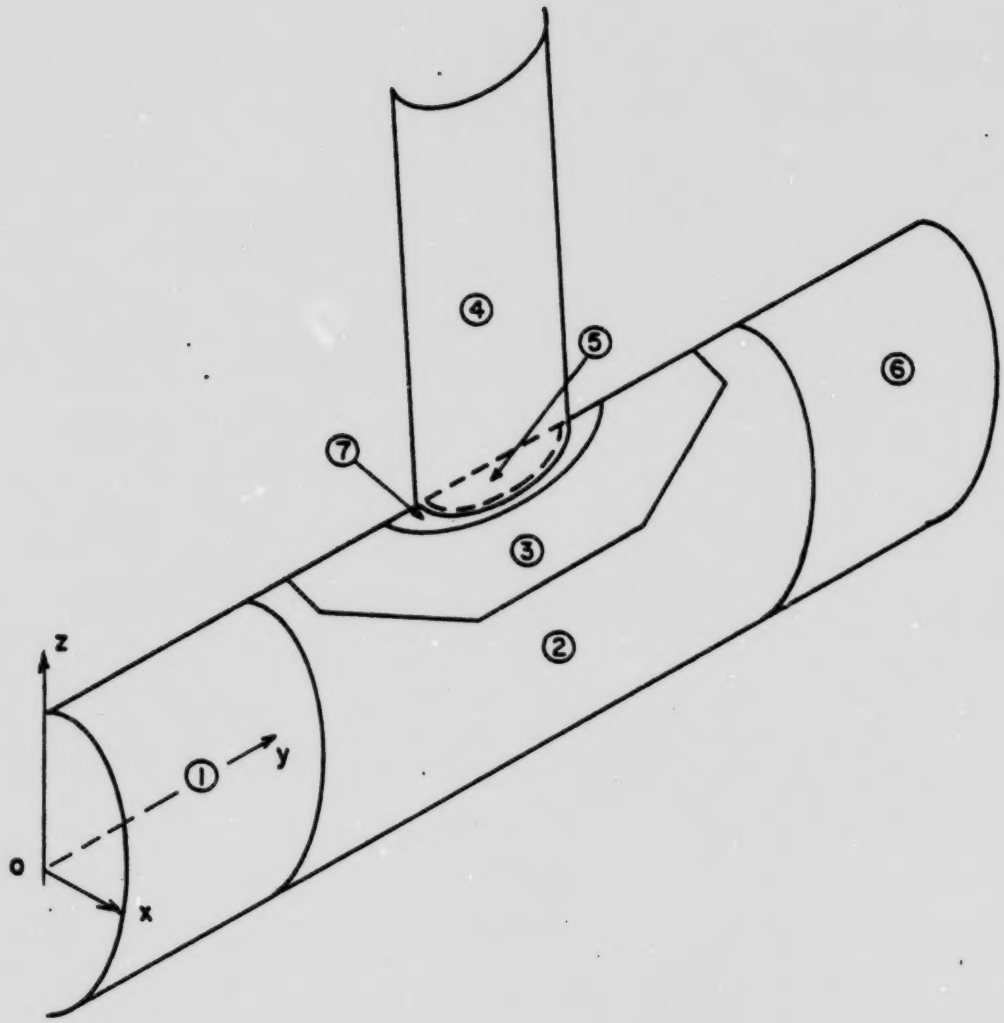

FIG. 3.1 REGIONS OF T-JOINT MODEL FOR MESH GENERATION

sections. Then the node numbers are rearranged for the complete model in a way so as to have minimum band width. For nodal connectivity of elements, the node numbering sequences are identified in the anti-clockwise direction (Fig. 3.2).

In order to plot the generated mesh for the model, the x, y and z axes are rotated through angles α, β and γ in three stages to attain the new axis systems ox'y'z', ox"y"z" and $\overline{oxyz}$ respectively (Fig. 3.3). The relation between oxyz and $\overline{oxyz}$ coordinates can be written as

$$\begin{Bmatrix} x \\ y \\ z \end{Bmatrix} = [A]\,[B]\,[C] \begin{Bmatrix} \bar{x} \\ \bar{y} \\ \bar{z} \end{Bmatrix} \tag{3.1}$$

where

$$[A] = \begin{bmatrix} 1 & 0 & 0 \\ 0 & \cos\alpha & -\sin\alpha \\ 0 & \sin\alpha & \cos\alpha \end{bmatrix} \tag{3.2}$$

$$[B] = \begin{bmatrix} \cos\beta & 0 & \sin\beta \\ 0 & 1 & 0 \\ \sin\beta & 0 & \cos\beta \end{bmatrix} \tag{3.3}$$

$$[C] = \begin{bmatrix} \cos\gamma & -\sin\gamma & 0 \\ \sin\gamma & \cos\gamma & 0 \\ 0 & 0 & 1 \end{bmatrix} \tag{3.4}$$

Using Eqn. (3.1), the coordinates of the nodal points are transformed into new oxyz coordinate system, which are then used in plotting the discretized model of the tubular T-joint.

3.2 Element Stiffness Formulation

The most critical step in two-dimensional stress analysis is the evaluation of the stiffness properties of an individual element. It is

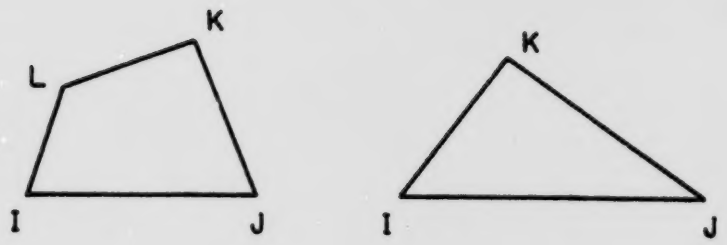

FIG. 3.2 NODE NUMBERING SEQUENCES

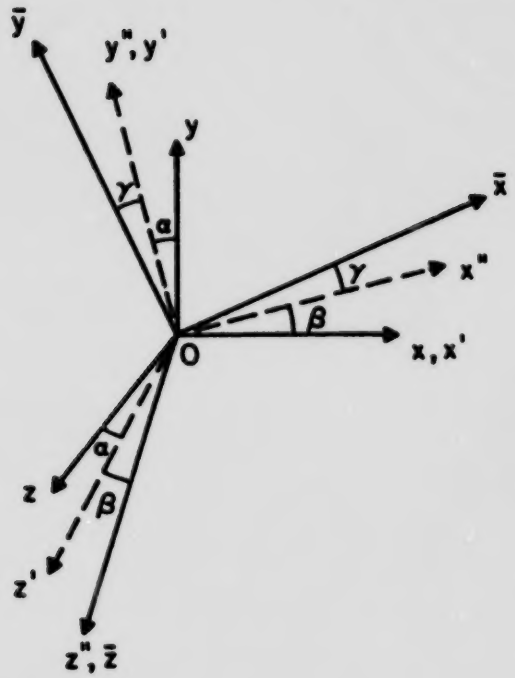

FIG. 3.3 ROTATION OF COORDINATE SYSTEM AXES FOR MESH GENERATION

assumed that the elements are interconnected only at their corner points. Two types of element stiffnesses are considered in the analysis: membrane stiffness which relates forces and displacements in the plane of the elements, and the plate bending stiffness which takes account of displacements and out of plane deformations. The membrane and flexural stiffnesses are represented without coupling using plane stress and plate bending elements.

3.2.1 Plate bending element

The triangular element stiffness matrix is derived using area coordinates. The area coordinates L_1, L_2, L_3 of any point P in the triangle are defined as the ratio of the area Δ_i, of the subtriangles subtended at that point, to the total area Δ, of the triangle i.e. $L_i = \Delta_i/\Delta$ (Fig. 3.4). The linear relation between the set of area coordinates and the cartesian system is given by

$$\begin{Bmatrix} 1 \\ x \\ y \end{Bmatrix} = \begin{bmatrix} 1 & 1 & 1 \\ x_1 & x_2 & x_3 \\ y_1 & y_2 & y_3 \end{bmatrix} \begin{Bmatrix} L_1 \\ L_2 \\ L_3 \end{Bmatrix} \tag{3.5}$$

Inversion of Eqn. (3.5) gives the area coordinates as

$$\begin{Bmatrix} L_1 \\ L_2 \\ L_3 \end{Bmatrix} = \frac{1}{2\Delta} \begin{bmatrix} a_1 & b_1 & c_1 \\ a_2 & b_2 & c_2 \\ a_3 & b_3 & c_3 \end{bmatrix} \begin{Bmatrix} 1 \\ x \\ y \end{Bmatrix} \tag{3.6}$$

where

$$\begin{aligned} a_i &= x_j\, y_k - x_k\, y_j \\ b_i &= y_j - y_k \\ c_i &= x_k - x_j \end{aligned} \tag{3.7}$$

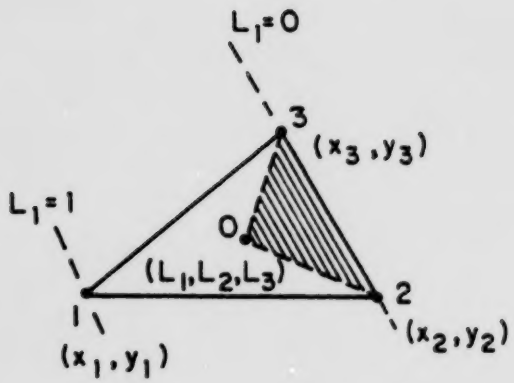

FIG. 3.4 TRIANGULAR AREA COORDINATE

$$\Delta = \frac{1}{2}\begin{vmatrix} 1 & x_1 & y_1 \\ 1 & x_2 & y_2 \\ 1 & x_3 & y_3 \end{vmatrix}$$

The transverse displacement w_i and the rotations about x and y axes, θ_{xi} and θ_{yi} at each corner node are taken as nodal degrees of freedom in the flexural element stiffness derivation (Fig. 3.5). The displacement within the element can be described in the form

$$\begin{aligned} w = {} & \beta_1 L_1 + \beta_2 L_2 + \beta_3 L_3 + \beta_4 (L_1^2 L_2 + \tfrac{1}{2} L_1 L_2 L_3) \\ & + \beta_5 (L_1 L_2^2 + \tfrac{1}{2} L_1 L_2 L_3) + \beta_6 (L_2^2 L_3 + \tfrac{1}{2} L_1 L_2 L_3) \\ & + \beta_7 (L_2 L_3^2 + \tfrac{1}{2} L_1 L_2 L_3) + \beta_8 (L_3^2 L_1 + \tfrac{1}{2} L_1 L_2 L_3) \\ & + \beta_9 (L_3 L_1^2 + \tfrac{1}{2} L_1 L_2 L_3) \end{aligned} \tag{3.8}$$

Substituting for the nodal values of

$$w_i,\ \theta_{xi} = -\left(\frac{\partial w}{\partial y}\right)_i \text{ and } \theta_{yi} = \left(\frac{\partial w}{\partial x}\right)_i \tag{3.9}$$

the constants β's, and hence the shape functions $N_i (i = 1,2,3)$ are determined. For ith node, the shape function, N_i can be written as

$$[N_i]^T = \begin{Bmatrix} L_i + L_i^2 L_j + L_i^2 L_k - L_i L_j^2 - L_i L_k^2 \\ b_k (L_i^2 L_j + \frac{1}{2} L_i L_j L_k) - b_j (L_k L_i^2 + \frac{1}{2} L_i L_j L_k) \\ c_k (L_i^2 L_j + \frac{1}{2} L_i L_j L_k) - c_j (L_k L_i^2 + \frac{1}{2} L_i L_j L_k) \end{Bmatrix} \tag{3.10}$$

The strain displacement relation for the element is written in terms of nodal displacements as

$$\{\varepsilon\} = \begin{Bmatrix} \frac{-\partial^2 w}{\partial x^2} \\ \frac{-\partial^2 w}{\partial y^2} \\ 2\frac{\partial^2 w}{\partial x \partial y} \end{Bmatrix} = [B_i\ B_j\ B_k] \begin{Bmatrix} a_{bi} \\ a_{bj} \\ a_{bk} \end{Bmatrix} \tag{3.11}$$

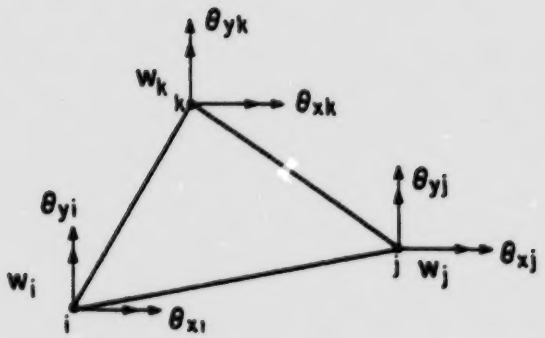

Degrees - of - Freedom

Fig. 3.5 Bending Element

where

$$B_i = \begin{matrix} \dfrac{-\partial^2 N_i}{\partial x^2} \\ \dfrac{-\partial^2 N_i}{\partial y^2} \\ 2\dfrac{\partial^2 N_i}{\partial x \partial y} \end{matrix} \qquad (3.12)$$

$$a_{bi} = \begin{matrix} w_i \\ \theta_{xi} \\ \theta_{yi} \end{matrix} = \begin{matrix} w_i \\ -(\frac{\partial w}{\partial y})_i \\ (\frac{\partial w}{\partial x})_i \end{matrix}$$

As the shape function, N_i is a polynomial in area coordinates, the differentiation with respect to x, y is performed as

$$\frac{\partial N_i}{\partial x} = \sum_{j=1}^{3} \frac{\partial N_i}{\partial L_j}\frac{\partial L_j}{\partial x} = \frac{1}{2\Delta}\left(b_i \frac{\partial N_i}{\partial L_1} + b_j \frac{\partial N_i}{\partial L_2} + b_k \frac{\partial N_i}{\partial L_3}\right)$$

$$\frac{\partial N_i}{\partial y} = \sum_{j=1}^{3} \frac{\partial N_i}{\partial L_j}\frac{\partial L_j}{\partial y} = \frac{1}{2\Delta}\left(c_i \frac{\partial N_i}{\partial L_1} + c_j \frac{\partial N_i}{\partial L_2} + c_k \frac{\partial N_i}{\partial L_3}\right) \qquad (3.13)$$

The terms in the [B] matrix remain polynomial in the area coordinates. The flexural element stiffness matrix is obtained using the general expression

$$[K_b] = t \iint_A [B]^T[D][B]\, dA \qquad (3.14)$$

where t = the thickness of the element and [D] = the elasticity matrix.

For an isotropic plate, [D] is given by

$$[D] = \frac{Et^3}{12(1-\nu^2)} \begin{matrix} 1 & \nu & 0 \\ \nu & 1 & 0 \\ 0 & 0 & \frac{1-\nu}{2} \end{matrix} \qquad (3.15)$$

The resulting polynomial in area coordinates in Eqn. 3.14 is integrated using the relation

$$\iint_A L_i^{\alpha} L_j^{\beta} L_k^{\gamma} dA = \frac{\alpha!\ \beta!\ \gamma!}{(\alpha + \beta + \gamma + 2)!}\ 2A \tag{3.16}$$

3.2.2 Membrane element

The displacements u and v along x and y axes at each node are taken as the nodal degrees of freedom (Fig. 3.6). The displacements within the element are expressed in terms of nodal values as

$$\begin{aligned} u &= L_1 u_1 + L_2 u_2 + L_3 u_3 \\ v &= L_1 v_1 + L_2 v_2 + L_3 v_3 \end{aligned} \tag{3.17}$$

in which shape functions are

$$\begin{aligned} N_1 &= L_1 \\ N_2 &= L_2 \\ N_3 &= L_3 \end{aligned} \tag{3.18}$$

The strain-displacement relations are

$$\{\varepsilon\} = \begin{Bmatrix} \frac{\partial u}{\partial x} \\ \frac{\partial v}{\partial y} \\ \frac{\partial u}{\partial y} + \frac{\partial v}{\partial x} \end{Bmatrix} = [B_i\ B_j\ B_k] \begin{Bmatrix} a_{mi} \\ a_{mj} \\ a_{mk} \end{Bmatrix} \tag{3.19}$$

where

$$[B_i] = \begin{bmatrix} \frac{\partial N_i}{\partial x} & 0 \\ 0 & \frac{\partial N_i}{\partial y} \\ \frac{\partial N_i}{\partial y} & \frac{\partial N_i}{\partial x} \end{bmatrix} \tag{3.20}$$

$$\{a_{mi}\} = \begin{Bmatrix} u_i \\ v_i \end{Bmatrix}$$

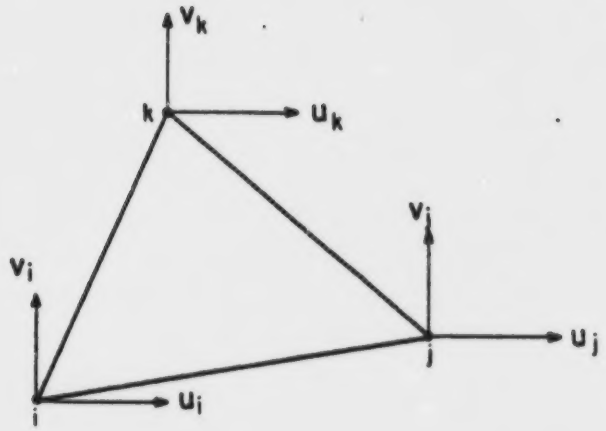

Degrees - of - Freedom

Fig. 3.6 Membrane Element.

The membrane element stiffness matrix is determined using the expression

$$[k_m] = t\iint_A [B]^T[D]\,[B]\,dA \tag{3.21}$$

where [D] = the elasticity matrix, which is given by

$$[D] = \frac{E}{1-\nu^2}\begin{bmatrix} 1 & \nu & 0 \\ \nu & 1 & 0 \\ 0 & 0 & \frac{(1-\nu)}{2} \end{bmatrix} \tag{3.22}$$

3.2.3 Assembly of six degrees of freedom

The state of strain is uniquely described in terms of u and v displacements at each node i for the in-plane action by stiffness matrices of the type

$$\{f_m\} = [k_m]\ \{a_m\} \tag{3.23}$$

where

$$\{a_{mi}\} = \begin{Bmatrix} u_i \\ v_i \end{Bmatrix}$$

$$\{f_{mi}\} = \begin{Bmatrix} f_{xi} \\ f_{yi} \end{Bmatrix} \tag{3.24}$$

For bending, the state of strain is expressed in terms of the nodal displacement in the z-direction, w and two rotations θ_x and θ_y (Fig. 3.7). The stiffness matrix is of the form

$$\{f_b\} = [k_b]\ \{a_b\} \tag{3.25}$$

where

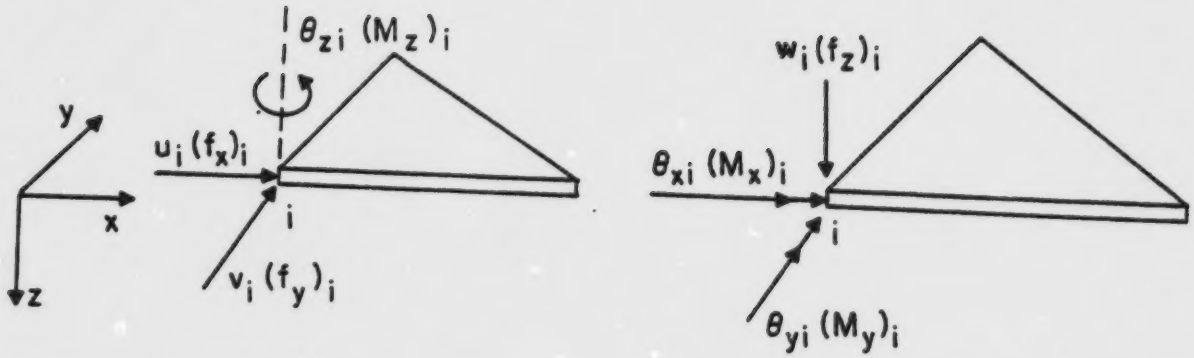

Inplane Forces and Deformations

Bending Forces and Deformations

FIG. 3.7 ASSEMBLY OF SIX-DEGREES OF FREEDOM

$$\{a_{bi}\} = \begin{Bmatrix} w_i \\ \theta_{xi} \\ \theta_{yi} \end{Bmatrix}$$

$$\{f_{bi}\} = \begin{Bmatrix} f_{zi} \\ M_{xi} \\ M_{yi} \end{Bmatrix} \tag{3.26}$$

The flexural and membrane effects are combined using the relation

$$\{f\} = [k]\{a\} \tag{3.27}$$

where

$$\{f_i\} = \{f_{xi}\ f_{yi}\ f_{zi}\ M_{xi}\ M_{yi}\}^T$$

$$\{a_i\} = \begin{Bmatrix} a_{mi} \\ a_{bi} \\ \theta_{zi} \end{Bmatrix} \tag{3.28}$$

The element stiffness matrix in local coordinate would be made up of the following submatrices:

$$[k]_{18x18} = \begin{bmatrix} [k_m]_{6x6} & [0] & [0] \\ [0] & [k_b]_{9x9} & [0] \\ [0] & [0] & [0]_{3x3} \end{bmatrix} \tag{3.29}$$

The elements in the stiffness matrix in Eqn. 3.29 corresponding to θ_z direction are zero, which lead to difficulties in computational algorithm. The singularity is avoided by modifying the element stiffness matrix before assembly by the following equation

$$\begin{bmatrix} M_{zi} \\ M_{zj} \\ M_{zk} \end{bmatrix} = \alpha E V \begin{bmatrix} 1 & -0.5 & -0.5 \\ & 1 & -0.5 \\ \text{sym} & & 1 \end{bmatrix} \begin{bmatrix} \theta_{zi} \\ \theta_{zj} \\ \theta_{zk} \end{bmatrix} \tag{3.30}$$

where

E = the modulus of elasticity

V = element volume and

α = small number, typically in the range of 10^{-6} to 10^{-2}

The quadrilateral element with thirty degrees-of-freedom is obtained by combining the four triangular subelements. Static condensation is then used to exclude the degrees-of-freedom associated with the interior node to obtain the final stiffness matrix of size 24 by 24 (Fig. 3.8).

3.3 2-Dimensional Results and Discussion

3.3.1 General

A computer program based on the finite element formulation given in section 3.2 is used for the two dimensional analysis of the tubular T-joint. The stresses are obtained at the centroid of each element. The accuracy of the program has been checked by comparing the computed displacements with those reported for a barrel (cylindrical) vault supported by rigid diaphragm at two ends and loaded by its own weight [29].

The joint parameters are given in Table 3.1. Figure 3.9 shows the schematic of the T-joint model analysed. Finite element meshes for different regions and the complete discretised model are shown in Figs. 3.10 and 3.11. The total number of elements and nodes are 416 and 464 respectively. All translational and rotational degrees of freedom have been restrained at the nodes at both ends of chord i.e. along lines CD and EF. The x-translational, y and z rotational degrees of freedom for the nodes along the edges AB, BC, DE, EF, FG, GH and BIG, are restrained from symmetric consideration. The results are based on the

TABLE 3.1
Joint Parameters

Type of Joint	D (mm)	T (mm)	$\beta = \frac{d}{D}$	$\tau = \frac{t}{T}$	$\gamma = \frac{D}{2T}$	$\alpha = \frac{2L}{D}$
T	850	32	0.5	0.5	13.2	8.4

D = Chord diameter
d = Brace diameter
T = Chord thickness
t = Brace thickness
2L = Length of chord between supports

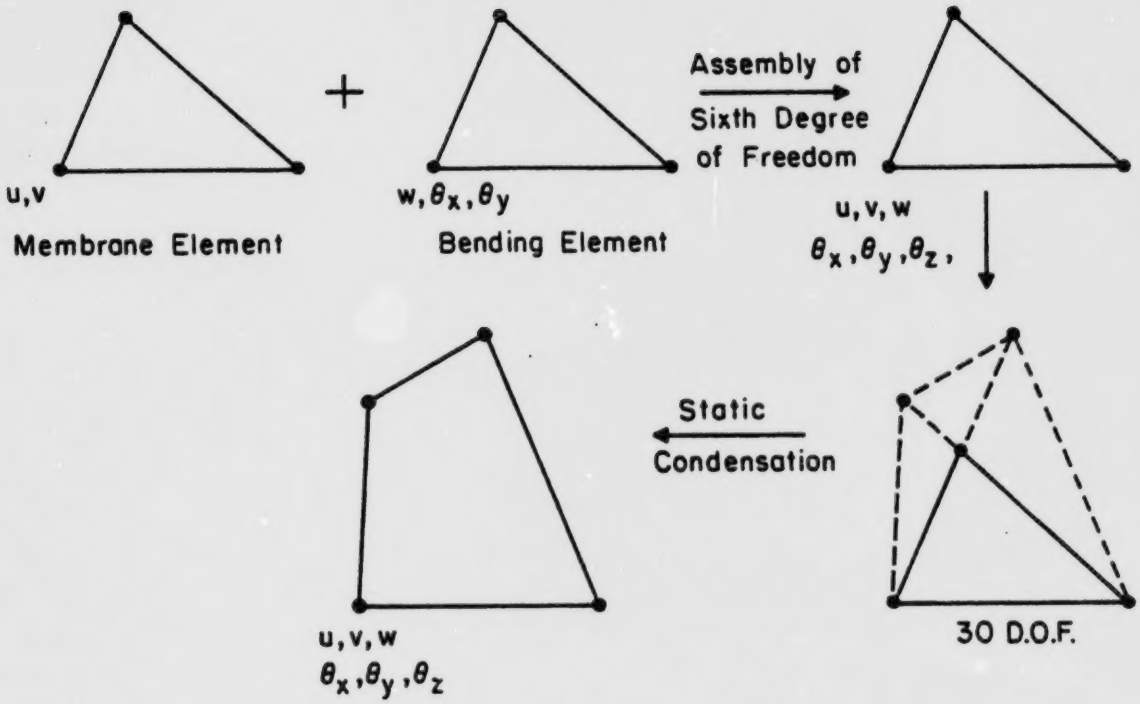

FIG. 3.8 ASSEMBLY OF TRIANGULAR ELEMENTS TO FORM QUADRILATERAL ELEMENT

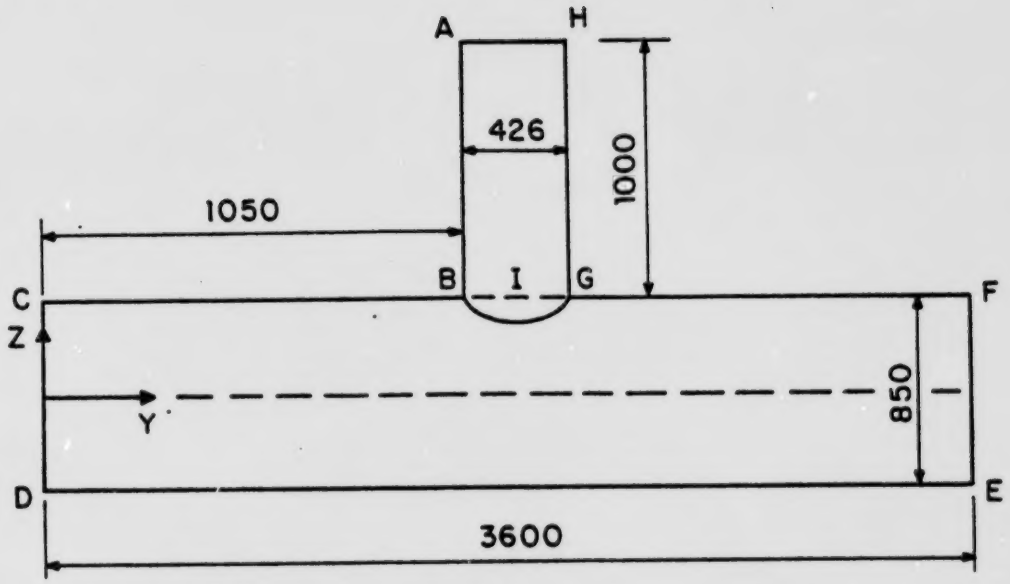

All Dimensions are in mm.

FIG. 3.9 SCHEMATIC OF T-JOINT MODEL

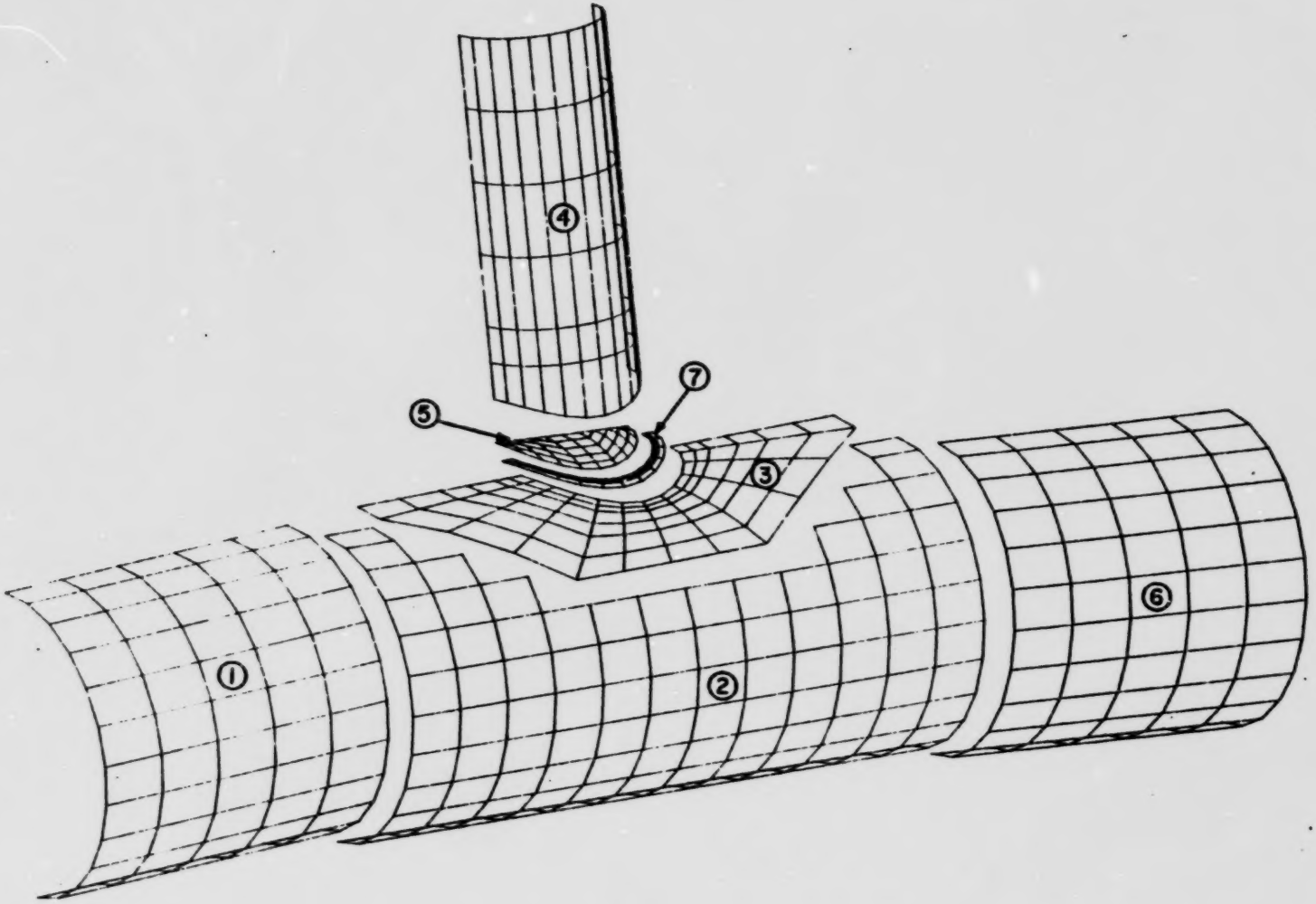

FIG. 3.10 FINITE ELEMENT MESH FOR DIFFERENT REGIONS.

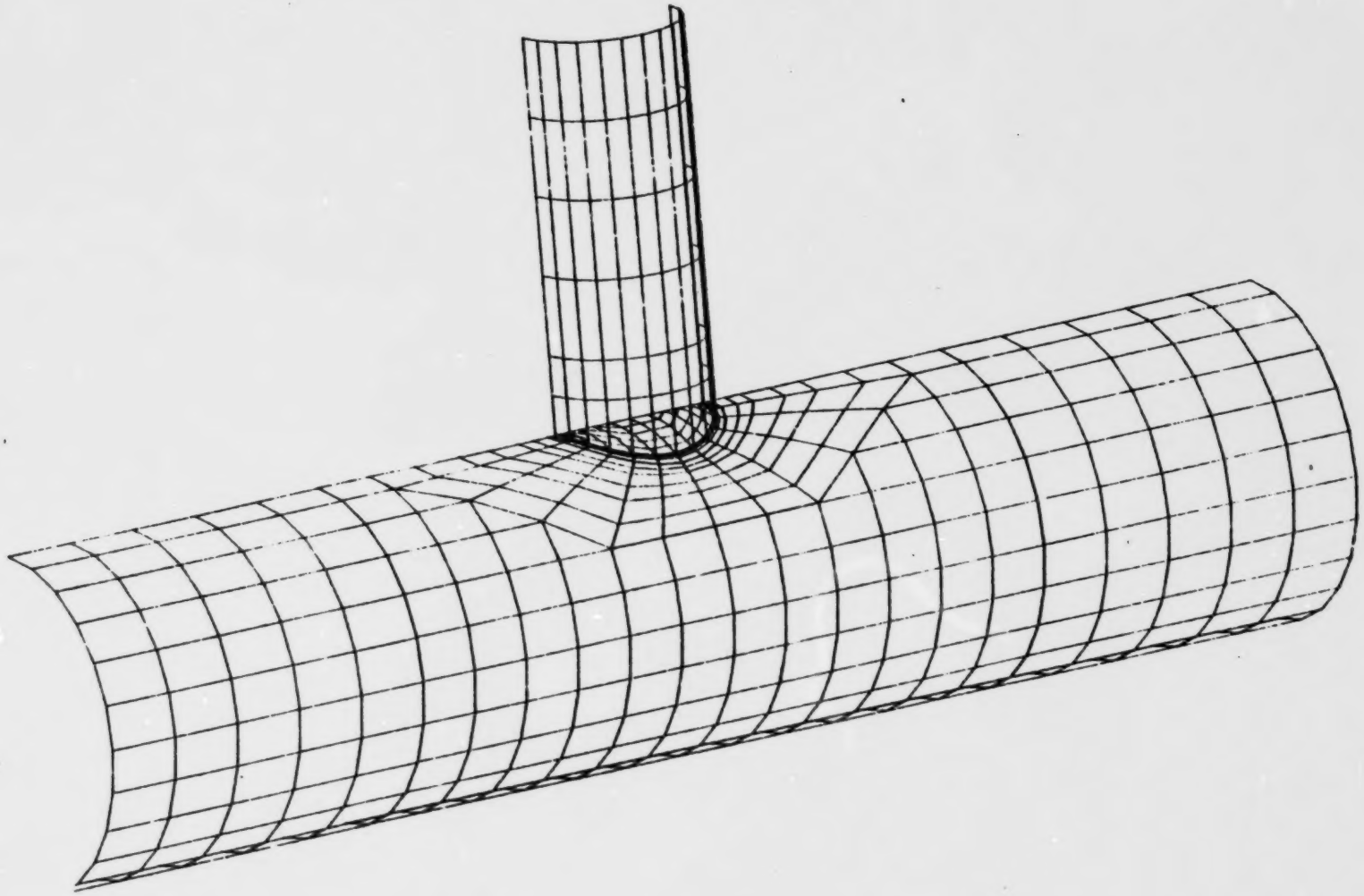

FIG. 3.11 FINITE ELEMENT MESH GENERATION FOR THE JOINT.

following material properties of steel: Young's Modulus, E = 2.1 x 10^{11} N/M^2, and Poisson ratio, ν = 0.3.

The joint is analysed for two different loads acting on the brace - (i) axial compressive load of 10^6N and (ii) in-plane bending load of 10^5N. The normalized deformed shapes of the joint for the two cases are shown in Figs. 3.12 and 3.13. The variation of maximum principal stresses due to both cases at certain critical locations (Fig. 3.14) are shown in Figs. 3.15 - 3.22. The stress concentration factors for chord and brace due to axial compressive and in-plane bending loads are obtained both at crown and saddle points, and shown in Table 3.2.

The calculated stress concentration factors are compared with the published literature based on experimental work and finite element analysis [30,31] and the parametric equations [32,33,34]. The parameters of the joint analysed by Clayton, et al [31] are α = 13.5, β = 0.5, τ = 0.5, γ = 12.1 whereas those of the joint analysed by Irvine [30] are α = 10.5, β = 0.53, τ = 0.51 and γ = 13.4.

3.3.2 Chord stresses

In the chord side it shows good general agreement with the measured stress concentration factor (Table 3.2). Under axial load, peak stress occurs at the saddle point. There is reversal of the principal stress along line-4 (Fig. 3.21). The stress gradient at the intersection is not so steep on the chord as on the brace (Figs. 3.17 and 3.21). In case of in-plane bending load, the peak stress occurs at the crown (Table 3.2). The stress gradient near the intersection in line-3 is less compared to that on brace line-1.

TABLE 3.2
Stress Concentration Factors

Methods	Chord Side				Brace Side			
	Axial		In-plane Bending		Axial		In-plane Bending	
	Crown Line-3	Saddle Line-4	Crown Line-3	Saddle Line-4	Crown Line-1	Saddle Line-2	Crown Line-1	Saddle Line-2
Present 2-Dimensional Finite Element Analysis (without plug)	2.968	7.004	1.35	0.977	4.18 3.96*	7.68 7.04*	3.36 2.34*	0.584 0.481*
Present 2-Dimensional Finite Element Analysis (with plug)	2.656	6.277	1.07	0.8	3.69 2.41*	6.8 6.02*	2.92 2.08*	0.497 0.427*
Analysis [31]	-	6.7	2.6	-	-	9.3	3.0	-
Experiment [31]	-	5.8	2.0	-	-	7.1	1.7	-
Experiment [30]	-	7.7	1.2	-	-	-	-	-
Smedly and Wordsworth [32]	3.097	7.439	2.38	-	2.951	5.686	2.499	-
Gibstein [33]	-	6.7	2.2	-	-	-	2.065	-
Kuang [34]	-	6.9	1.9	-	-	-	2.358	-

*with correction for brace rotation and translation

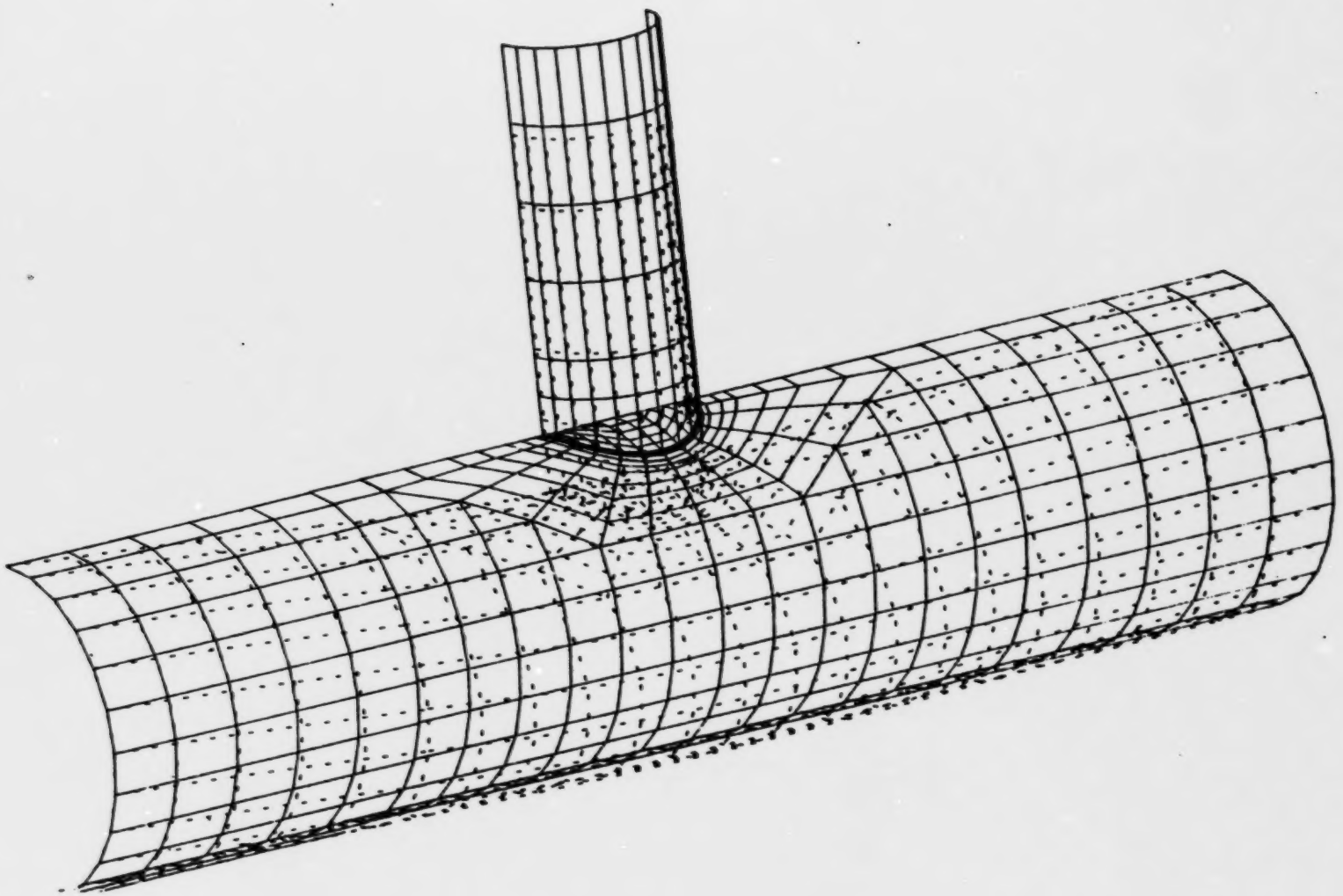

FIG. 3.12 DEFORMED JOINT DUE TO AXIAL COMPRESSIVE LOAD.

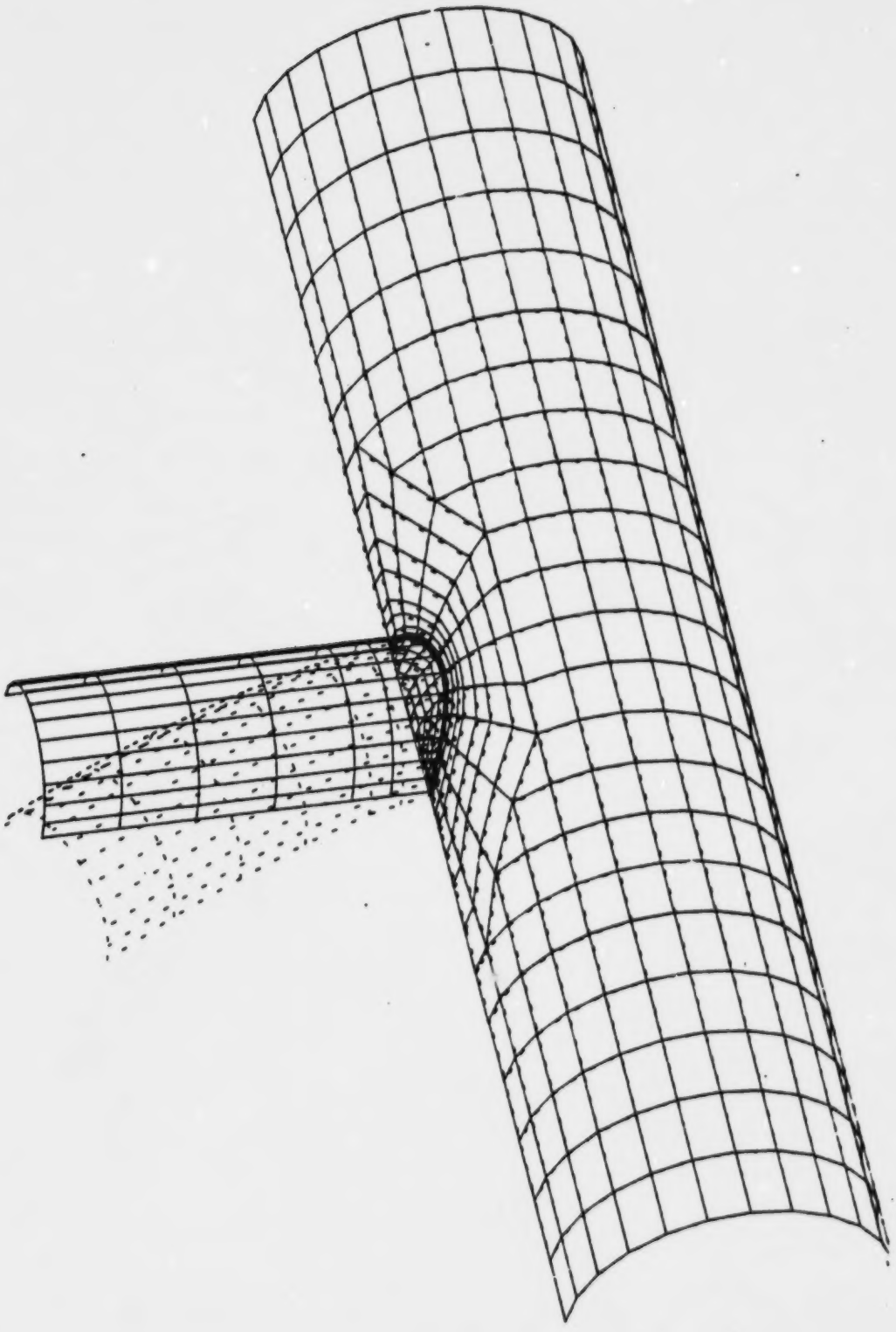

FIG. 3.13 DEFORMED JOINT DUE TO IN-PLANE BENDING LOAD

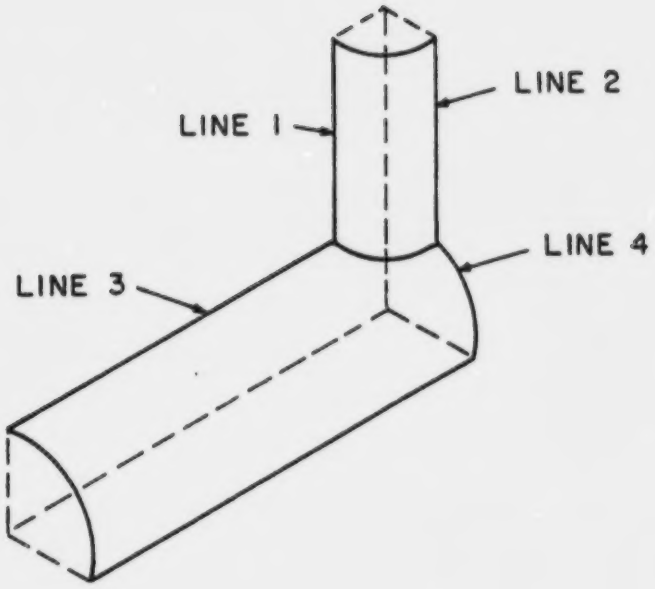

FIG. 3.14 CHARACTERISTIC LINES OF THE JOINT

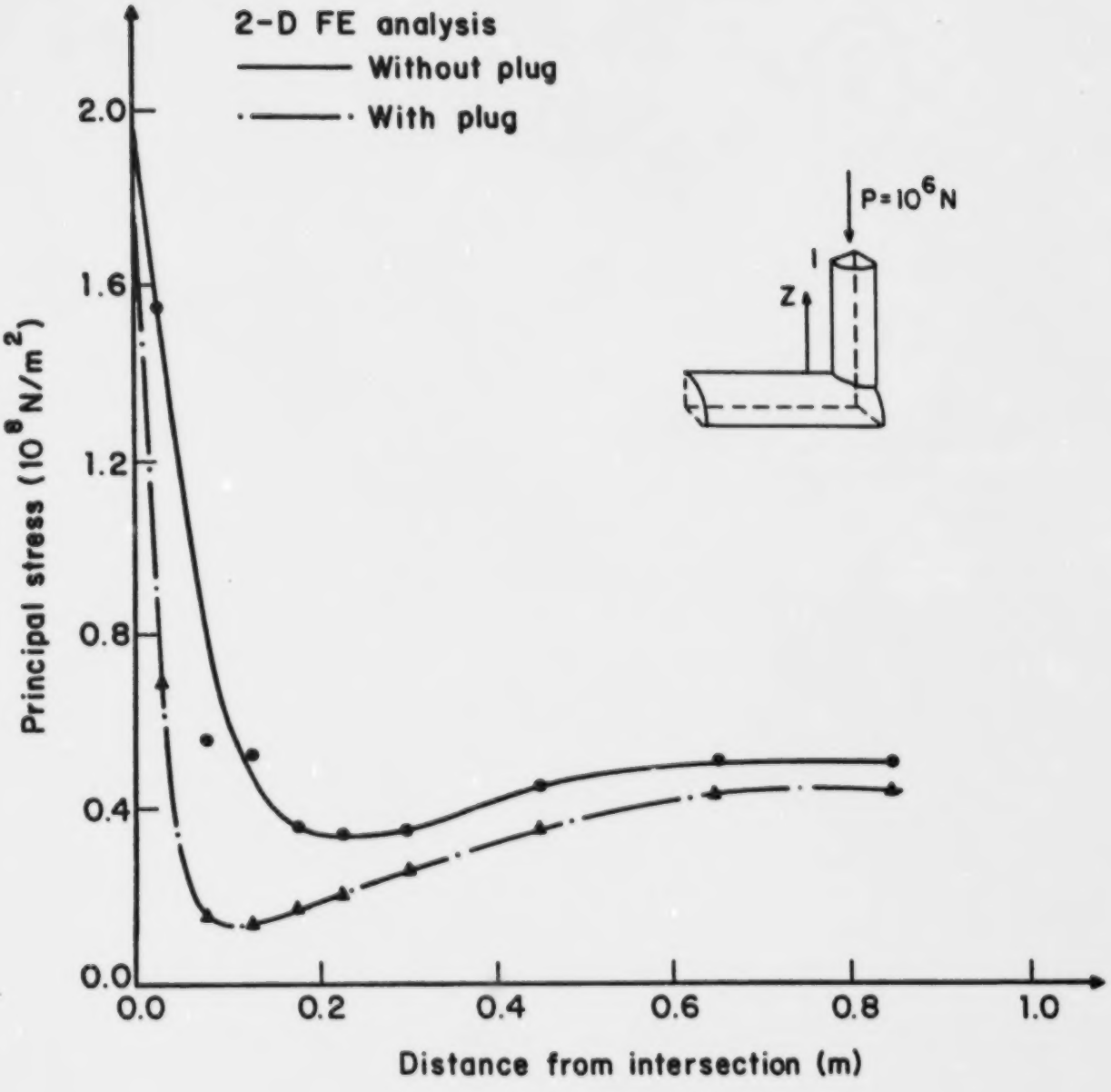

Fig. 3.15 Principal stress distribution: brace, line 1

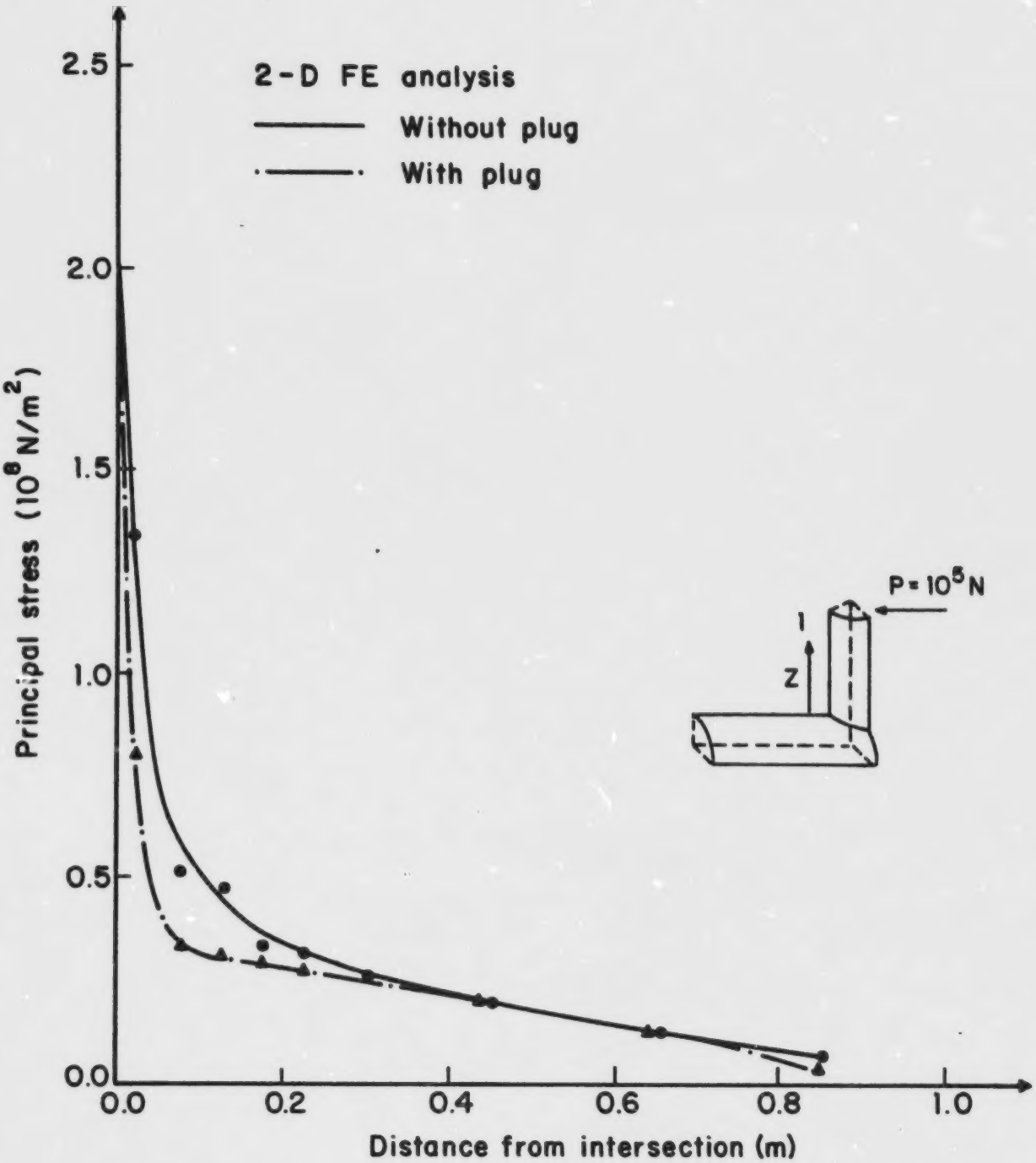

Fig. 3.16 Principal stress distribution: brace, line 1.

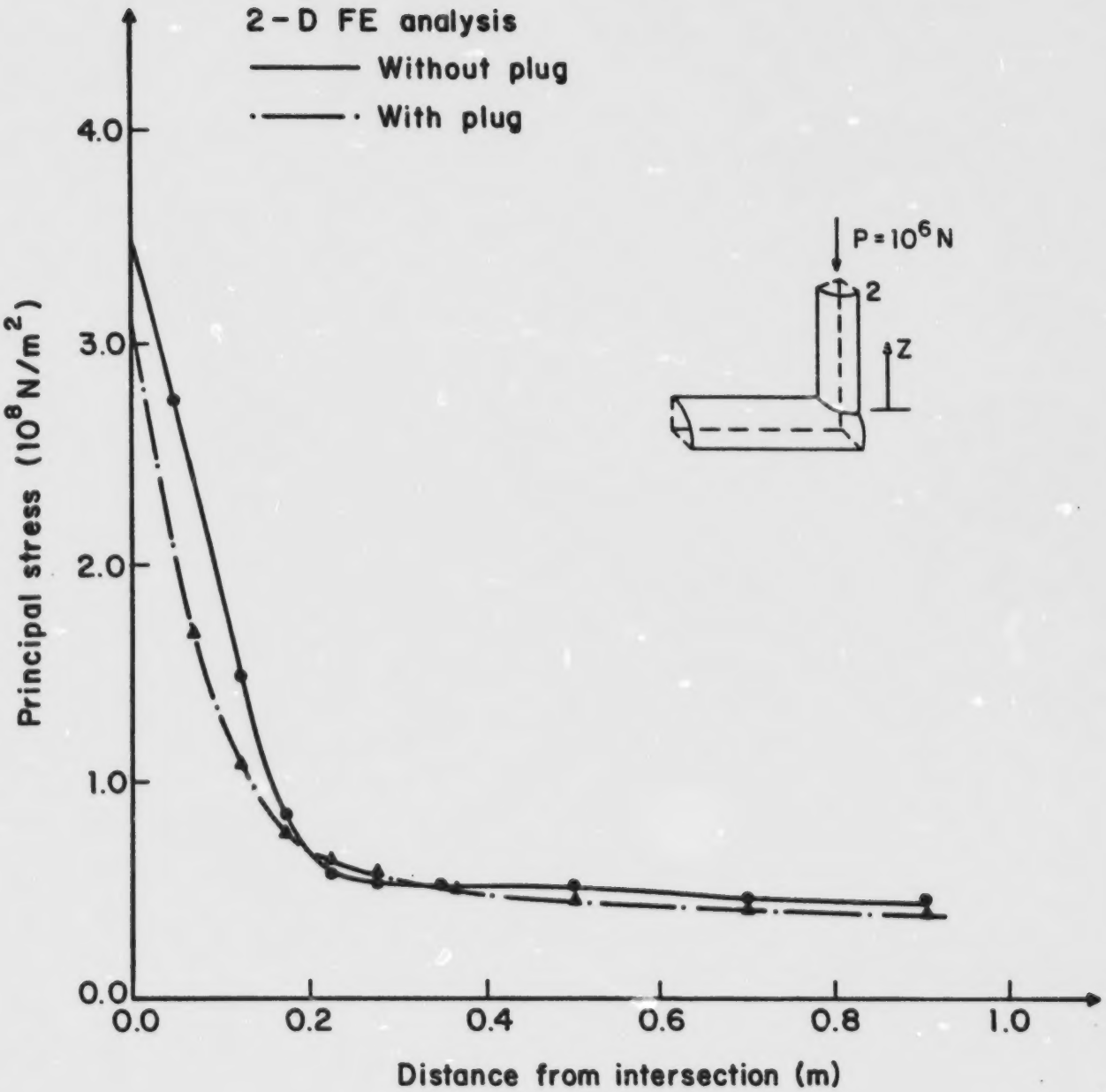

Fig. 3.17 Principal stress distribution: brace, line 2.

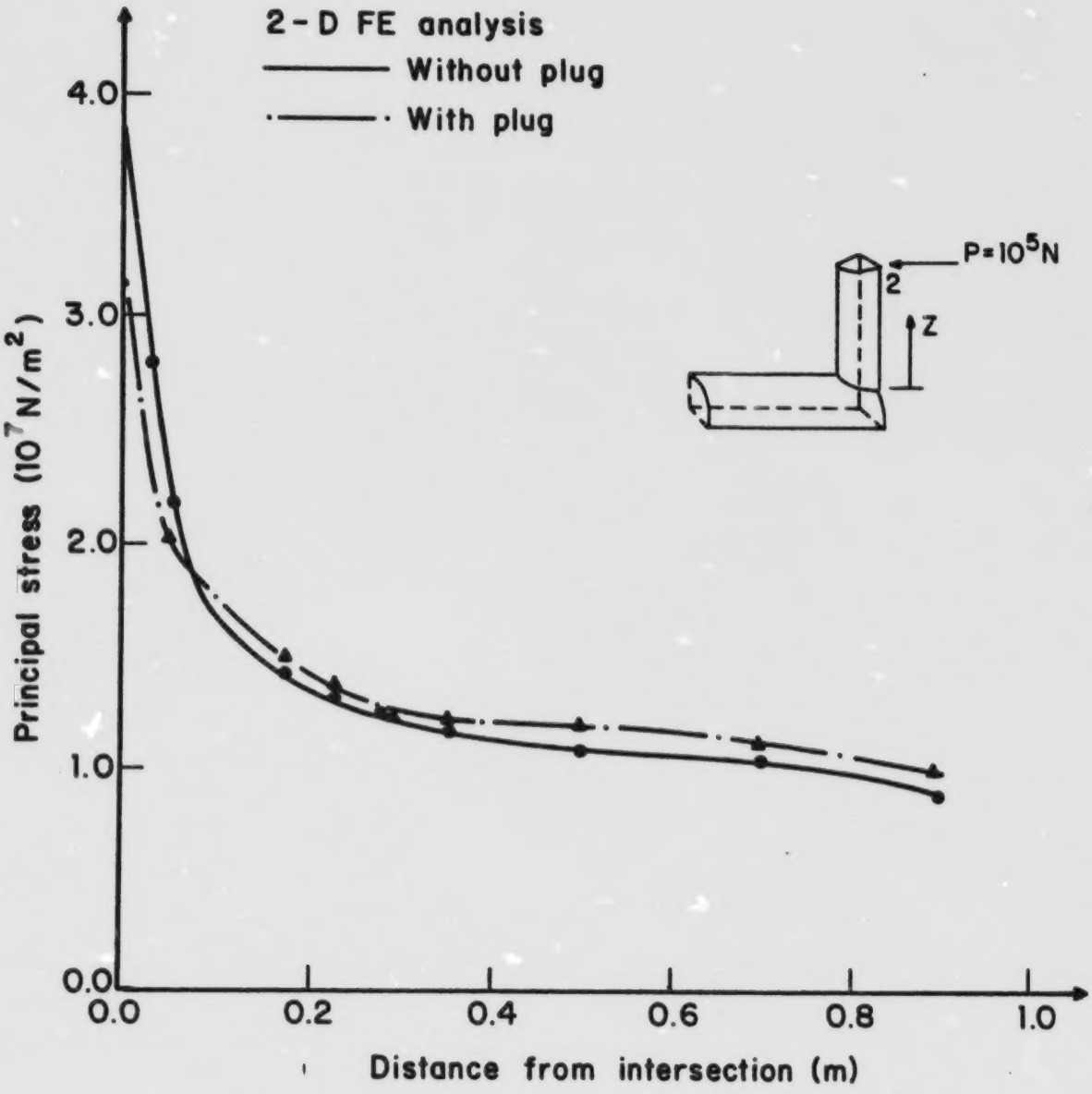

Fig. 3.18 Principal stress distribution: brace, line 2

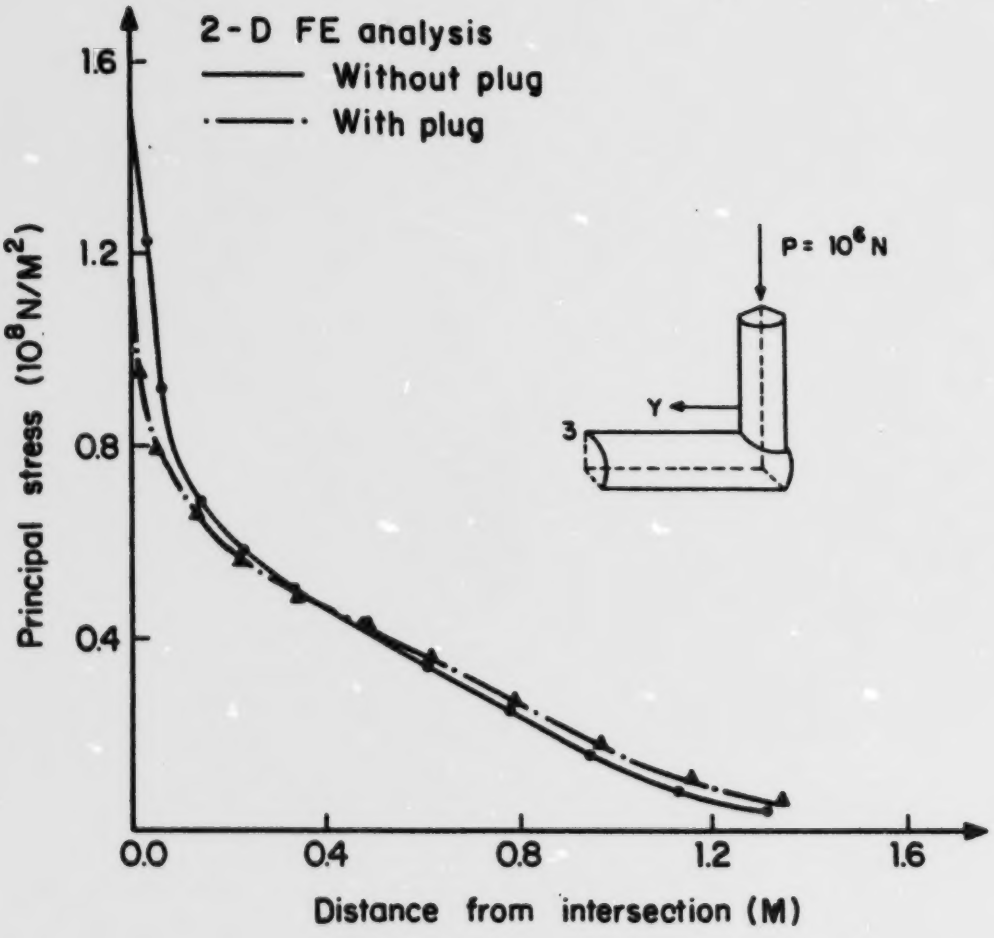

Fig. 3.19 Principal stress distribution: chord, line 3.

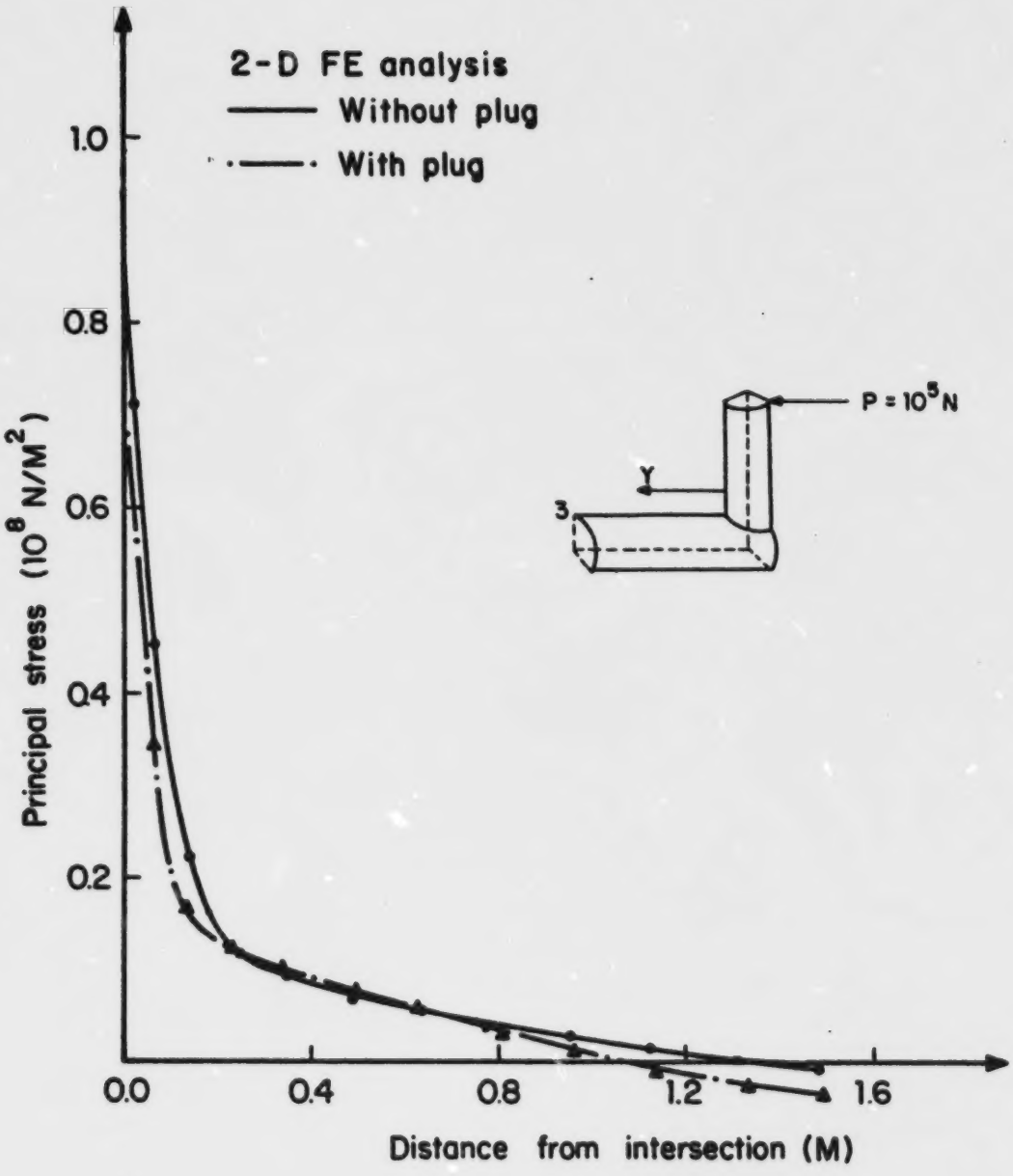

Fig. 3.20 Principal stress distribution: chord, line 3.

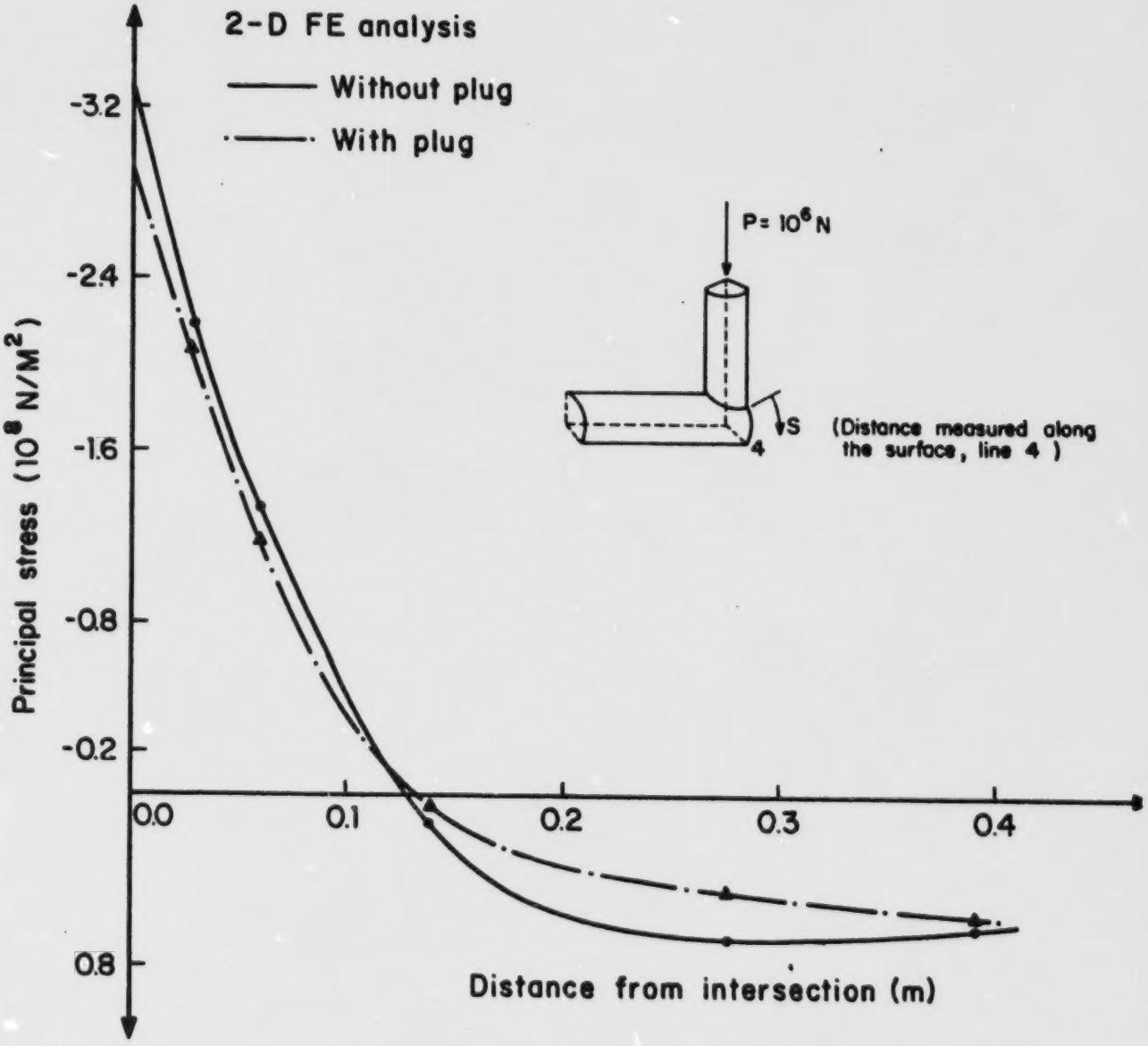

Fig. 3.21 Principal stress distribution: chord, line 4.

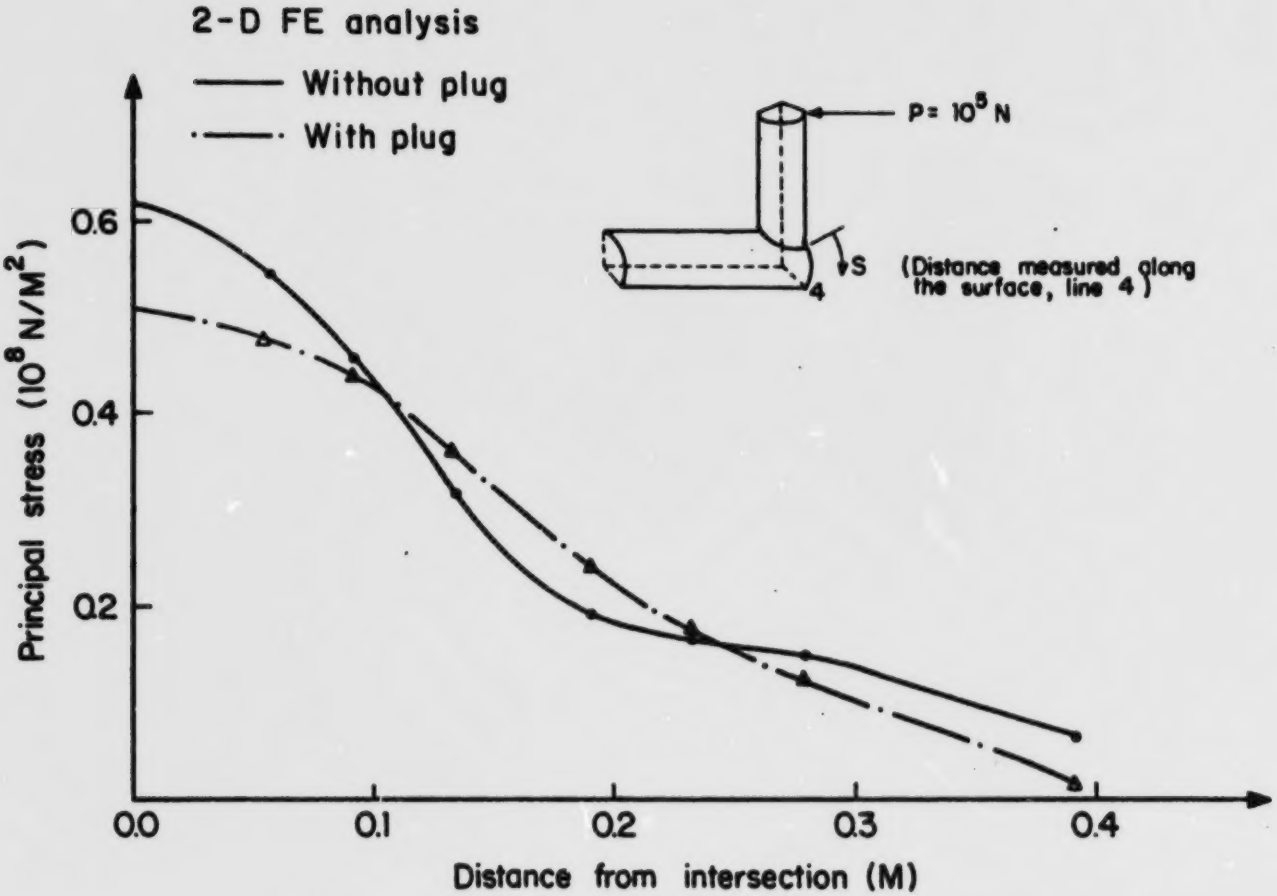

Fig. 3.22 Principal stress distribution: chord, line 4.

3.3.3 Brace stresses

The difference in stress concentration factors is observed between the measured values and those computed directly from the 2-dimensional analysis (Table 3.2). Finite element analysis tends to overestimate the brace-side SCFs due to the displaced brace/chord intersection (Fig. 3.23). The thickness of the chord wall and its resistance to shear results in the brace end rotating about and translating from a point, a, within the chord in between the chord-brace mid surface intersection and the point above, b, on the chord upper surface. To interpret the finite element results in terms of physical model stress values, the entire brace finite element representation is translated to the point, b, from the mid surface intersection.

Irvine [37] has attempted to explain the need for shift of the brace stresses. The required axial shift of brace stresses, Δ is given by

$$\Delta = \frac{1}{2} T - p + q \tag{3.31}$$

where T is chord wall thickness, p is a small positive correction factor, which can be expressed in terms of joint parameters as

$$p = \left\{0.0163 \frac{\tau}{\beta} + 0.297 \frac{\tau^{3/4}}{\beta^{1/4}}\right\} T \tag{3.32}$$

The term q in Eqn. 3.31 is a small positive correction for weld profile. For the T-joint under investigation, the value of Δ is 16 mm.

Loading in the brace distorts the chord, as shown in Fig. 3.23. The degree of ovalling of the chord is influenced primarily by the

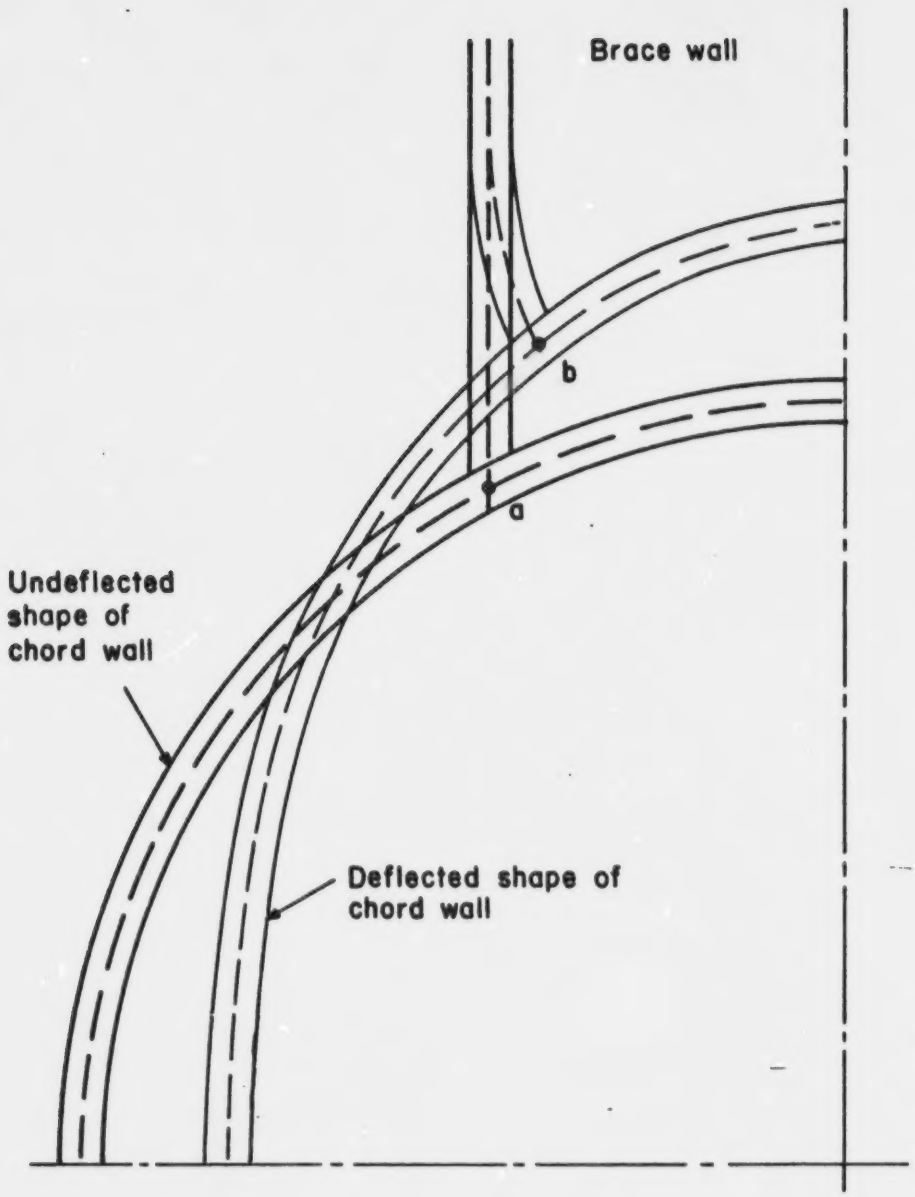

FIG. 3.23 SCHEMATIC OF DISPLACEMENTS ON THE PLANE OF SYMMETRY.

brace loading and the chord stiffness. Hence, the wall rotation at the end of the brace is dictated by the chord. The brace stresses are dependent upon the brace's end condition. The modified stress concentration factors for brace side are tabulated in Table 3.2, which show good agreement with the experimental values reported in the literature. The brace stresses after axial shifting are shown in Figs. 3.24 - 3.27.

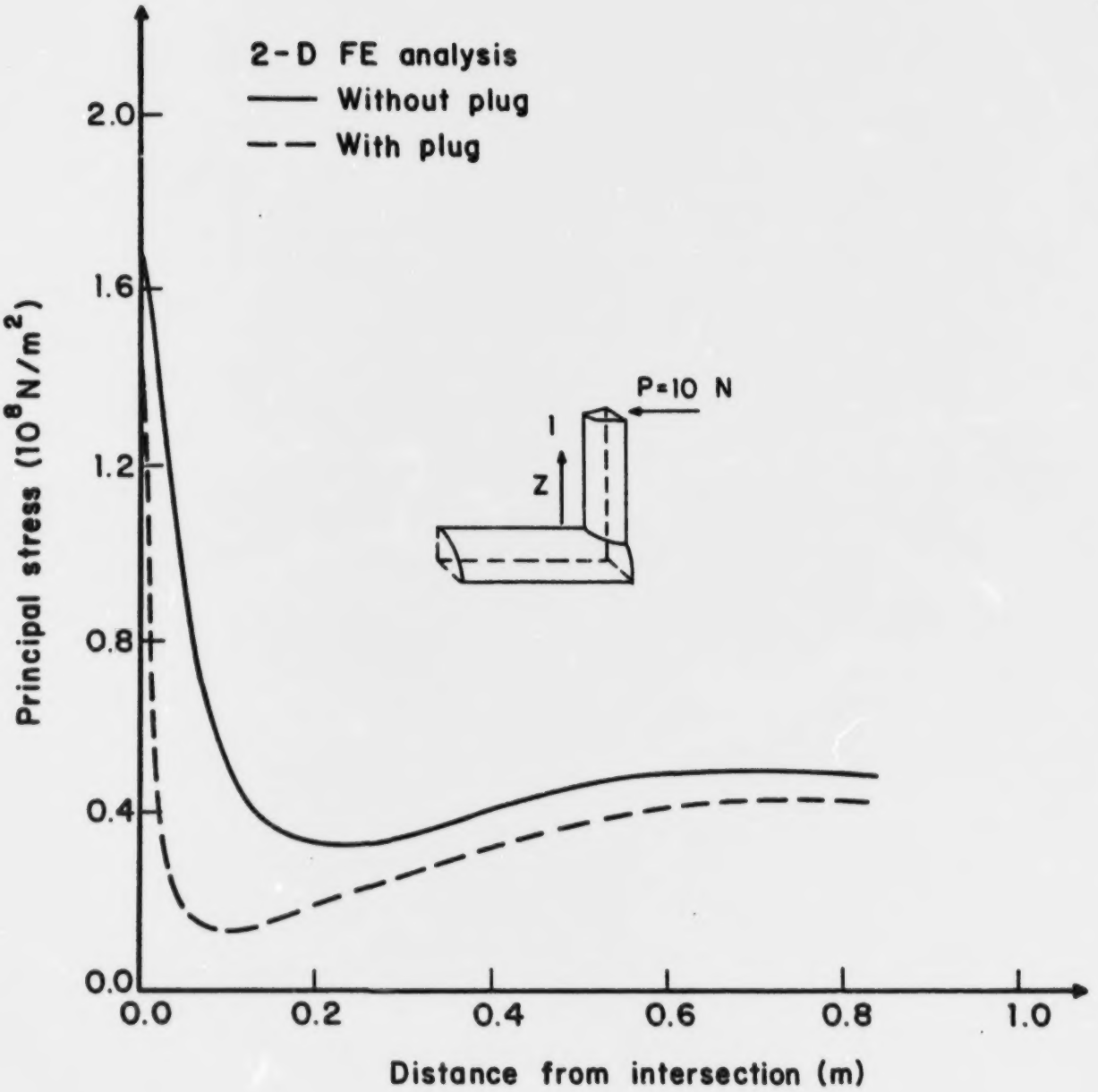

Fig. 3.24 Modified principal stress distribution after axial shifting: brace, line 1.

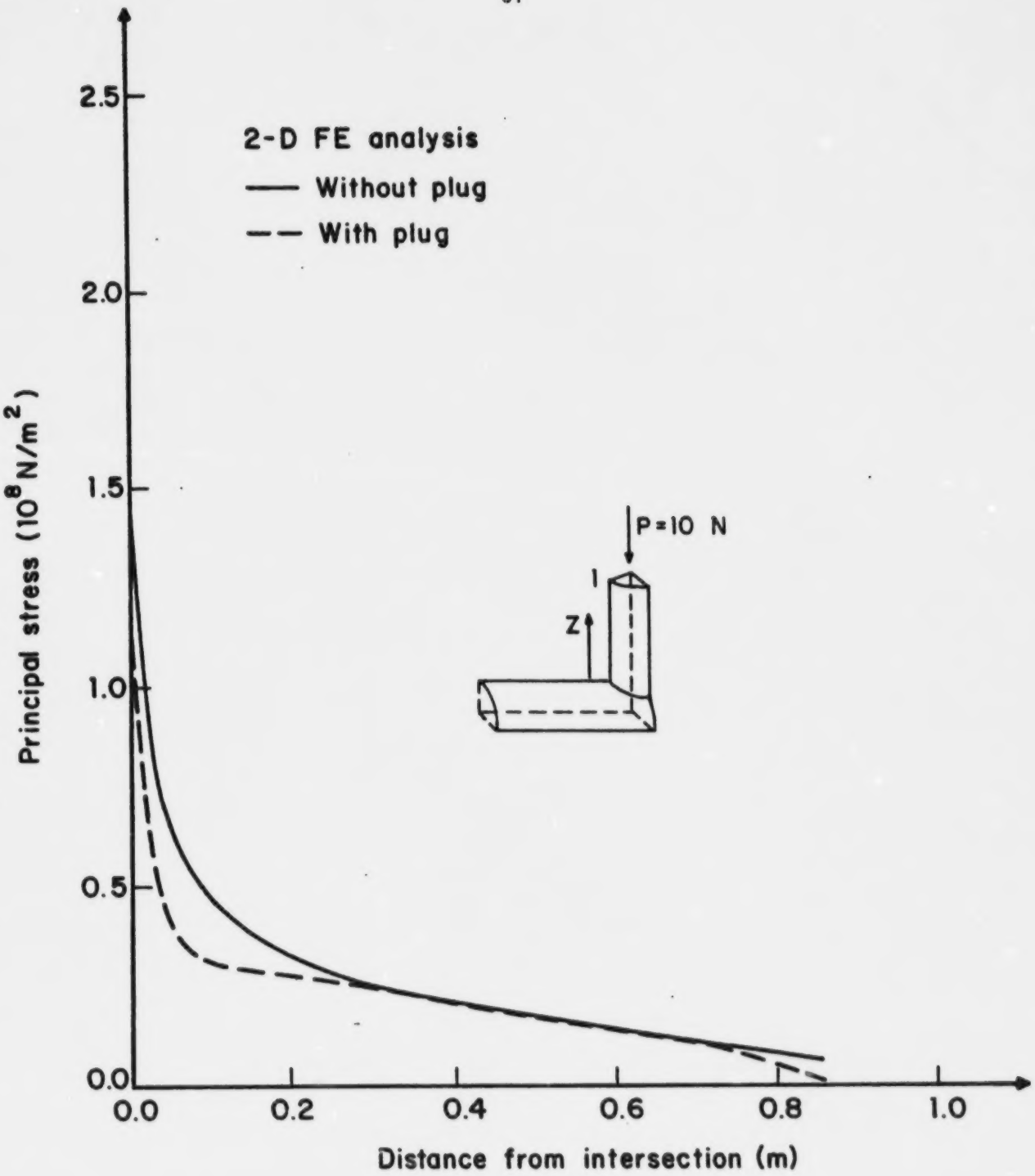

Fig. 3.25 Modified principal stress distribution after axial shifting: brace, line 1.

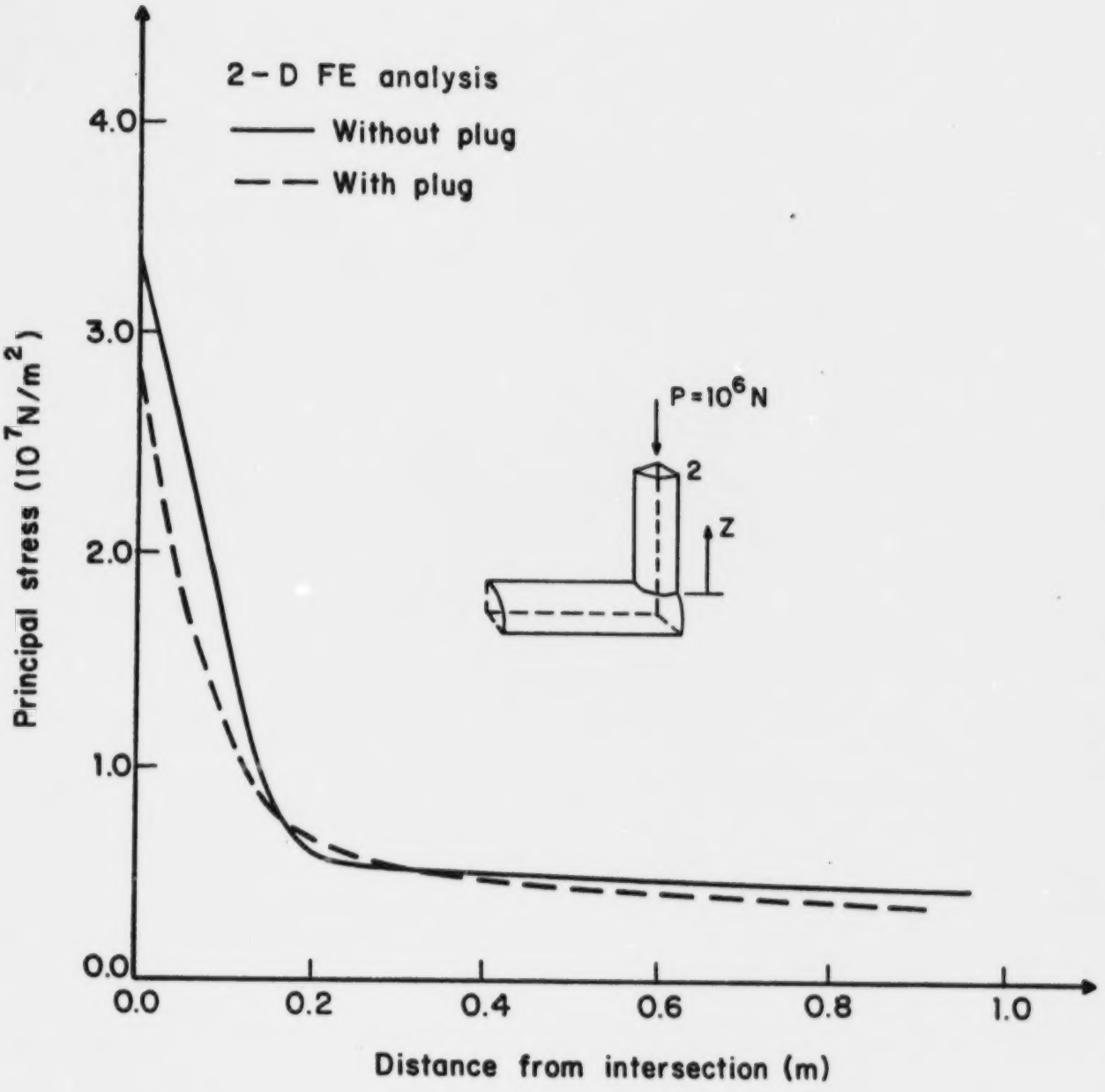

Fig. 3.26 Modified principal stress distribution after axial shifting: brace, line 2

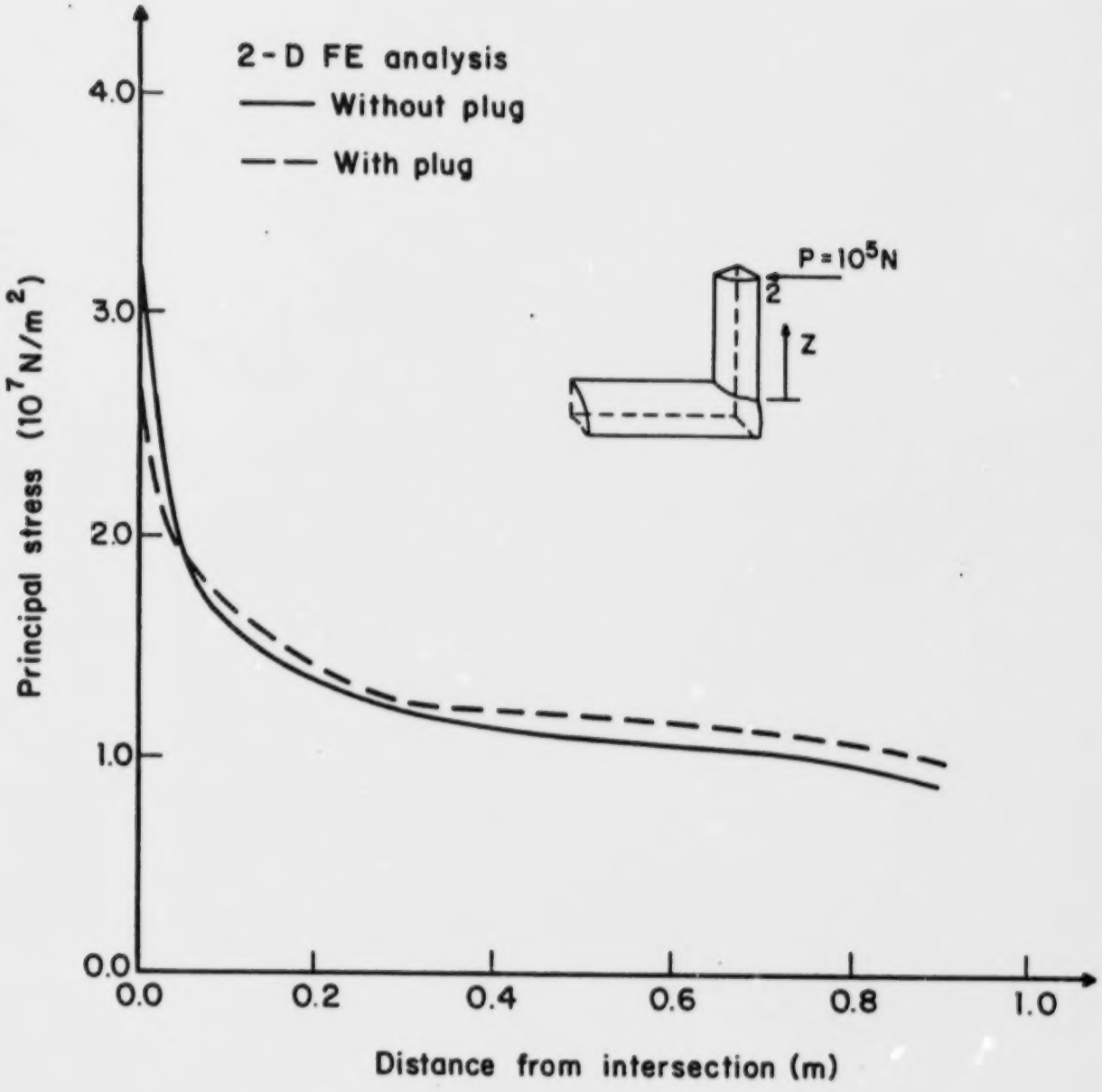

Fig. 3.27 Modified principal stress distribution after axial shifting: brace, line 2

CHAPTER IV

4. THREE DIMENSIONAL STRESS ANALYSIS INCLUDING REZONE TECHNIQUE

4.1 Introduction

The tubular joint is analysed in Chapter III using the plate and shell element, in which the joint is idealized by the midsurface of the chord and brace. The thickness of the shell element is used only in the computation of the membrane and flexural stiffnesses. It is not considered in the physical modelling of the joint and the consequent through thickness variation of displacements and the resulting stresses. The plate and shell element idealisation also does not permit consideration of the weld profile and the actual chord interaction.

This chapter presents the effect of the three dimensional idealisation of the joint including the weld reinforcement based on the modelling of i) the entire T-joint, and ii) the region around the hot spot using rezone technique.

4.2 Modelling of the Entire T-Joint

4.2.1 Element stiffness formulation

The displacements u_i, v_i and w_i along x, y and z axes at each node are taken as the nodal degrees of freedom. The faces of the 8-node incompatible brick element (Fig. 4.1) are defined by local coordinates $\xi, \eta, \zeta = \pm 1$. The global coordinates are defined as

$$x = \sum_{i=1}^{8} N_i \, x_i$$

$$y = \sum_{i=1}^{8} N_i \, y_i \qquad (4.1)$$

$$z = \sum_{i=1}^{8} N_i \, z_i$$

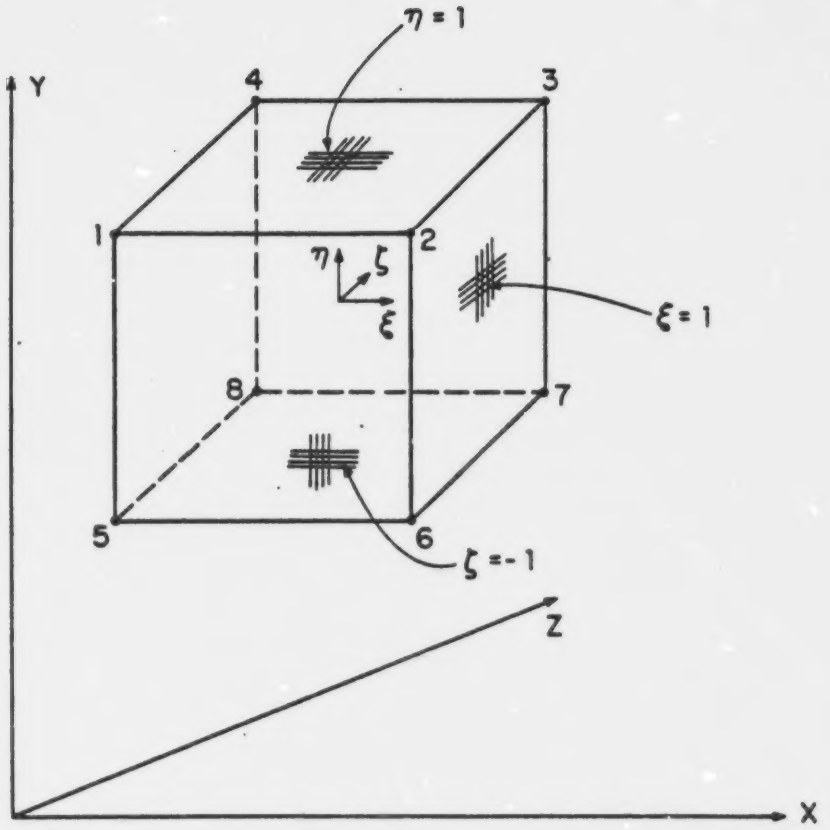

FIG. 4.1 THREE-DIMENSIONAL 8-NODE ELEMENT

where x_i, y_i and z_i are the element nodal point coordinates and N_i is the shape function which is given by

$$N_i = \frac{1}{8}(1 + \xi\xi_i)(1 + \eta\eta_i)(1 + \zeta\zeta_i) \tag{4.2}$$

To improve the flexural characteristics of 8-node isoparametric brick elements, three incompatible modes are introduced in the displacement interpolation functions. The global displacements u, v and w at any point within the element can be expressed as

$$\begin{aligned} u &= \sum_{i=1}^{8} N_i u_i + \sum_{j=1}^{3} g_j \alpha_j \\ v &= \sum_{i=1}^{8} N_i v_i + \sum_{j=1}^{3} g_j \beta_j \\ w &= \sum_{i=1}^{8} N_i w_i + \sum_{j=1}^{3} g_j \gamma_j \end{aligned} \tag{4.3}$$

where $g_j (j=1,2,3)$ are the additional shape functions for the incompatible element and α_j, β_j and γ_j are the generalized displacement coordinates. The first term of the right hand side of Eqn. 4.3 represents the polynomial corresponding to the basic element. The displacements due to the terms in the polynomial of the basic element are continuous across the interface of the element, but those due to the second terms in Eqn. 4.3 are not necessarily continuous across the element boundaries. The incompatible shape functions g_j are given as

$$\begin{aligned} g_1 &= (1-\xi^2) \\ g_2 &= (1-\eta^2) \\ g_3 &= (1-\zeta^2) \end{aligned} \tag{4.4}$$

The stress-strain relations are

$$\{\sigma\} = \{\sigma_x \ \sigma_y \ \sigma_z \ \tau_{xy} \ \tau_{yx} \ \tau_{zx}\}^T = [D]\ \{\epsilon\}$$

$$= [D]\ \{\epsilon_x \ \epsilon_y \ \epsilon_z \ \gamma_{xy} \ \gamma_{yz} \ \gamma_{zx}\}^T \tag{4.5}$$

where

[D] = the elasticity matrix, which is given by

$$[D] = \frac{E(1-\nu)}{(1+\nu)(1-2\nu)} \begin{bmatrix} 1 & \frac{\nu}{(1-\nu)} & \frac{\nu}{(1-\nu)} & 0 & 0 & 0 \\ & 1 & \frac{\nu}{(1-\nu)} & 0 & 0 & 0 \\ & & 1 & 0 & 0 & 0 \\ & \text{sym.} & & \frac{(1-2\nu)}{2(1-\nu)} & 0 & 0 \\ & & & & \frac{(1-2\nu)}{2(1-\nu)} & 0 \\ & & & & & \frac{(1-2\nu)}{2(1-\nu)} \end{bmatrix} \tag{4.6}$$

The strain-displacement relation of the element can be written as

$$\{\epsilon\} = [B_1 \ | \ B_2] \begin{Bmatrix} a_1 \\ -- \\ a_2 \end{Bmatrix} \tag{4.7}$$

where

$$\{a_{1i}\} = \{u_i \ v_i \ w_i\}^T, \text{ for } i = 1 \text{ to } 8 \tag{4.8}$$

are the element nodal point displacements, and

$$\{a_2\} = \{\alpha_1 \ \beta_1 \ \gamma_1 \ \alpha_2 \ \beta_2 \ \gamma_2 \ \alpha_3 \ \beta_3 \ \gamma_3\}^T \tag{4.9}$$

are the element generalized coordinates due to the incompatible modes. The submatrices $[B_1]$ and $[B_2]$ contain the derivatives of functions N and g respectively. The general forms of the submatrices $[B_1]$ and $[B_2]$ are given by

$$[B_{1i}] = \begin{bmatrix} \frac{\partial N_i}{\partial x} & 0 & 0 \\ 0 & \frac{\partial N_i}{\partial y} & 0 \\ 0 & 0 & \frac{\partial N_i}{\partial z} \\ \frac{\partial N_i}{\partial y} & \frac{\partial N_i}{\partial x} & 0 \\ 0 & \frac{\partial N_i}{\partial z} & \frac{\partial N_i}{\partial y} \\ \frac{\partial N_i}{\partial z} & 0 & \frac{\partial N_i}{\partial x} \end{bmatrix} \tag{4.10}$$

and

$$[B_{2i}] = \begin{bmatrix} \frac{\partial g_i}{\partial x} & 0 & 0 \\ 0 & \frac{\partial g_i}{\partial y} & 0 \\ 0 & 0 & \frac{\partial g_i}{\partial z} \\ \frac{\partial g_i}{\partial y} & \frac{\partial g_i}{\partial x} & 0 \\ 0 & \frac{\partial g_i}{\partial z} & \frac{\partial g_i}{\partial y} \\ \frac{\partial g_i}{\partial z} & 0 & \frac{\partial g_i}{\partial x} \end{bmatrix} \tag{4.11}$$

The global and local derivatives of the shape functions are related by the equation

$$\begin{bmatrix} \frac{\partial N_i}{\partial x} \\ \frac{\partial N_i}{\partial y} \\ \frac{\partial N_i}{\partial z} \end{bmatrix} = [J]^{-1} \begin{bmatrix} \frac{\partial N_i}{\partial \xi} \\ \frac{\partial N_i}{\partial \eta} \\ \frac{\partial N_i}{\partial \zeta} \end{bmatrix} \tag{4.12}$$

where

[J] = Jacobian matrix, which is given by

$$[J] = \begin{bmatrix} \Sigma \frac{\partial N_i}{\partial \xi} x_i & \Sigma \frac{\partial N_i}{\partial \xi} y_i & \Sigma \frac{\partial N_i}{\partial \xi} z_i \\ \Sigma \frac{\partial N_i}{\partial \eta} x_i & \Sigma \frac{\partial N_i}{\partial \eta} y_i & \Sigma \frac{\partial N_i}{\partial \eta} z_i \\ \Sigma \frac{\partial N_i}{\partial \zeta} x_i & \Sigma \frac{\partial N_i}{\partial \zeta} y_i & \Sigma \frac{\partial N_i}{\partial \zeta} z_i \end{bmatrix} \tag{4.13}$$

The equilibrium equations for the element can be written as

$$\left[\begin{array}{c|c} [K_{11}] & [K_{12}] \\ \hline [K_{21}] & [K_{22}] \end{array}\right] \left\{\begin{array}{c} \{\alpha_1\} \\ \hline \{a_2\} \end{array}\right\} = \left\{\begin{array}{c} \{F_1\} \\ \hline \{F_2\} \end{array}\right\} \tag{4.14}$$

where

$$[K_{ij}] = \int_{-1}^{1} \int_{-1}^{1} \int_{-1}^{1} [B_i]^T [D] [B_j] |J| \, d\xi \, d\eta \, d\zeta \tag{4.15}$$

are the submatrices of the element stiffness matrix. $\{F_1\}$ is the element load vector containing equivalent nodal forces. $\{F_2\}$ represents the forces in terms of the element generalized coordinates contributed by only thermal loading; in the present case $\{F_2\} = \{0\}$.

Before assembling the global stiffness matrix, the incompatible degrees of freedom $\{a_2\}$ in Eqn. 4.14 are condensed out to get the resulting equation

$$[\bar{K}_{11}]\ \{a_1\} = \{F_1\} \tag{4.16}$$

where

$$[\bar{K}_{11}] = [K_{11}] - [K_{12}]\ [K_{22}]^{-1}\ [K_{21}] \tag{4.17}$$

Eqn. 4.16 is used to assemble the global stiffness matrix and nodal displacements are then computed. The incompatible degrees of freedom $\{a_2\}$ are calculated as

$$\{a_2\} = -[K_{21}]\ \{a_1\} \tag{4.18}$$

Knowing the displacements, $\{a_1\}$ and $\{a_2\}$ the element strains and corresponding stresses are obtained using Eqns. 4.7 and 4.5 respectively.

The 6-node incompatible prism element stiffness matrix is derived in a similar manner from the 8-node incompatible brick element by coalescing the nodes 1, 2 and 5, 6 (Fig. 4.2).

4.3 Modelling of Hot Spot Region Using Rezone Technique

4.3.1 Introduction

The rezone technique is used to reduce the computer storage requirements as well as solution costs that result from the large number of degrees-of-freedom associated with the 3-dimensional elements. This section presents the use of the rezone technique to obtain an accurate estimate of stresses at the intersection of the

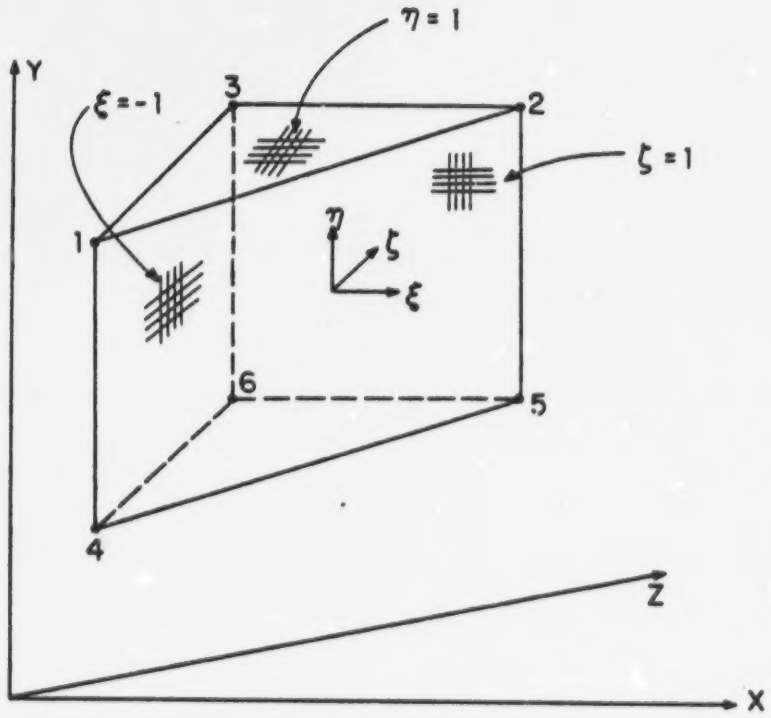

FIG. 4.2 6-NODE PRISM ELEMENT

brace and chord including the through thickness and weld reinforcement effects. The hot spot region around the weld toe and the weld reinforcement are modelled using three dimensional incompatible 8 node brick and 6 node prism elements. Using the results of the two dimensional analysis, the boundary nodal forces/displacements are obtained as discussed in section 4.3.2. The surface stresses at the critical locations of the brace-chord intersection including the through thickness distribution are compared with those obtained from the three dimensional modelling of the entire joint.

4.3.2 Rezone sections

Typical rezoned regions, around the saddle point and crown point at the brace/chord intersection are shown in Figs. 4.3 and 4.4. A schematic example of the transition of a typical plate to solid element is shown in Fig. 4.5, in which one inner surface and one outer surface brick element node are assigned to each plate element node. Therefore, the plate element's boundary solutions i.e. the displacements or forces are applied entirely to brick element nodes defined at the inner and outer surfaces of a shell (Fig. 4.6) The shell surface normal directions for all nodal locations at the plate-to-solid transition are defined as cylinder radius vector through the transition node. The cylinder is defined by the coordinates of two points along the centre line of the shell (Fig. 4.7). The six boundary variables are distributed between two 3D-solid element nodes maintaining boundary compatibility of displacement or boundary force equilibrium, because three translational degrees-of-freedom are assigned to the solid element.

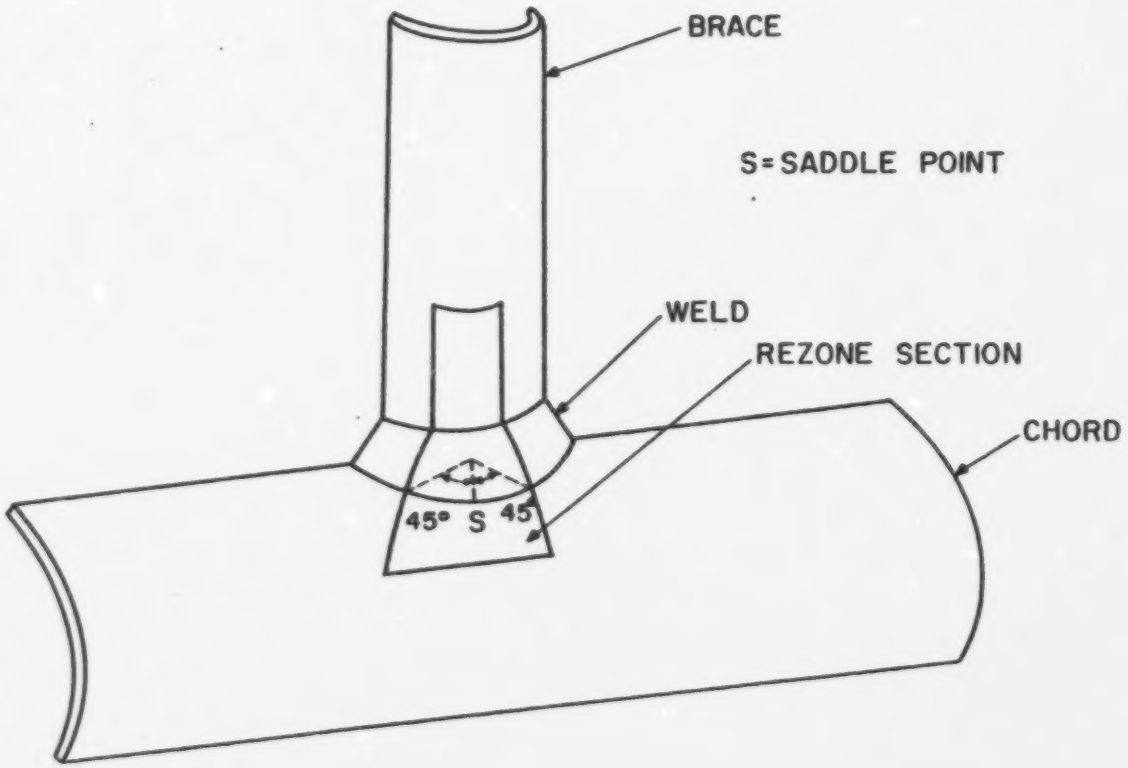

FIG. 4.3 REZONE SECTION AT SADDLE POINT.

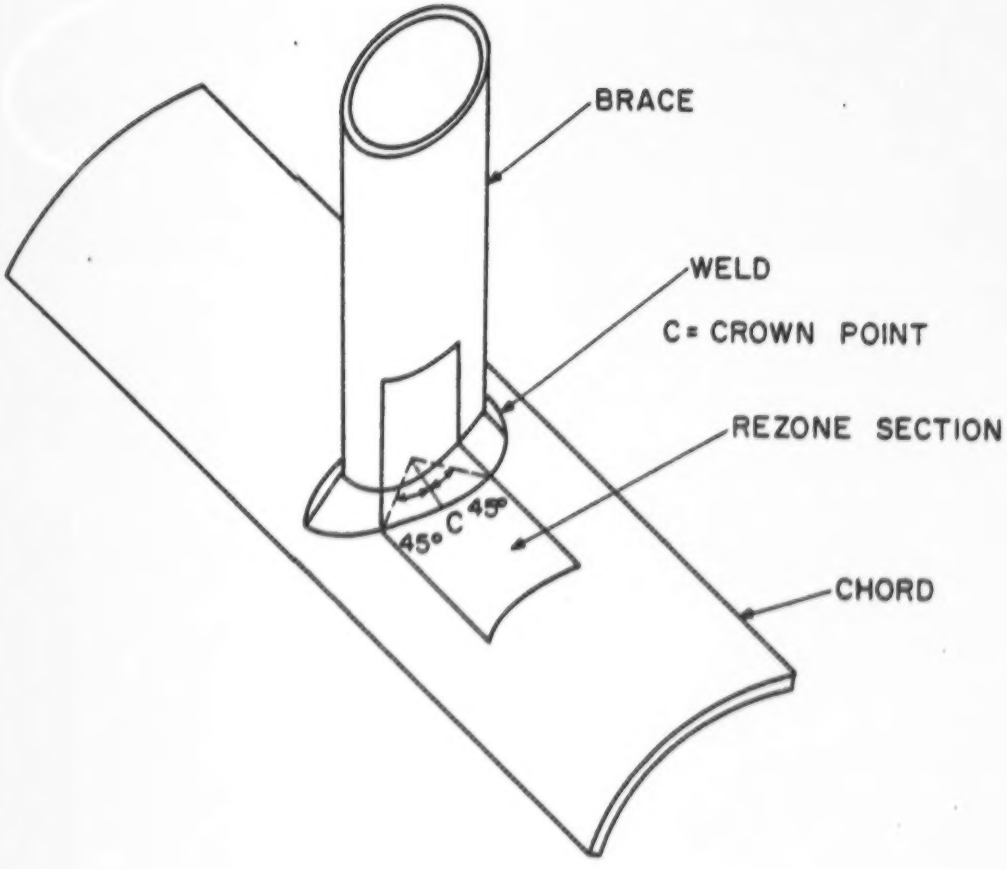

FIG. 4.4 REZONE SECTION AT CROWN POINT.

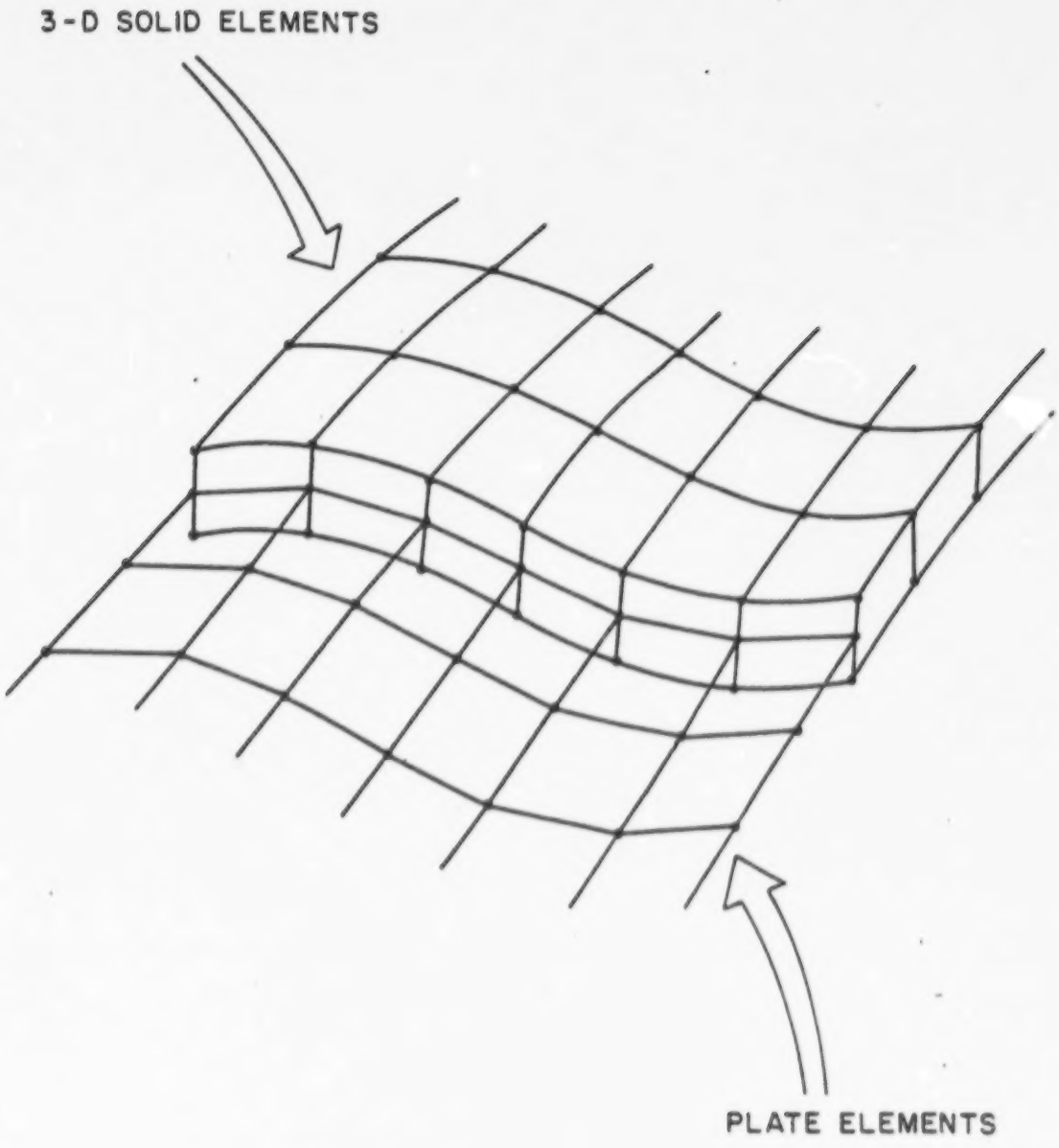

FIG. 4.5 PLATE-TO-SOLID ELEMENT TRANSITION

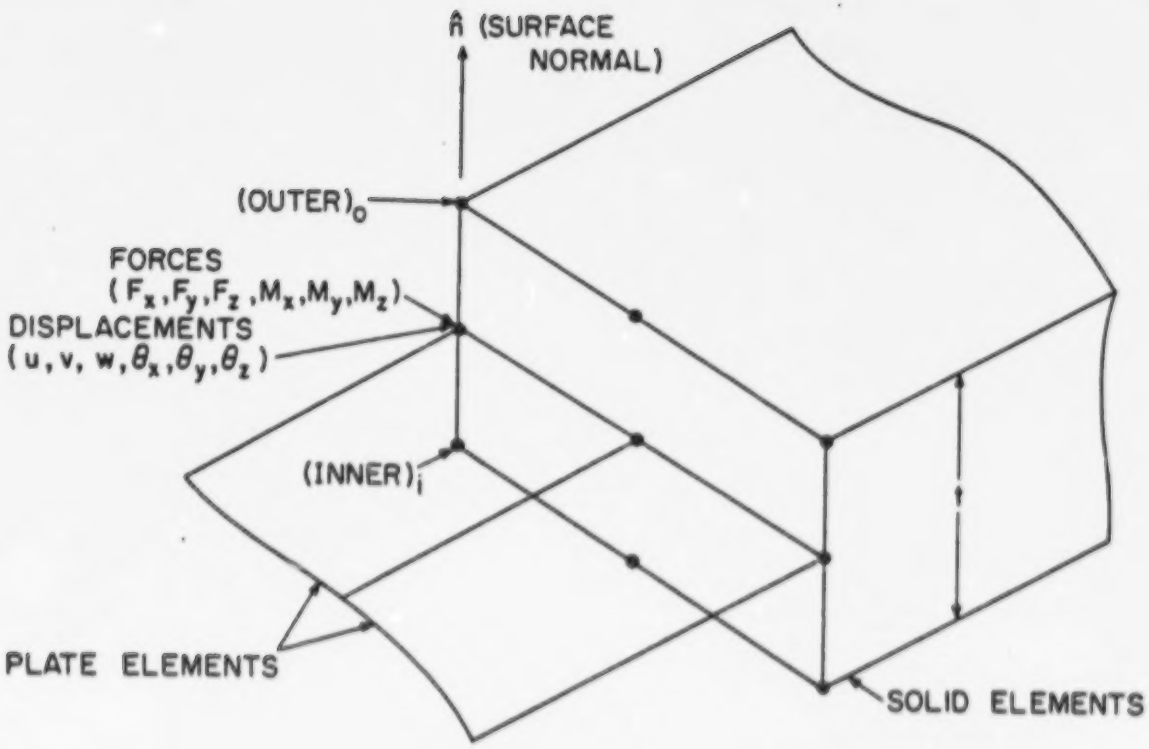

FIG. 46 EXPANDED VIEW OF PLATE-TO-SOLID ELEMENT TRANSITION.

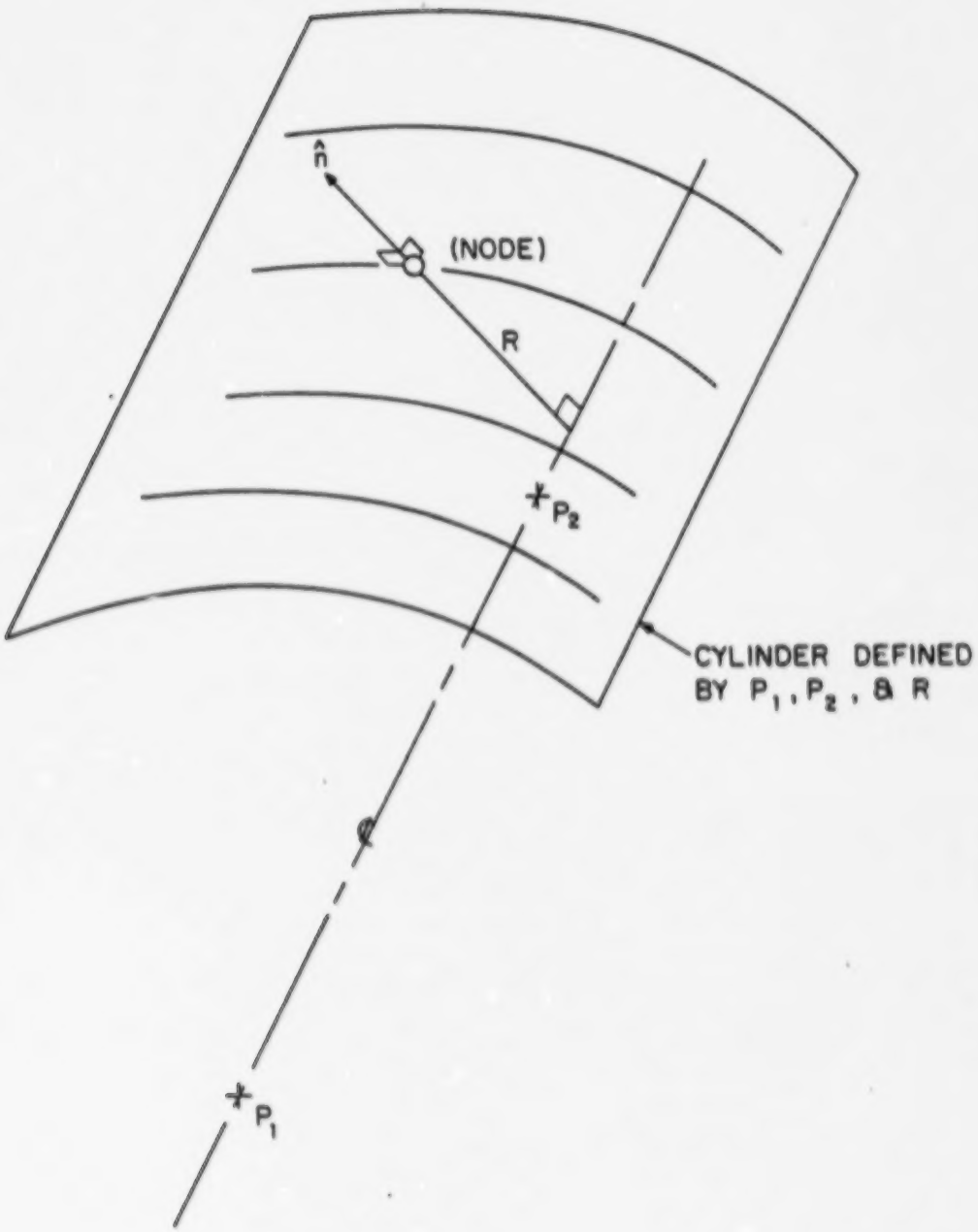

FIG. 4.7 DEFINITION OF SURFACE NORMAL FOR A CYLINDRICAL SURFACE.

The directional cosines cos α, cos β and cos γ are defined in the x,y,z cartesian system as shown in Fig. 4.8. The coordinates x_o, y_o, z_o and x_i, y_i, z_i of the outer and inner surface transition nodes are respectively

$$\begin{aligned} x_o &= x + t/2 \cos \alpha \\ y_o &= y + t/2 \cos \beta \\ z_o &= z + t/2 \cos \gamma \\ x_i &= x - t/2 \cos \alpha \\ y_i &= y - t/2 \cos \beta \\ z_i &= z - t/2 \cos \gamma \end{aligned} \tag{4.19}$$

where t = shell thickness and x,y,z = plate element nodal coordinates at the transition.

Displacement transformation

The boundary displacements applied to the surface nodes of brick element at transition are derived from the combined translation and rotation of the matching plate element node. The initial position vector of the surface node are defined by the outward normal vector extended from the plate element node to the outer surface node of solid element (Fig. 4.9). The projection of this position vector onto x-z plane, $\hat{n}_y$, makes an inclination, λ_{yx} with the z-axis which is given by

$$\lambda_{yx} = \sin^{-1}\left[\frac{\cos \alpha}{\text{Sin } \beta}\right] \tag{4.20}$$

Due to the y-axis rotation of the plate element node, θ_y, the position vector, $\hat{n}_y$, of the surface node is rotated to a new position, $\hat{n}'_y$, causing the partial translation in the x-direction, $\Delta x_o(\theta_y)$, which is

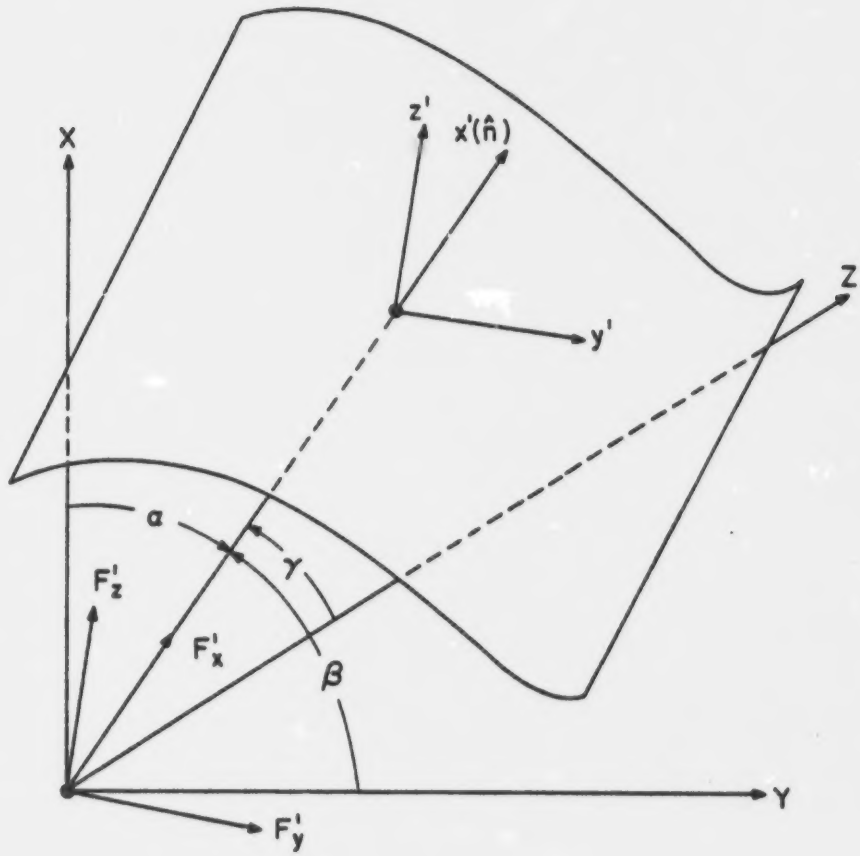

FIG. 4.8 SHELL SURFACE LOCAL COORDINATE SYSTEM DEFINITION.

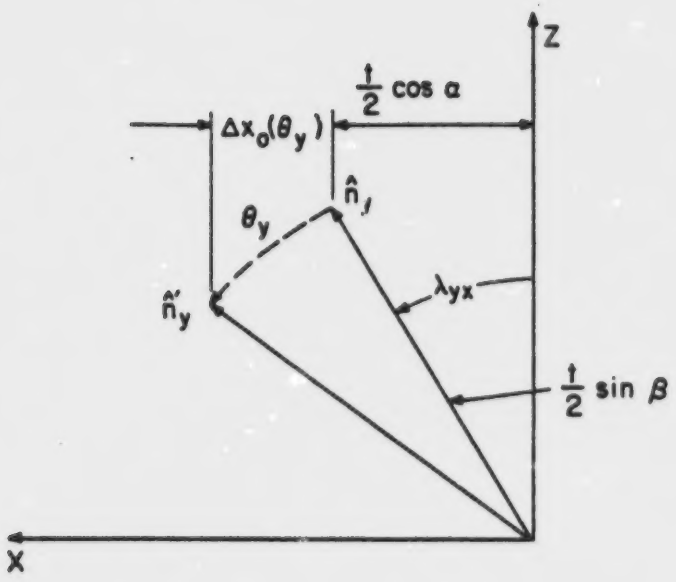

FIG. 4.9 TRANSLATION OF SURFACE NODE DUE TO ROTATION OF PLATE NODE ABOUT Y-AXIS.

$$\Delta x_o(\theta_y) = \frac{t}{2} \sin\beta \sin(\lambda_{yx} + \theta_y) - \frac{t}{2}\cos\alpha \qquad (4.21)$$

Similarly the x-direction translation due to rotation about the z-axis, is given by (Fig. 4.10)

$$\Delta x_o(\theta_z) = \frac{t}{2} \sin\gamma \sin(\lambda_{zx} - \theta_z) - \frac{t}{2}\cos\alpha \qquad (4.22)$$

where

$$\lambda_{zx} = \sin^{-1}\left(\frac{\cos\alpha}{\sin\gamma}\right) \qquad (4.23)$$

So the total displacement in x-direction of the outer surface node of the solid element, Δx_o, at transition node due to the x-translation (Δx), y-rotation (θ_y) and z-rotation (θ_z) of the plate node is

$$\Delta x_o = \Delta x + \Delta x_o(\theta_y) + \Delta x_o(\theta_z) \qquad (4.24)$$

Similarly, the total displacements in y and z directions of the outer surface node of solid element Δy_o, Δz_o are derived. Assuming the rigid body movement of the solid element edge, the total x, y, and z-displacements of the inner surface node Δx_i, Δy_i and Δz_i are obtained. The surface node displacements are

$$\Delta x_o = \Delta x + \left(\frac{t}{2}\right)[\sin\beta \sin(\lambda_{yx}+\theta_y) + \sin\gamma \sin(\lambda_{zx}-\theta_z) - 2\cos\alpha]$$

$$\Delta y_o = \Delta y + \left(\frac{t}{2}\right)[\sin\gamma \sin(\lambda_{zy}+\theta_z) + \sin\alpha \sin(\lambda_{xy}-\theta_x) - 2\cos\beta]$$

$$\Delta z_o = \Delta z + \left(\frac{t}{2}\right)[\sin\alpha \sin(\lambda_{xz}+\theta_x) + \sin\beta \sin(\lambda_{yz}-\theta_y) - 2\cos\gamma]$$

$$\Delta x_i = 2(\Delta x) - \Delta x_o$$

$$\Delta y_i = 2(\Delta y) - \Delta y_o \qquad (4.25)$$

$$\Delta z_i = 2(\Delta z) - \Delta z_o$$

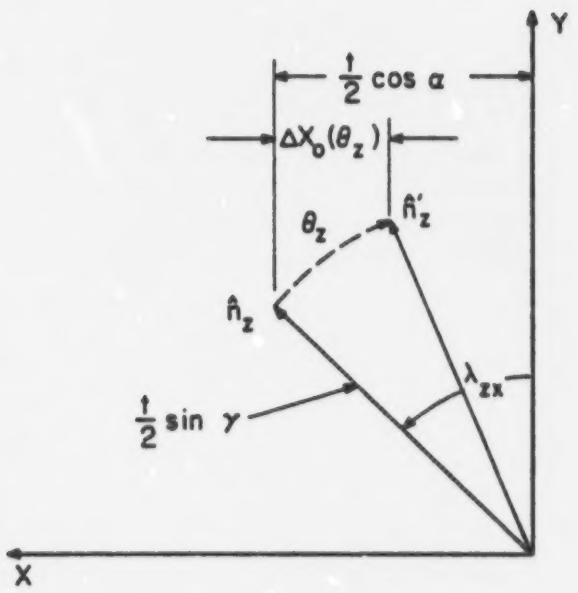

FIG. 4.10 TRANSLATION OF SURFACE NODE DUE TO ROTATION OF PLATE NODE ABOUT Z-AXIS.

where

$$\lambda_{yx} = \sin^{-1}\left(\frac{\cos\alpha}{\sin\beta}\right) \qquad \lambda_{zx} = \sin^{-1}\left(\frac{\cos\alpha}{\sin\gamma}\right)$$

$$\lambda_{zy} = \sin^{-1}\left(\frac{\cos\beta}{\sin\gamma}\right) \qquad \lambda_{xy} = \sin^{-1}\left(\frac{\cos\beta}{\sin\alpha}\right) \tag{4.26}$$

$$\lambda_{xz} = \sin^{-1}\left(\frac{\cos\gamma}{\sin\alpha}\right) \qquad \lambda_{yz} = \sin^{-1}\left(\frac{\cos\gamma}{\sin\beta}\right)$$

Force transformation

Derivations of the force transformation relations are considerably more involved than those of the displacement transformations. There are only two orthogonal coordinate directions which are used to balance the plate element's midplane moments with 3-D element's surface nodal forces. Forces applied to the third coordinate direction (in line with the surface normal vector) would not produce moments about the midplane since the force line intersects that node. Since there are three moments and three forces associated with the plate element's node, a special shell coordinate system is established in order to balance the moments with the surface forces. There would be no component of moment parallel to the shell normal vector due to the fact that plate elements carry no in-plane rotational stiffness. By defining a local shell normal vector, the surface nodal forces are determined such that equilibrium is preserved for the three components of force and two components of moment in the plane of local shell tangent as shown in Fig. 4.8. The x-axis of the local coordinate system is set parallel to the shell normal vector and the z- axis is constrained to remain in a plane parallel to the y-z coordinate plane. From the direction cosines of each of the primed directions relative to the global axis shown in Fig. 4.11, the primed forces and moments become

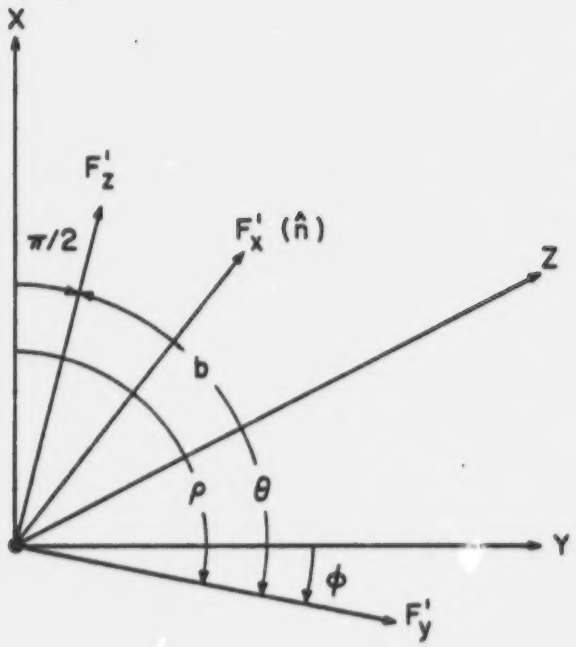

FIG. 4.11 FORCES TRANSFORMED TO LOCAL SHELL SURFACE COORDINATE SYSTEM.

$$F_{x'} = F_x \cos\alpha + F_y \cos\beta + F_z \cos\gamma$$

$$F_{y'} = F_x \cos\rho + F_y \cos\phi + F_z \cos\theta$$

$$F_{z'} = F_y \cos(b + \pi/2) + F_z \cos b$$

$$M_{x'} = M_x \cos\alpha + M_y \cos\beta + M_z \cos\gamma = 0 \qquad (4.27)$$

$$M_{y'} = -M_x \sin\alpha + M_y \cos\alpha \cos b + M_z \cos\alpha \sin b$$

$$M_{z'} = M_z \cos b - M_y \sin b$$

The angles α, β and γ are known direction angles of the shell normal vector. The angle ρ, ϕ, θ, and b are determined from the coordinate system constraints imposed. Since z' is parallel to the y-z plane, the y' coordinate would be in the plane defined by the x-x' axes. The direction angle ρ is given by

$$\rho = \alpha + \pi/2 \qquad (4.28)$$

The remaining direction angles are determined by reference to spherical geometry (Fig. 4.12). Using the Napier's rules for right spherical triangles, the angle 'b' is given as

$$|b| = \sin^{-1}\left[\sqrt{\sin^2\beta - \cos^2\beta \operatorname{ctn}^2\alpha}\right]$$

and ϕ, θ are defined by

$$\cos\phi = \cos\alpha \cos b \qquad (4.29)$$

and $\cos\theta = \cos\alpha \sin b$

By preserving the equilibrium of force and moment, the inner and outer surface nodal forces are

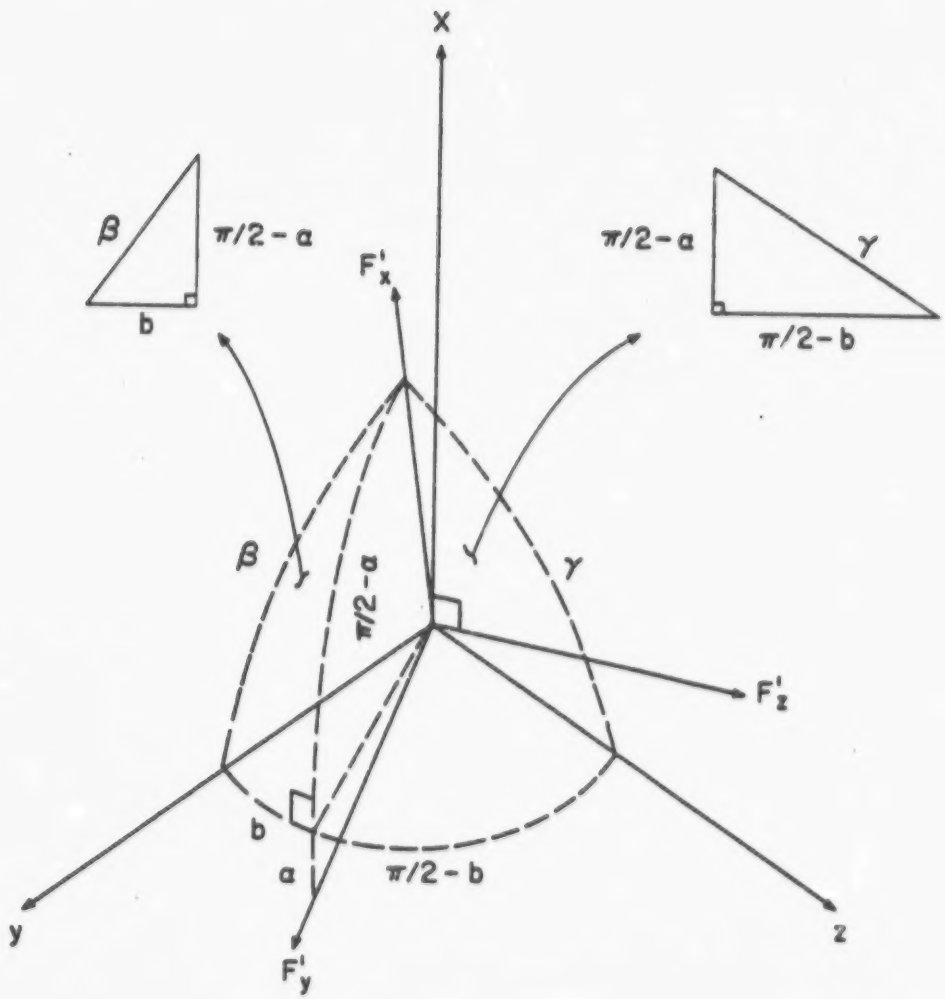

FIG. 4.12 USE OF SPHERICAL TRIGONOMETRY TO SOLVE FOR AZIMUTH ANGLE b.

$$F_{x'0} = \frac{F_{x'}}{2} \qquad F_{x'i} = \frac{F_{x'}}{2}$$

$$F_{y'0} = \frac{F_{y'}}{2} + \frac{M_{z'}}{t} \qquad F_{y'i} = F_{y'} - F_{y'0} \tag{4.30}$$

$$F_{z'0} = \frac{F_{z'}}{2} - \frac{M_{y'}}{t} \qquad F_{z'i} = F_{z'} - F_{z'0}$$

Finally the equilibrium forces are transferred back to global system so that they would be used as input to the 3-D solid element rezone model. The results of this last transformation are as follows:

$$F_{xo} = F_{x'o} \cos \alpha - F_{y'o} \sin \alpha$$

$$F_{xi} = F_{x'i} \cos \alpha - F_{y'o} \sin \alpha$$

$$F_{yo} = F_{x'o} \cos \beta + F_{y'o} \cos \alpha \cos b - F_{z'o} \sin b$$

$$F_{yi} = F_{x'i} \cos \beta + F_{y'i} \cos \alpha \cos b - F_{z'i} \sin b \tag{4.31}$$

$$F_{zo} = F_{x'o} \cos \gamma + F_{y'o} \cos \alpha \sin b + F_{z'o} \cos b$$

$$F_{zi} = F_{x'i} \cos \gamma + F_{y'i} \cos \alpha \sin b + F_{z'i} \cos b$$

Thus substituting Eqn. 4.27 into Eqn. 4.30 and then Eqn. 4.30 into Eqn. 4.31 leads to the forces which are applied to the inner and outer surface nodes of the transition boundary of the 3-D rezone model.

Boundary conditions

The element stiffness matrices are assembled to obtain the global stiffness of the rezoned model. Interior displacement vector for the rezoned model are determined for imposed boundary displacements/forces obtained from the 2-dimensional solution.

Considering the rezone model with n degrees of freedoms, the force displacement relations are written as

$$\begin{bmatrix} K_{11} & K_{12} & \cdot & K_{1m} & K_{1(m+1)} & \cdot & K_{1n} \\ K_{21} & K_{22} & \cdot & K_{2m} & K_{2(m+1)} & \cdot & K_{2n} \\ \cdot & \cdot & \cdot & & \cdot & \cdot & \cdot \\ K_{m1} & K_{m2} & \cdot & K_{mm} & K_{m(m+1)} & \cdot & K_{mn} \\ K_{(m+1)1} & K_{(m+1)2} & & K_{(m+1)m} & K_{(m+1)(m+1)} & \cdot & K_{(m+1)n} \\ \cdot & \cdot & \cdot & \cdot & \cdot & \cdot & \cdot \\ K_{n1} & K_{n2} & \cdot & K_{nm} & K_{n(m+1)} & \cdot & K_{nn} \end{bmatrix} \begin{Bmatrix} \delta_1 \\ \delta_2 \\ \cdot \\ \delta_m \\ \delta_{(m+1)} \\ \cdot \\ \delta_n \end{Bmatrix} = \begin{Bmatrix} F_1 \\ F_2 \\ \cdot \\ F_m \\ F_{(m+1)} \\ \cdot \\ F_n \end{Bmatrix} \quad (4.32)$$

Imposing m boundary displacements, $\delta_1 = \beta_1$, $\delta_2 = \beta_2 \ldots\ldots \delta_m = \beta_m$ at the transition nodes, the displacements are obtained after modifying the stiffness, [K], and force, {F} matrices, as

$$\begin{bmatrix} 1 & 0 & \cdot & 0 & 0 & \cdot & 0 \\ 0 & 1 & \cdot & 0 & 0 & \cdot & 0 \\ \cdot & \cdot & \cdot & \cdot & \cdot & \cdot & \cdot \\ 0 & 0 & \cdot & 1 & 0 & \cdot & 0 \\ 0 & 0 & \cdot & 0 & K_{(m+1)(m+1)} & \cdot & K_{(m+1)n} \\ \cdot & \cdot & \cdot & \cdot & \cdot & \cdot & \cdot \\ 0 & 0 & \cdot & 0 & K_{n(m+1)} & \cdot & K_{nn} \end{bmatrix} \begin{Bmatrix} \delta_1 \\ \delta_2 \\ \cdot \\ \delta_m \\ \delta_{(m+1)} \\ \cdot \\ \delta_n \end{Bmatrix} = \begin{Bmatrix} \beta_1 \\ \beta_2 \\ \cdot \\ \beta_m \\ F'_{(m+1)} \\ \cdot \\ F'_n \end{Bmatrix} \quad (4.33)$$

where

$$F'_{(m+1)} = F_{(m+1)} - K_{(m+1)1}\beta_1 - K_{(m+1)2}\beta_2 \cdots - K_{(m+1)m}\beta_m$$

$$F'_n = F_n - K_{n1}\beta_1 - K_{n2}\beta_2 \cdots - K_{nm}\beta_m \quad (4.34)$$

The unknown displacements $\delta_{m+1}, \ldots, \delta_n$ are obtained by solving the equation

$$\begin{bmatrix} K_{(m+1)(m+1)} & \cdot & K_{(m+1)n} \\ \cdot & \cdot & \cdot \\ K_{n(m+1)} & \cdot & K_{nn} \end{bmatrix} \begin{Bmatrix} \delta_{(m+1)} \\ \cdot \\ \delta_n \end{Bmatrix} = \begin{Bmatrix} F'_{m+1} \\ \cdot \\ F'_n \end{Bmatrix} \quad (4.35)$$

Then the forces are obtained from Eqn. (4.32).

4.4 Results and Discussions

4.4.1 General

A computer program based on the formulation presented in sections 4.2 and 4.3 is used for the 3-dimensional analysis of i) the entire joint and ii) rezoned section. The weld dimensions used for the modelling are shown in Fig. 4.13. The entire joint is first analysed for axial and in-plane bending loads. Finite element discretization of the model is shown in Fig. 4.14. The total number of elements, nodes, and the degrees-of-freedom in the discretised model with plug are 516, 1102, and 3306 respectively. For the analysis of rezoned sections, the saddle point rezoned model is analysed for axial compressive load in brace and the results are compared with those of the entire 3-D model analyses. The total number of elements, nodes, and the degrees-of-freedom for the rezoned analysis are 192, 416, and 1248 respectively. The discretization of the rezoned model is shown in Fig. 4.15. The number of degrees-of-freedom in the rezoned model analysis is much less when compared to that for the entire joint.

The total number of degrees of freedom in the analysis exceeds 3000 and semiband width also is above 200. To obtain the solution for such a system in one run in the VAX system, the problem is solved in stages by i) storing the stiffness matrix on a disk, ii) decomposing the stiffness matrix in blocks of 500 equations or 1000 equations and iii) finally back substituting to arrive at the displacment vector in stages.

The stresses can be accurately calculated at the Gauss integration points than at the nodal points. Since the main interest is to obtain

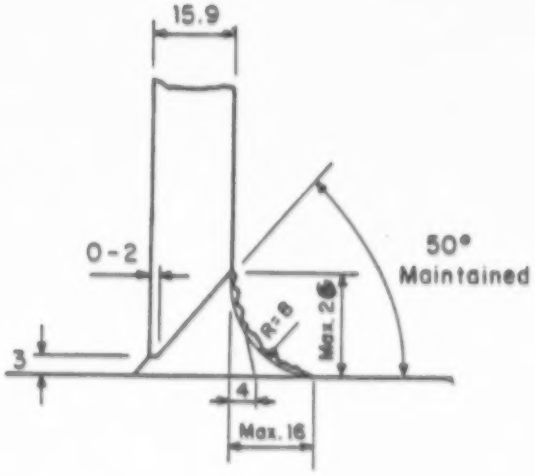

(a) Details of weld

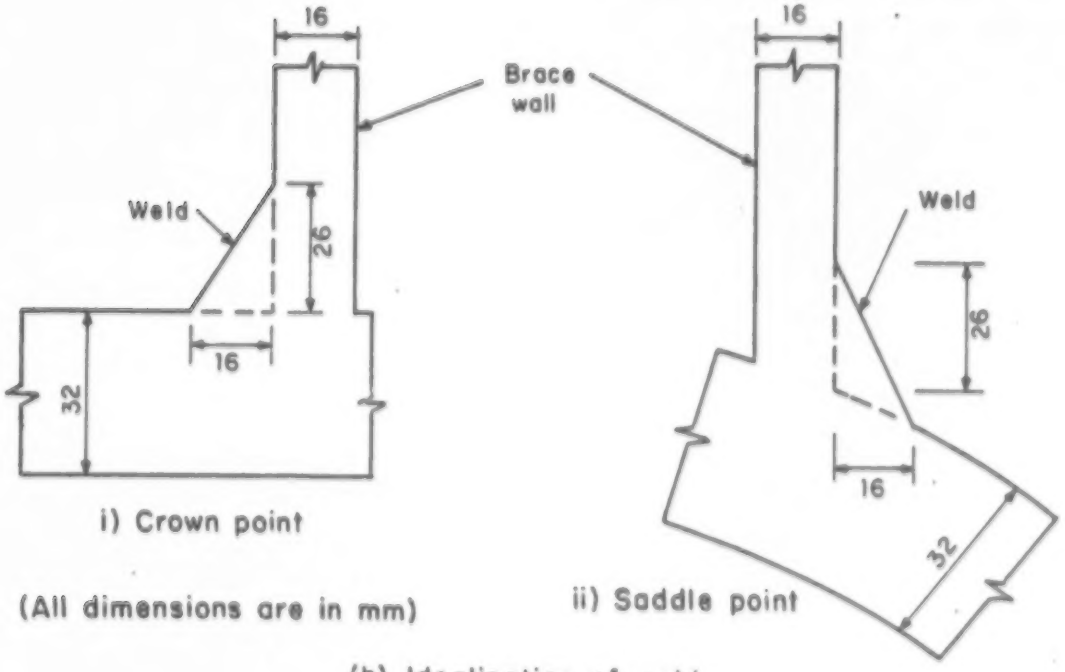

(All dimensions are in mm)

(b) Idealisation of weld

FIG. 4.13 MODELLING OF WELD AT CHORD/BRACE INTERSECTION.

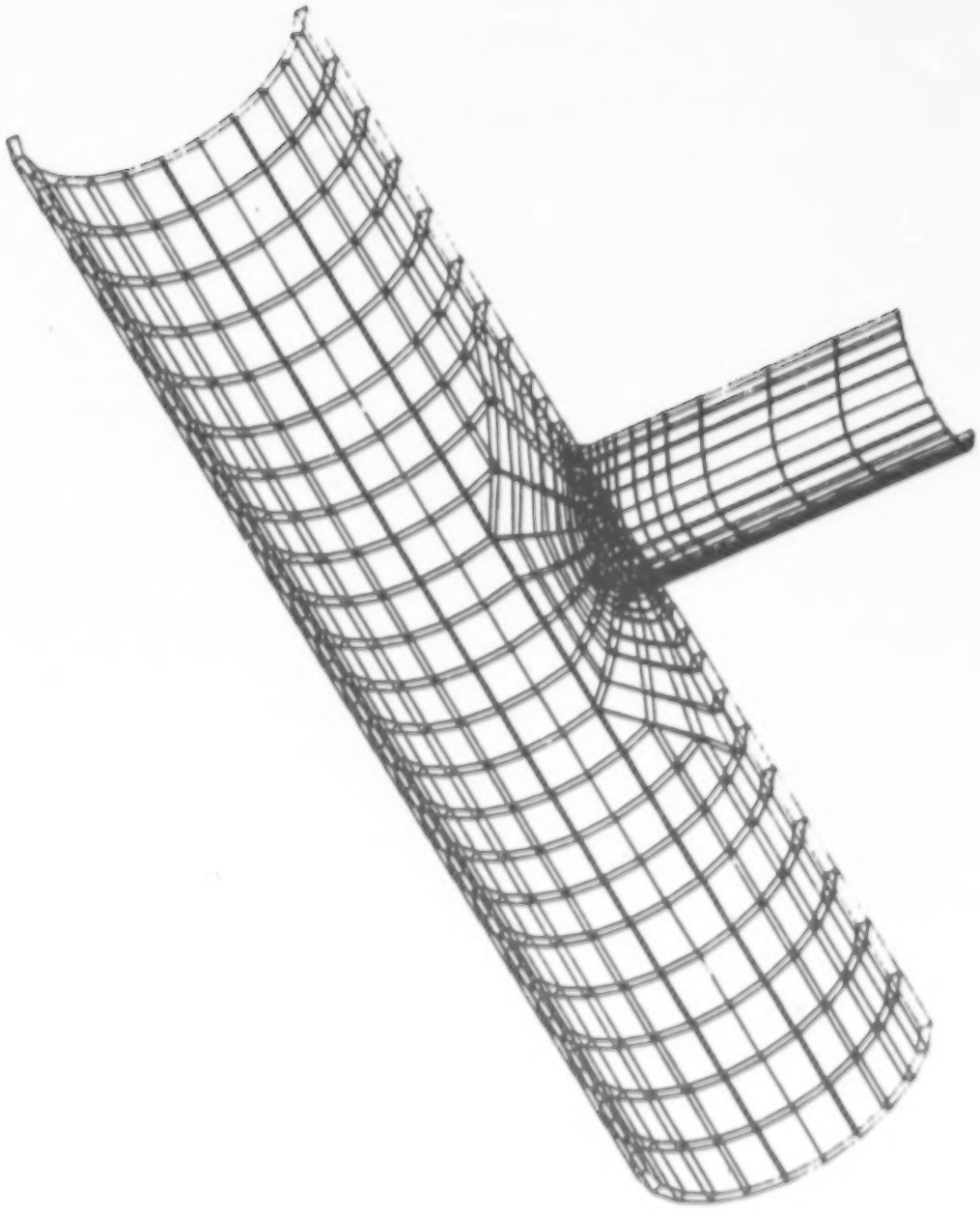

FIG. 4.14a 3-DIMENSIONAL FINITE ELEMENT MESH FOR THE JOINT WITH PLUG

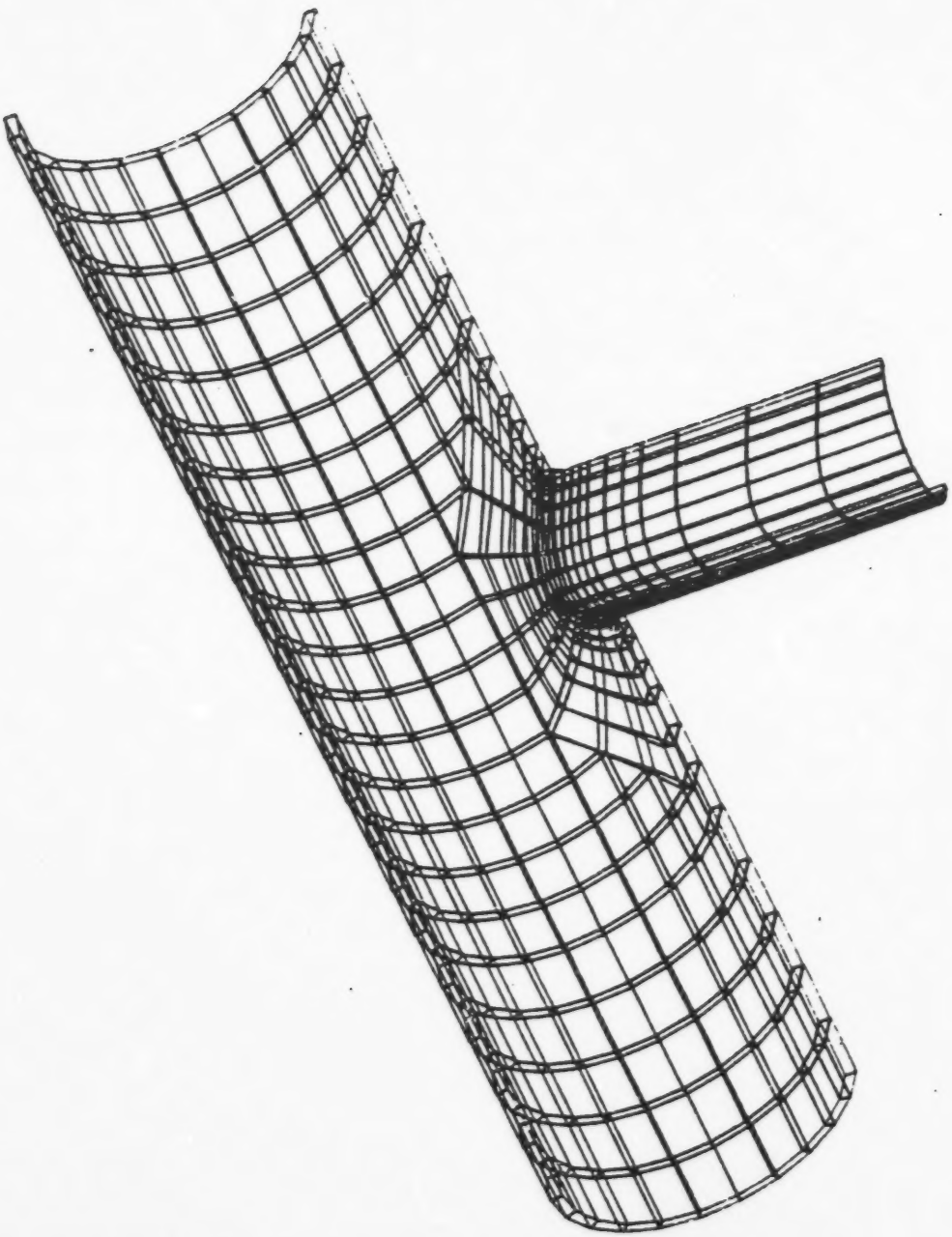

FIG. 4.14 b 3-DIMENSIONAL FINITE ELEMENT MESH FOR THE JOINT WITHOUT PLUG

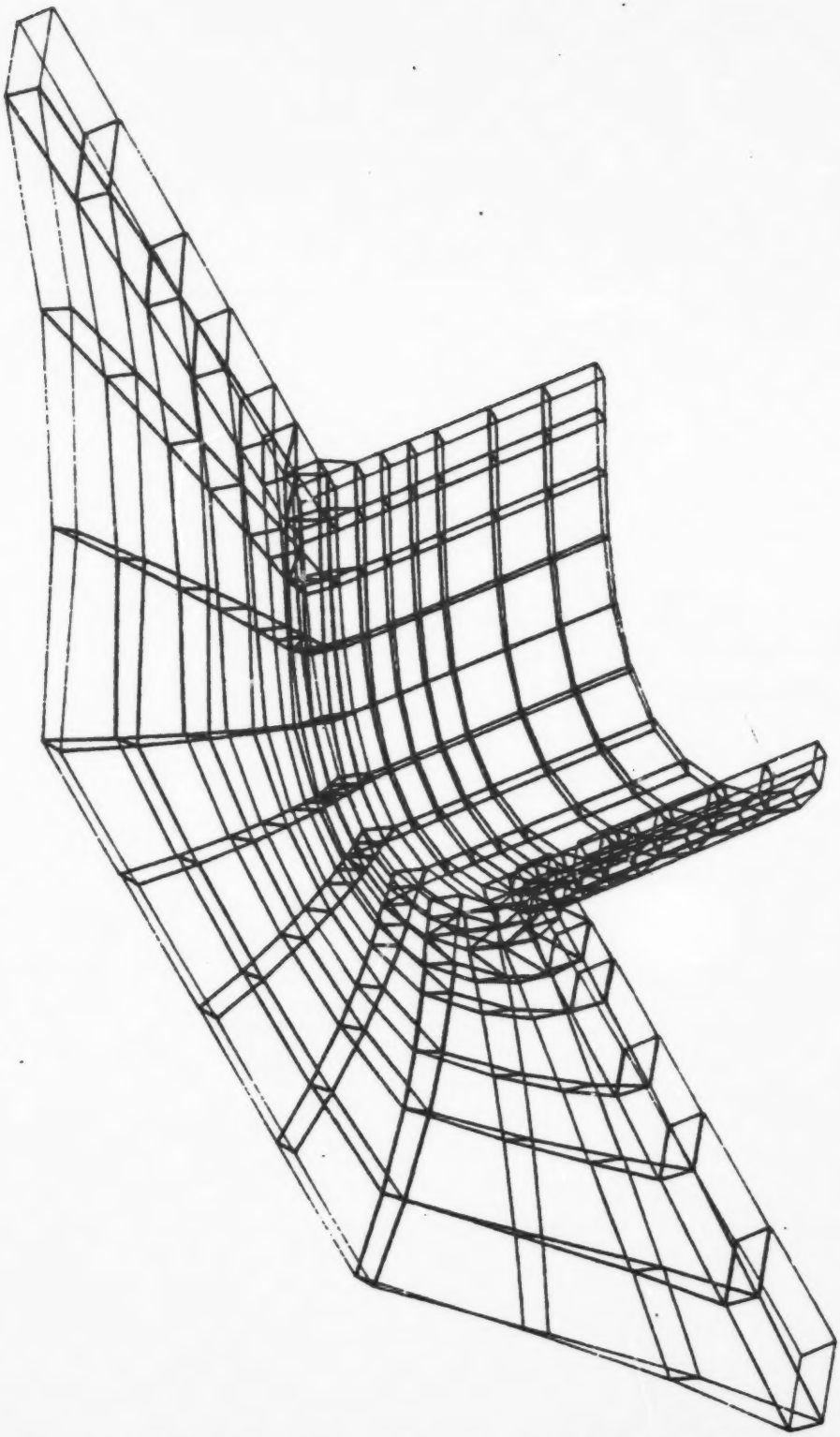

FIG. 4.15 3-DIMENSIONAL FINITE ELEMENT MESH FOR REZONED SECTION OF THE JOINT AT SADDLE POINT

the stress distribution at the outer surface of the shell, the stresses are computed at the nodes and averaged between the elements that are connected at the nodes.

4.4.2 Entire joint analysis

Axial load

The variation of maximum surface stresses at saddle point due to axial load is shown in Fig. 4.16a. The results from two dimensional analysis extend through the weld toe positions up to the intersection of the chord and brace midsurfaces. For the chord side both two and three dimensional analyses give similar variation of stresses as that reported by Parkhouse [38] (Fig. 4.16b). The hot spot stress at the weld toe at saddle point in the chord side obtained from three dimensional analysis without plug is 20 percent higher than that obtained from the two dimensional analysis. But the stress obtained from the 3-dimensional analysis with plug is 10 percent less than the corresponding value from the two dimensional approach. Three dimensional analysis without plug gives a hot spot stress on the brace side which is only 3 percent higher than the two dimensional analysis. The stress variation agrees reasonably well with that reported in ref. [38] (Fig. 4.16c). The stresses near the weld toe from the two dimensional analysis are higher than those obtained from the three dimensional analysis with and without plug. The hot spot stress concentration factors for joint are given in Table 4.1.

The stress variation along the weld surface is shown in Fig. 4.16a. From chord weld toe, the stress decreases up to certain point

TABLE 4.1
Hot Spot Stress Concentration Factors

Methods	Axial				In-plane Bending			
	Chord		Brace		Chord		Brace	
	Crown	Saddle	Crown	Saddle	Crown	Saddle	Crown	Saddle
Present 3-D analysis (full model)	2.2 2.09*	6.448 .57*	2.55 2.34*	7.08 5.41*	1.306 1.06*	—	1.79 1.304*	—
Present Rezoned analysis	—	7.53	—	9.83	—	—	—	—
Experiment [31]	—	5.8	—	7.1	—	—	1.7	—
Experiment [30]	—	7.7	—	—	—	—	—	—

*In the analysis plug stiffness is included.

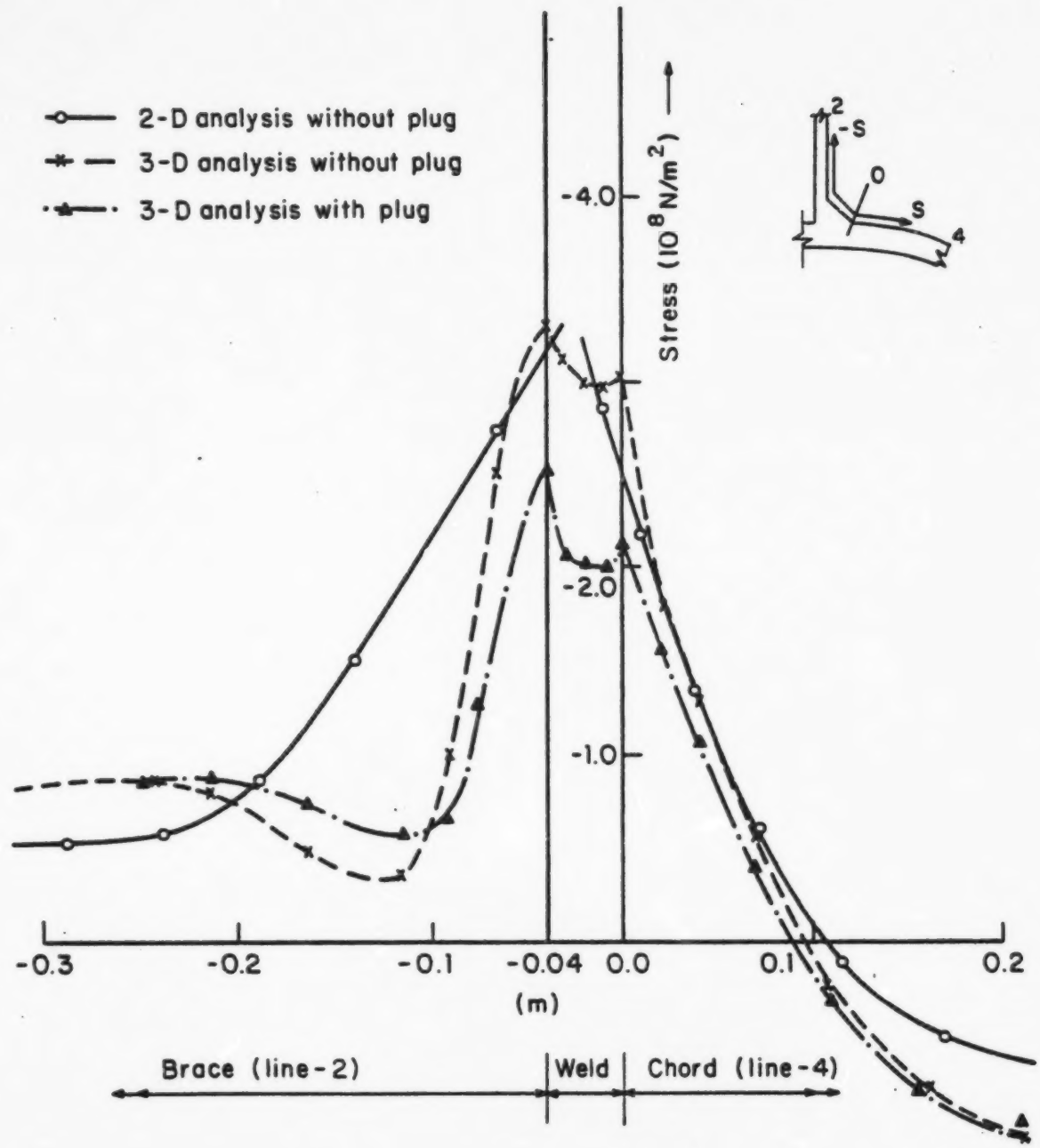

FIG. 4.16 a MAXIMUM SURFACE STRESS VARIATION AT SADDLE POINT DUE TO AXIAL LOAD

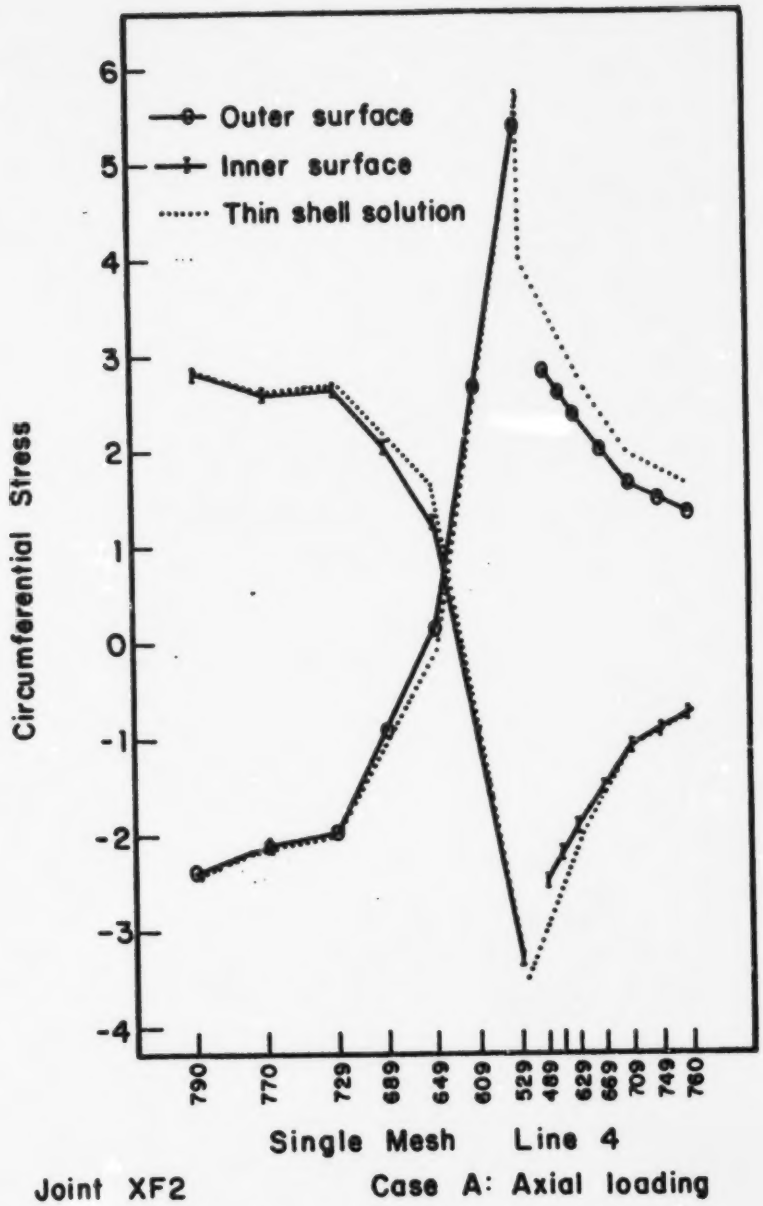

FIG. 4.16 b STRESSES ALONG LINE 4 [REF. 38]

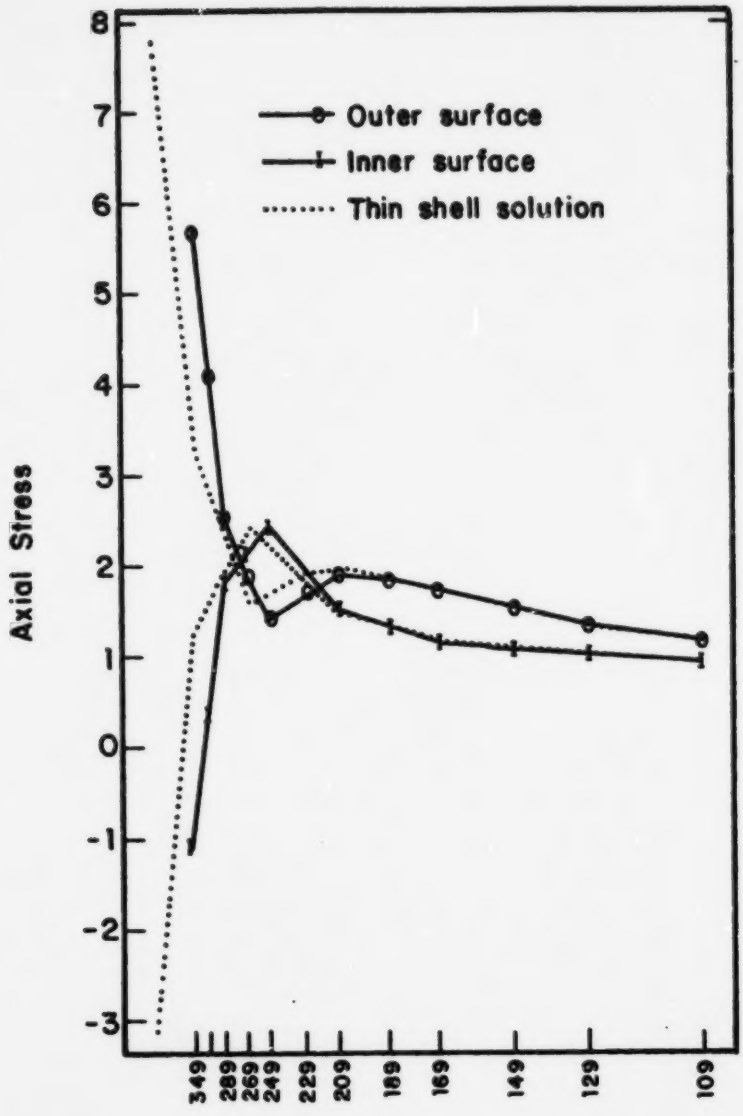

FIG. 4.16 c STRESSES ALONG LINE 2 [REF. 38]

and then starts increasing and reaches a maximum value at the brace weld toe, which compares well with that reported by Morgan [39] (Fig. 4.16d). The variation of strain concentration factors (SNCFs) near the saddle point for axial load, obtained from the three dimensional analysis compares well with the measured values reported by deBack (51) for the tubular joints having the same dimensions as that under study in this report (Figs. 4.16e and 4.16f).

Figure 4.17 shows the stress distribution across the weld reinforcement and brace wall at the saddle point due to axial load. A rapid decrease in stress across the weld leg is observed in contrast to the nearly constant value through the brace wall.

The stress values at the crown point obtained from the two dimensional analysis are lower on the chord side but higher on the brace side when compared to the three dimensional analyses with and without plug (Fig. 4.18). Gradual increase in stress is observed along the weld surface from the chord to brace weld toe. The through thickness variation of stress across the weld and brace (Fig. 4.19) is similar to that observed at the saddle point (Fig. 4.17).

In plane bending:

The hot spot stresses at the weld toe computed from the three dimensional analyses are higher on both the chord and brace sides at the crown point compared to those obtained from the two dimensional analysis (Fig. 4.20). However the stress gradient obtained from the three dimensional analyses on the brace side is steeper than that given by the two dimensional analysis. Stress variations across the weld and brace (Fig. 4.21) are similar to those obtained for the case of axial load (Fig. 4.19).

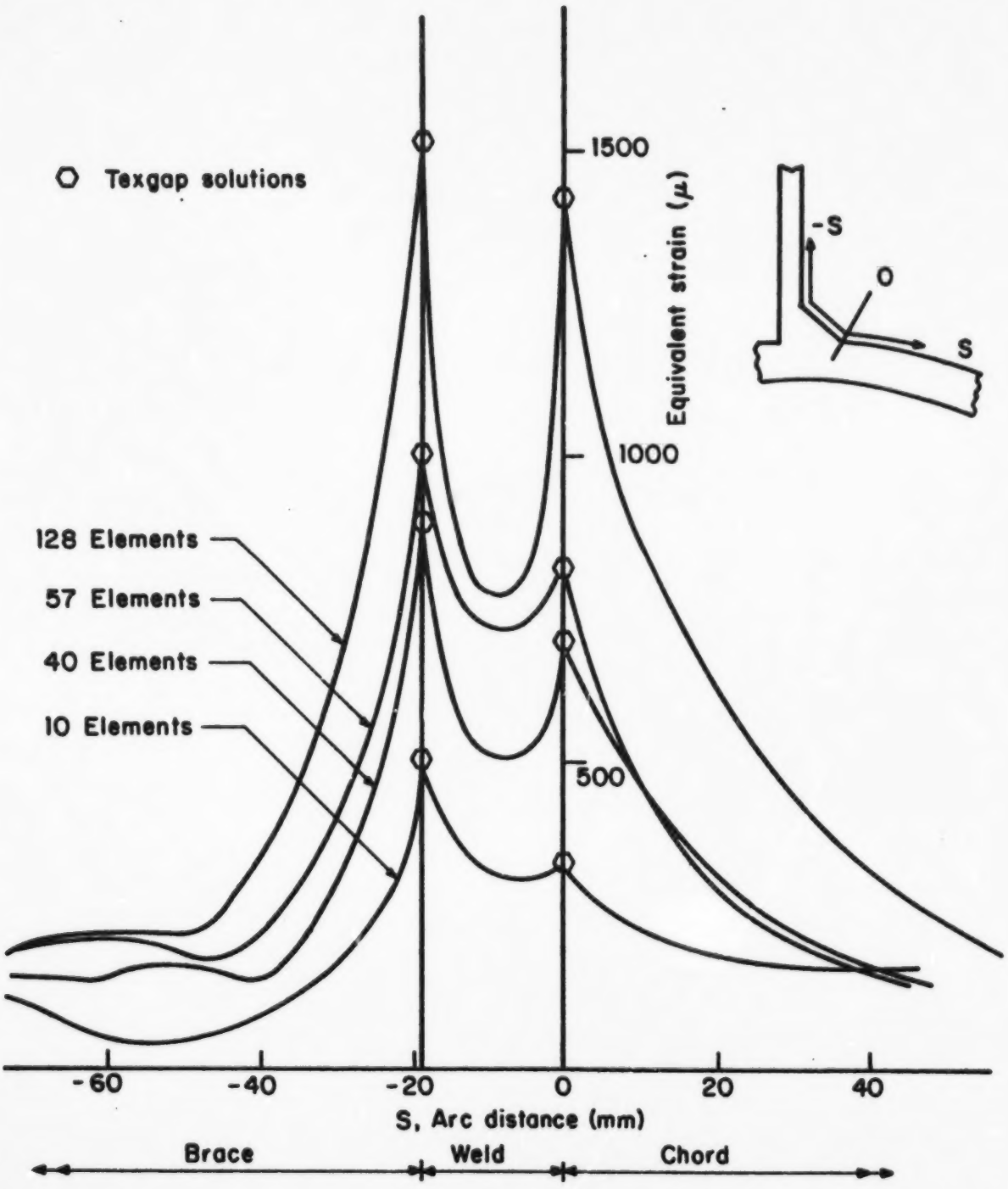

FIG. 4.16 d TRANSVERSE MIDSECTION STRAIN LEVELS FOR THE TEXGAP-3D SOLUTIONS [REF. 39]

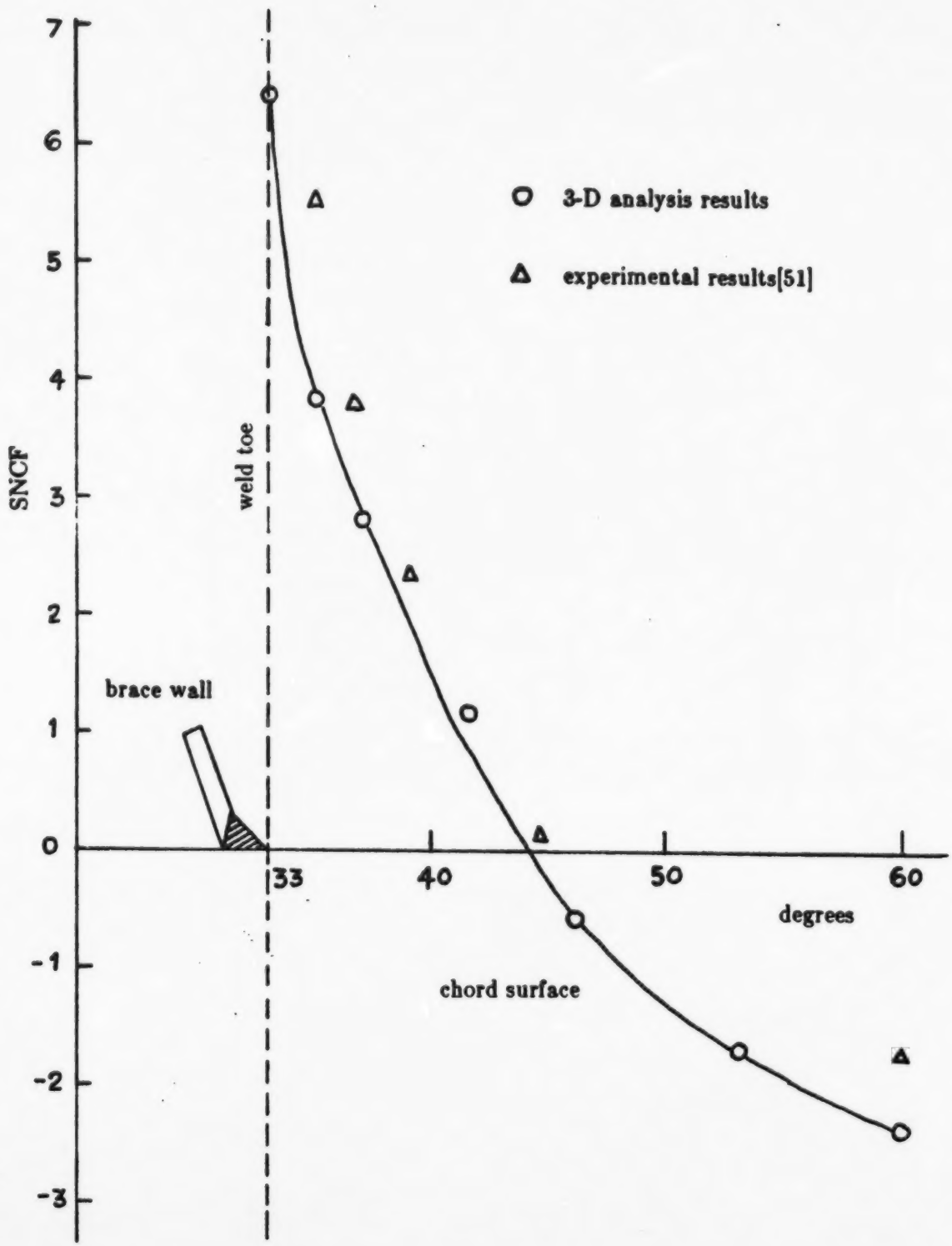

FIG. 4.16eSTRAIN DISTRIBUTION ALONG LINE-4 DUE TO AXIAL LOAD

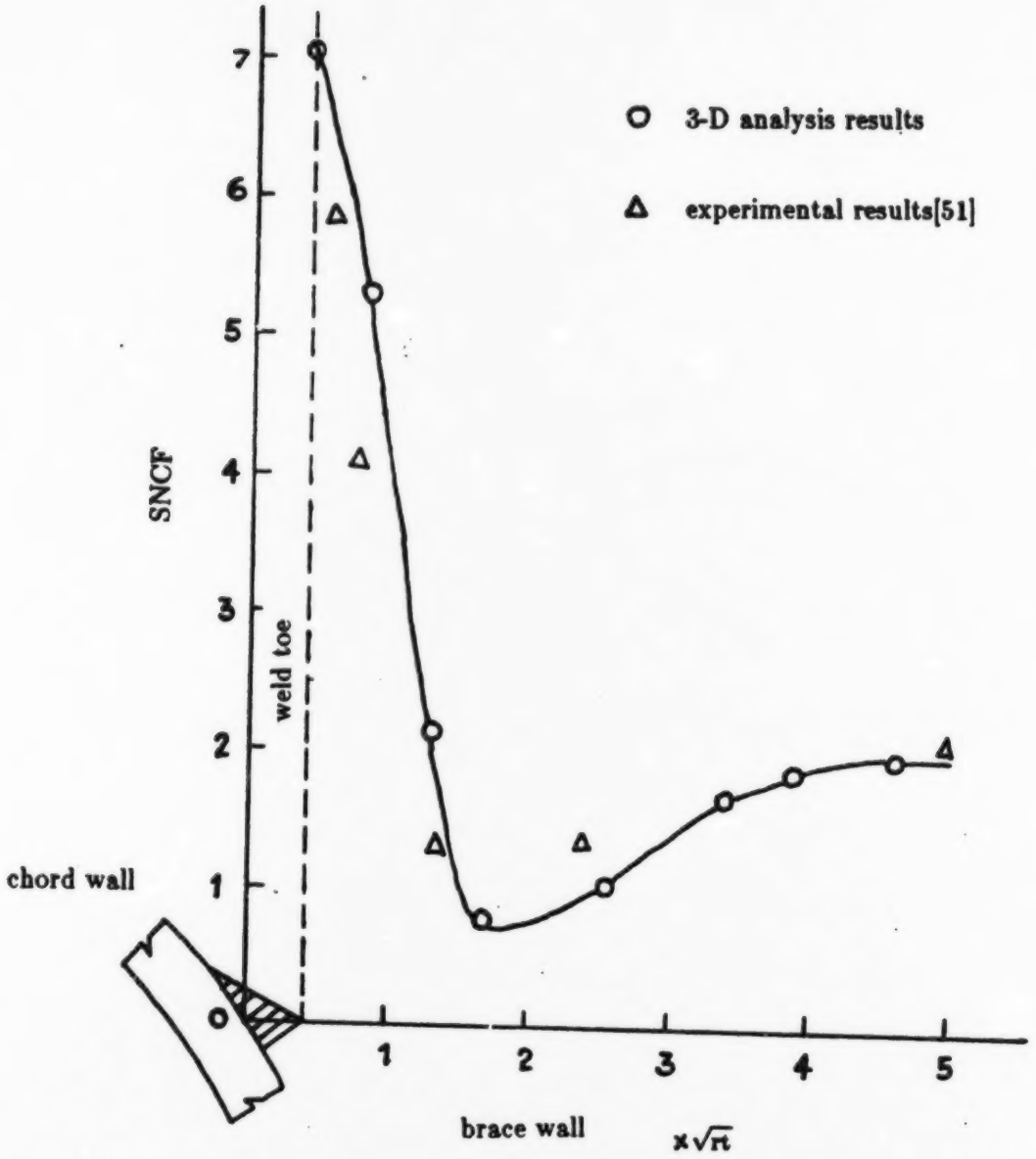

FIG. 4.16fSTRAIN DISTRIBUTION ALONG LINE-2 DUE TO AXIAL LOAD

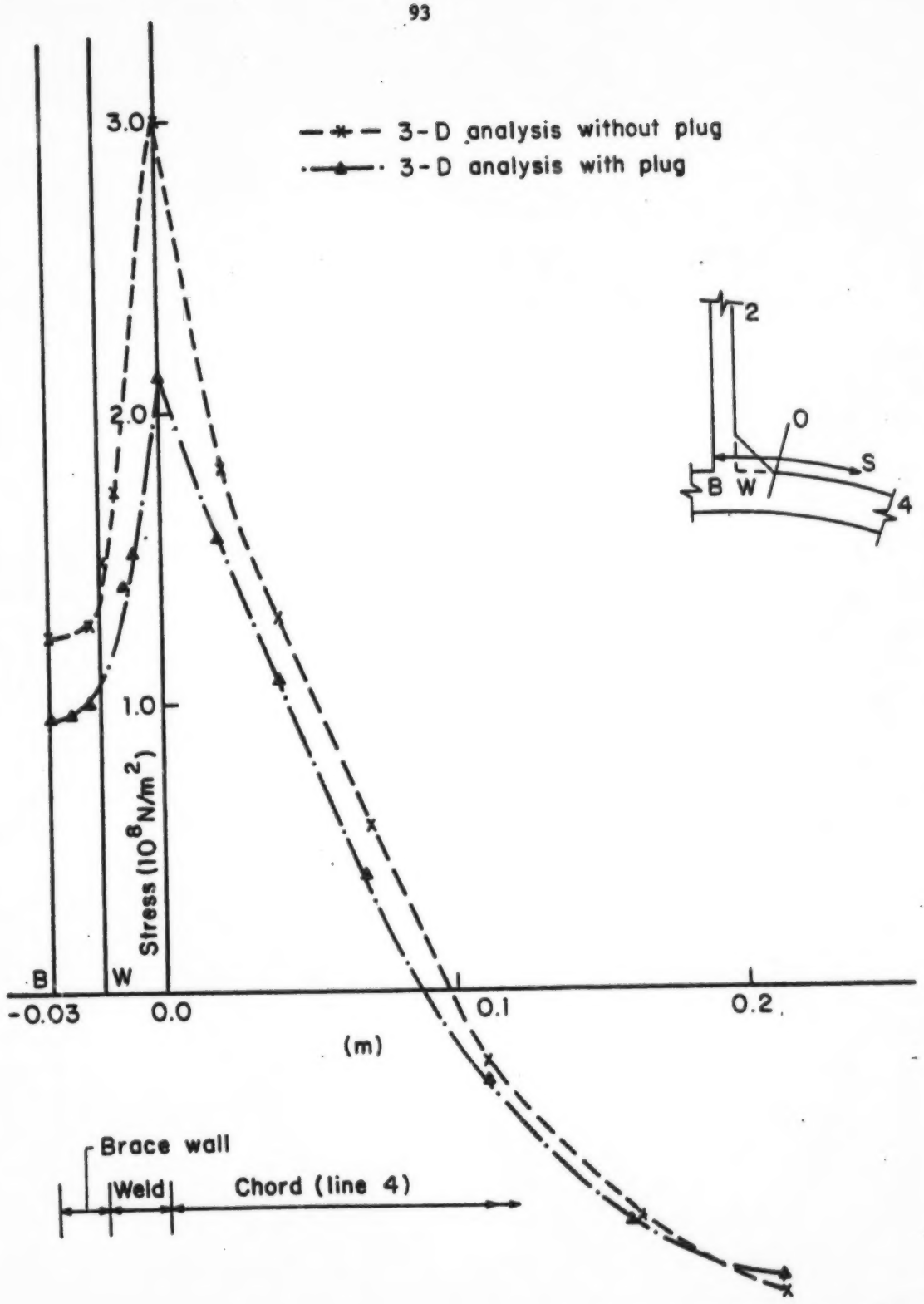

FIG. 4.17 STRESS DISTRIBUTION ACROSS THE WELD AND BRACE WALL AT SADDLE POINT DUE TO AXIAL LOAD

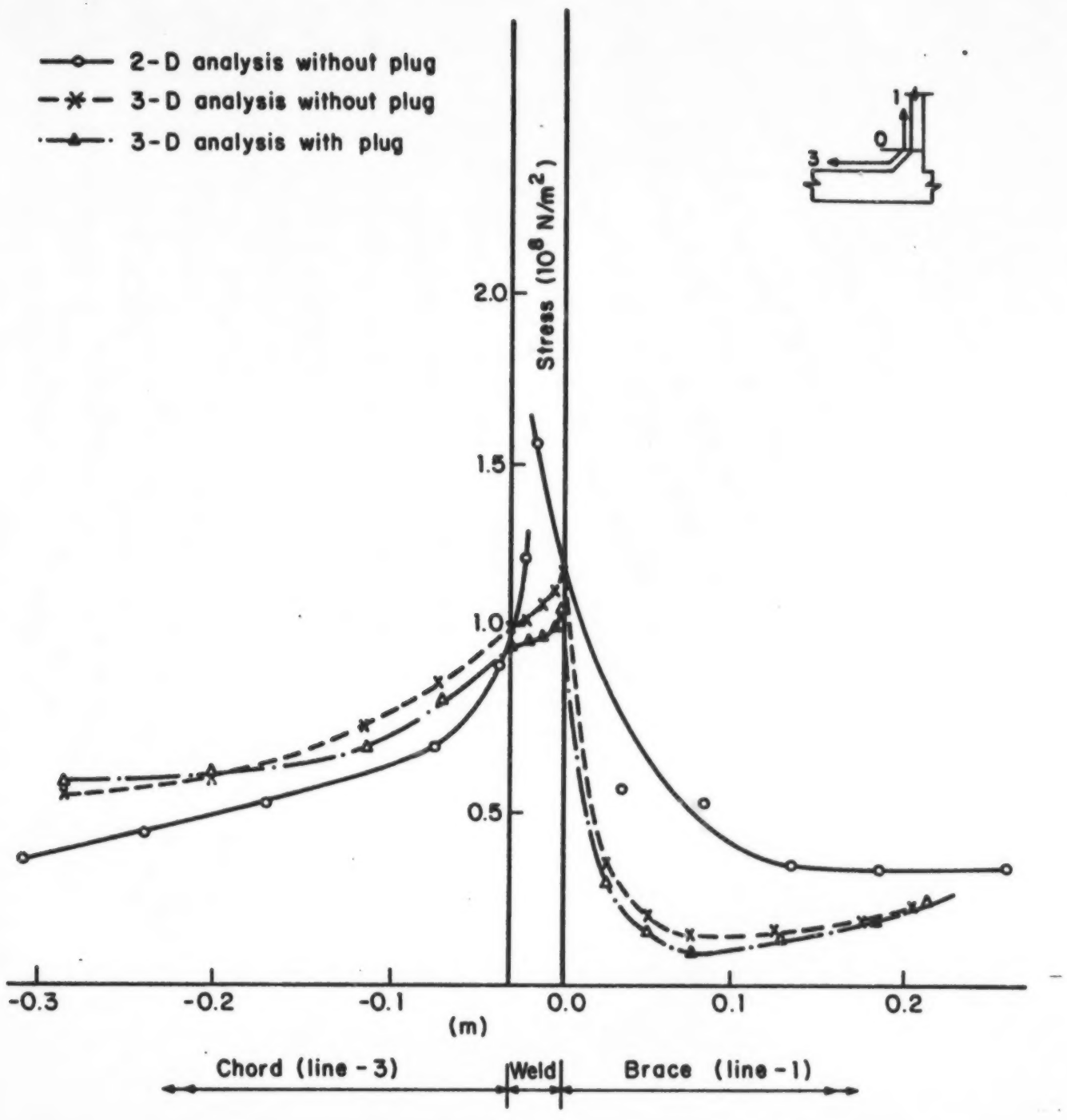

FIG. 4.18 MAXIMUM SURFACE STRESS VARIATION AT CROWN POINT DUE TO AXIAL LOAD

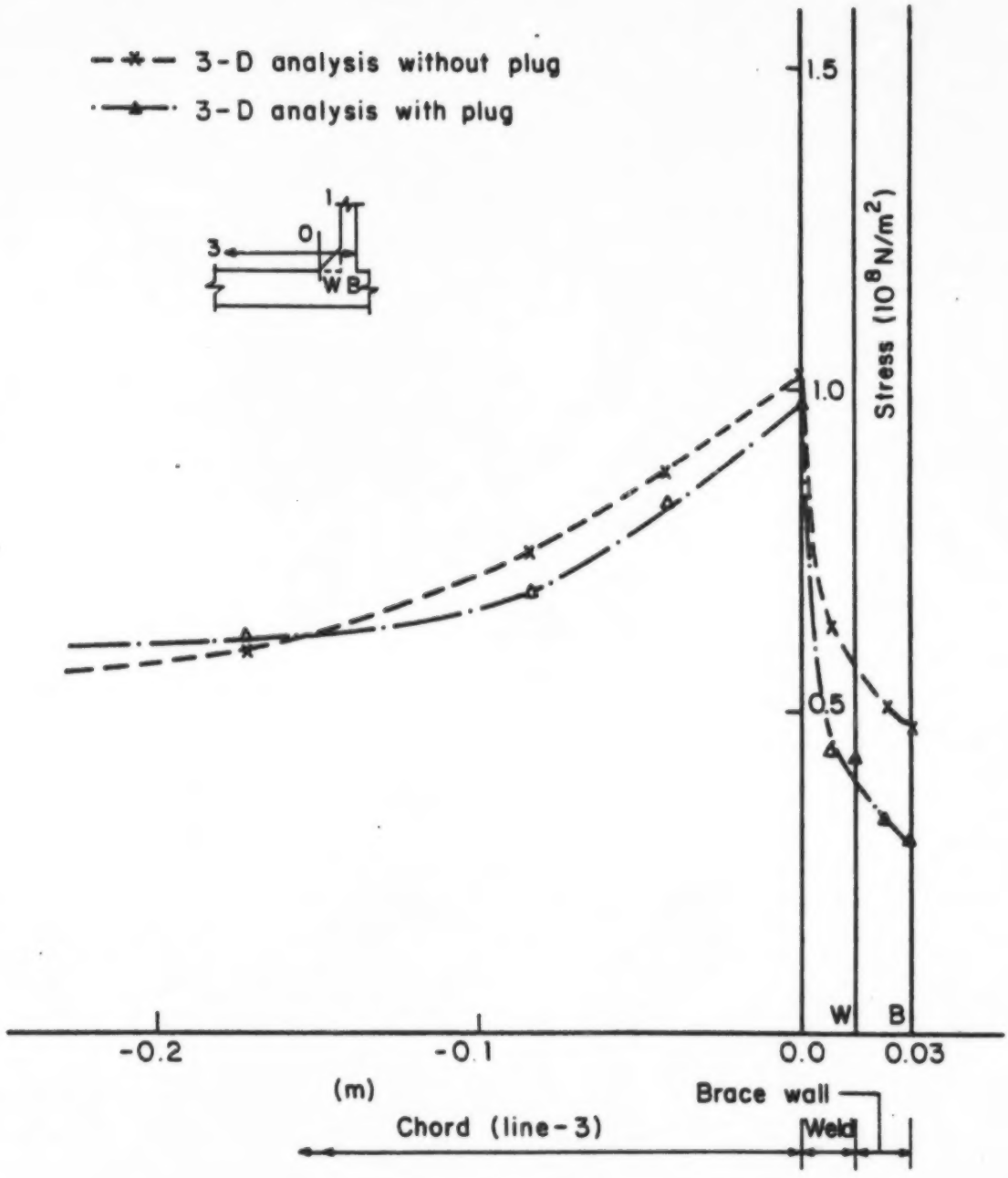

FIG. 4.19 STRESS DISTRIBUTION ACROSS THE WELD AND BRACE WALL AT CROWN POINT DUE TO AXIAL LOAD

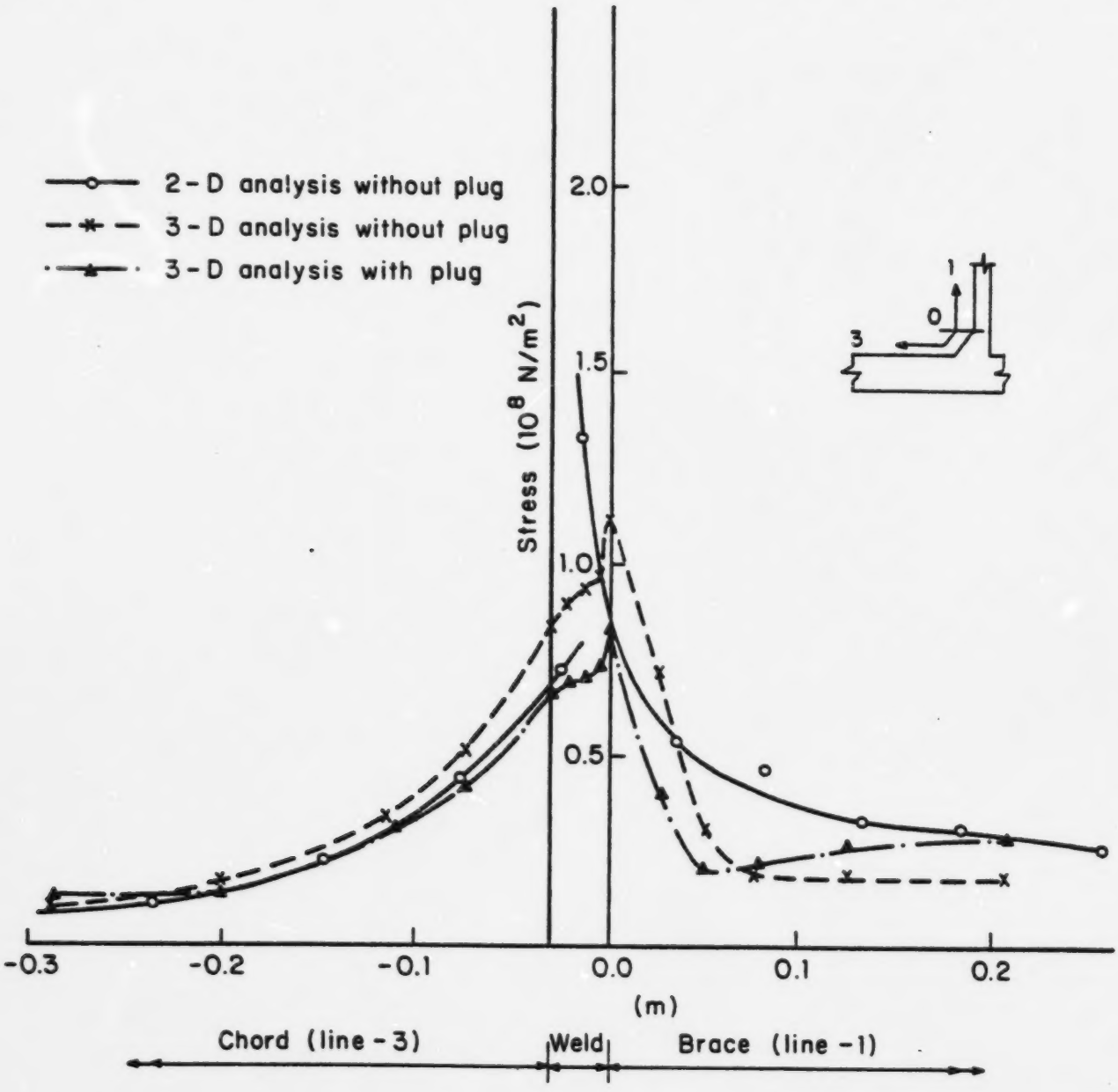

FIG. 4.20 MAXIMUM SURFACE STRESS VARIATION AT CROWN POINT DUE TO IN-PLANE BENDING LOAD

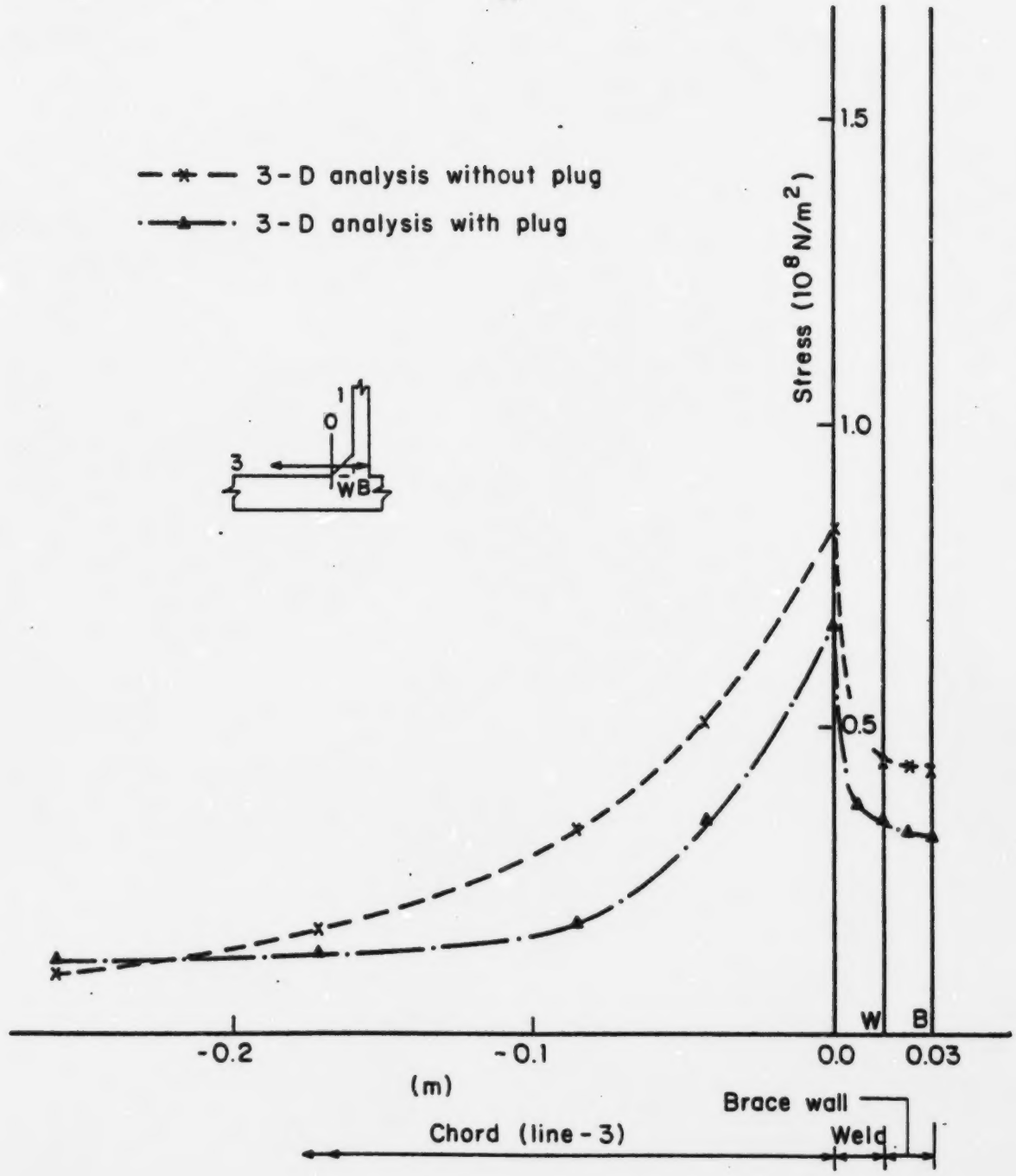

FIG. 4.21 STRESS DISTRIBUTION ACROSS THE WELD AND BRACE WALL AT CROWN POINT DUE TO IN-PLANE BENDING LOAD

4.4.3 Rezoned analysis

The rezoned section of the tubular intersection is shown in Fig. 4.15. The forces and the displacements at the boundary nodes of the rezone are calculated as discussed in section 4.3.2. These forces/displacements are imposed at the boundary of the rezone for the case of axial load for the stress analysis of the rezone. The stress distribution obtained from the rezone analysis are presented in Figs. 4.22 and 4.23.

Fig. 4.22 shows stress variation in the chord along line 4 and the stress variation along brace line 2 is given in Fig. 4.23. From the figures it can be seen that the stress magnitudes considerably differ from three dimensional analysis of the entire joint. Specifically on the brace side the deviation is very much pronounced, indicating the effect of boundary conditions at the plate to solid transition. Since the plate to solid transition boundary effect is affecting the results considerably, the rezone analysis for inplane bending case is not carried out in lieu of the 3-D analysis of the entire joint.

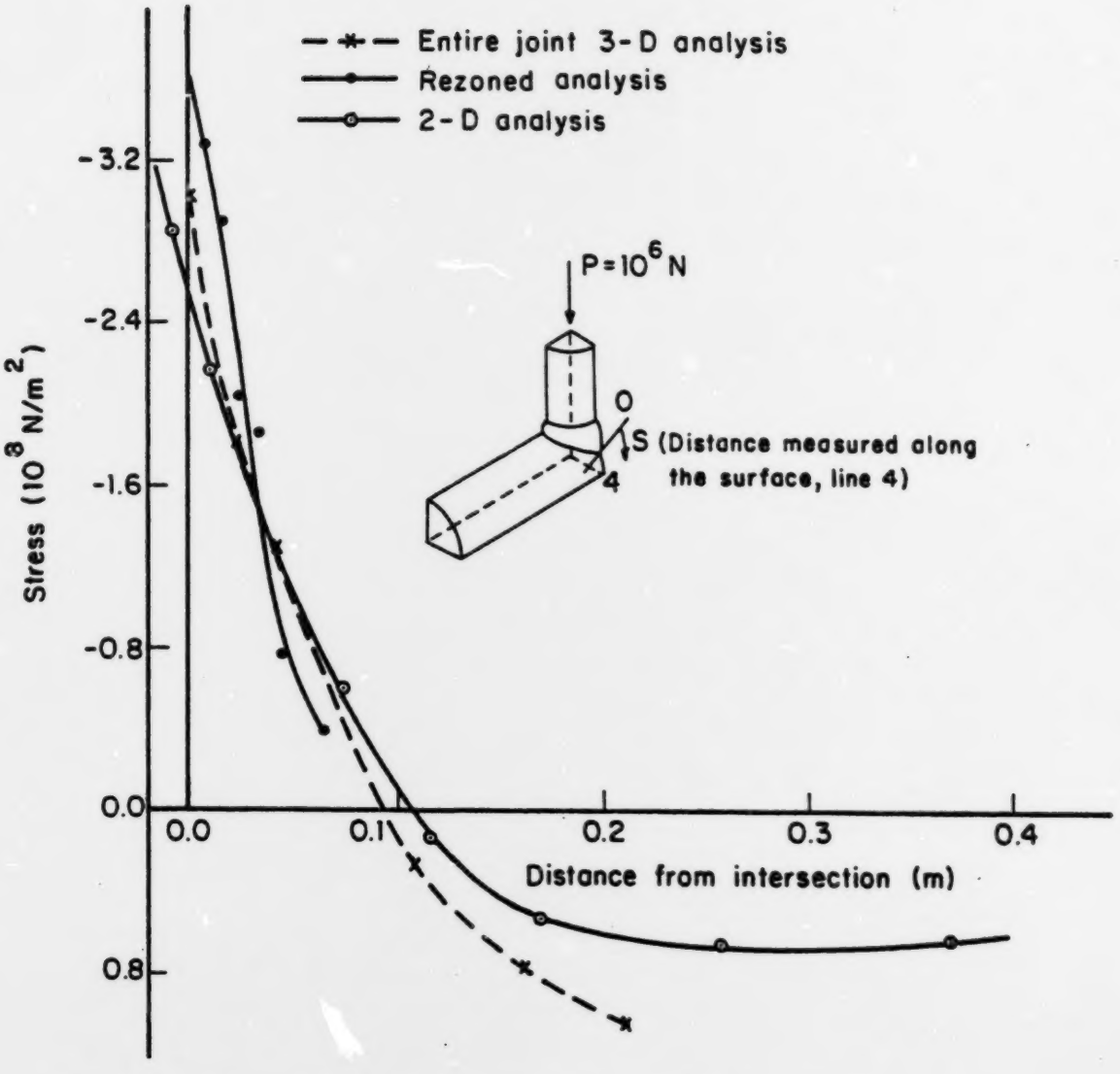

FIG. 4.22 COMPARISON OF ENTIRE JOINT MODEL AND REZONED SECTION ANALYSES RESULTS ALONG LINE - 4

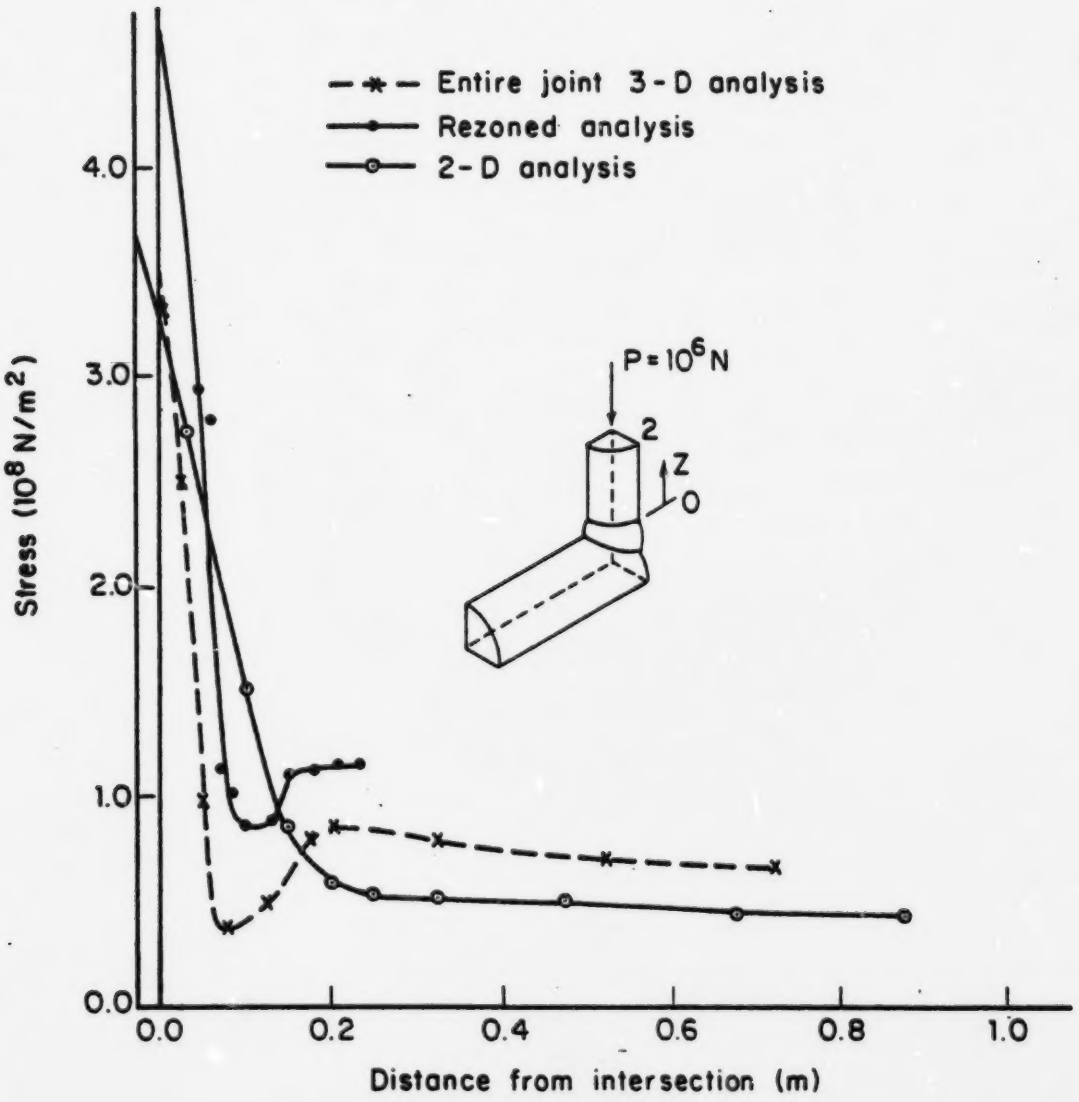

FIG. 4.23 COMPARISON OF ENTIRE JOINT MODEL AND REZONED SECTION ANALYSES RESULTS ALONG LINE-2

CHAPTER V

5. STRESS DISTRIBUTION AROUND SHALLOW CRACK NEAR THE WELD TOE

5.1 Introduction

In the past fifteen years investigation of fracture problems has been one of the most active areas in applied mechanics. In the past the region of crack front is modelled by using a very large number of conventional finite elements, thereby increasing the number of variables to be solved. Moreover, stress singularity is not taken into account. For a linear elastic material, the displacement and stress fields in the vicinity of crack tip vary as $r^{1/2}$ and $r^{-1/2}$ respectively, where r is the radial distance from the crack tip. By introducing singular elements which allow the stress singularity at the crack tip around the crack front, surrounded by the conventional finite element, the requirements of stress singularity can be accounted. In this report, 6 node isoparametric singular element, along with conventional 8 node brick element and 6 node prism element is used to analyse the rezoned model of the tubular T-joint.

5.2 Formulation of Singular Element

The 6-node wedge shaped singular element (Ref. 19) is used for modelling near the crack front which exhibits a square root singularity. The element shown in Fig. 5.1 is obtained by collapsing one face of the 8-node brick element and choosing the appropriate displacement interpolation functions. The brick and wedge elements are considered in the parametric region $0 \leq \xi, \eta, \gamma \leq 1$. The brick nodes

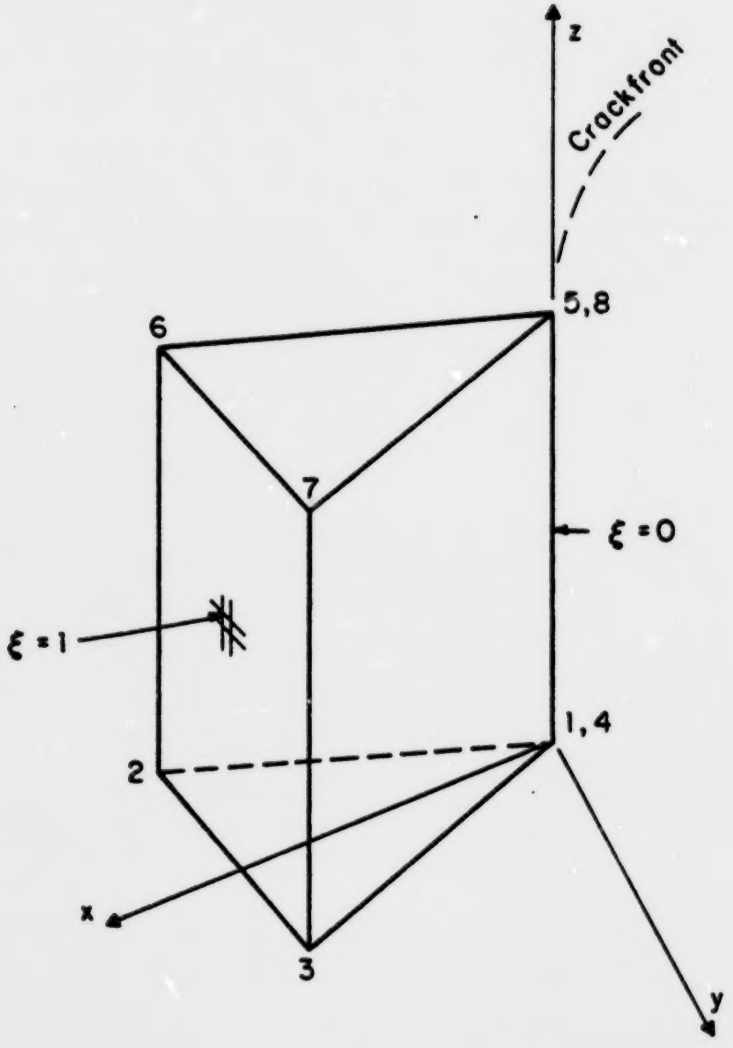

FIG. 5.1 SINGULAR WEDGE ELEMENT

1, 2,...8 take $\xi\eta\gamma$ positions as 000, 100, 110, 010,001, 101, 111, and 011. The mapping function for the physical global cartesian co-ordinate x is given in terms of the nodal coordinates as

$$x = x^1 (1-\xi)(1-\eta)(1-\gamma) + x^2 \xi(1-\eta)(1-\gamma)$$
$$+ x^3 \xi\eta(1-\gamma) + x^4(1-\xi)\eta(1-\gamma)$$
$$+ x^5(1-\xi)(1-\eta)\gamma + x^6 \xi(1-\eta)\gamma$$
$$+ x^7 \xi\eta\gamma + x^8(1-\xi)\eta\gamma \qquad (5.1)$$

where x^1, x^2 ... are x-coordinates of nodes. In the same way relationship can be written for y and z coordinates. The wedge element has only six nodes, but the mapping function is nonetheless valid by making $x^1 = x^4$ and $x^5 = x^8$.

The general form of interpolation function for the displacement component u is given as

$$u = u^1(1-f)(1-\eta)(1-\gamma) + u^2 f(1-\eta)(1-\gamma)$$
$$+ u^3 f\eta(1-\gamma) + u^4(1-f)\eta(1-\gamma)$$
$$+ u^5(1-f)(1-\eta)\gamma + u^6 f(1-\eta)\gamma$$
$$+ u^7 f\eta\gamma + u^8(1-f)\eta\gamma \qquad (5.2)$$

where $f = \xi^{1/2}$ for the displacement components u_x and u_y

$= \xi$ for the component u_z along the crack edge.

Eqn. (5.2) considers eight degrees of freedom, but for the wedge $u^1 = u^4$ and $u^5 = u^8$. From Eqn. (5.2) it can be seen that the local u_x, u_y displacement components depend on square root of ξ, whereas u_z depends on ξ only. This results in an $r^{-1/2}$ distribution for the local strain components ϵ_{xx}, ϵ_{yy} and ϵ_{xy} on a local plane perpendicular to

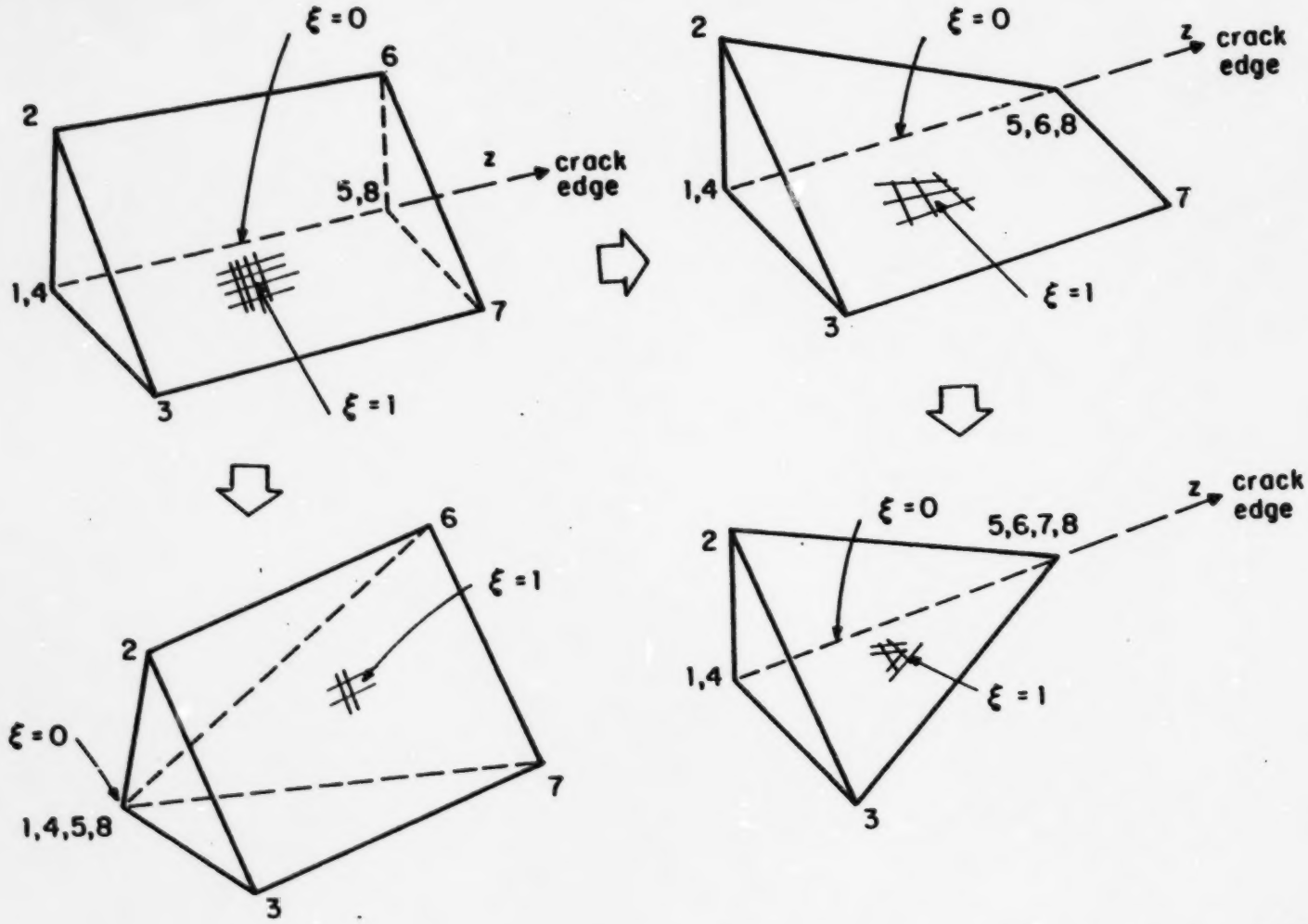

FIG. 5.2 VARIOUS SINGULAR ELEMENTS DEVELOPED TO MODEL CRACK FRONT REGION

the crack edge and non-singular variations of ε_{zz}, ε_{zx} and ε_{zy} throughout the wedge.

For modelling the region at the vicinity of crack, in three dimensional structural model, one may need 5 and 4 noded singular elements. These elements can be obtained by collapsing different sides of the prism as indicated in Fig. 5.2. It is to be observed that on any local xy plane perpendicular to the crack edge, the displacement interpolation functions (Eqn. 5.2) satisfy the singularity constraints.

5.3 Discretization of the Crack Region

The crack front is divided into number of straight line segments. Around each straight crack edge, singular elements are provided. Surrounding these singular elements, conventional brick and wedge elements are used. Fig. 5.3 shows schematic arrangement of element around the crack across any cross section at the weld toe. The three dimensional discretisation of the crack region is shown in Fig. 5.4. The initial surface flaw at the weld toe is modelled as a line of singularity at the surface using singular elements around it. This line of singularity is termed herein as incipient crack.

5.4 Results and Discussion

In order to study the stress redistribution around the shallow crack at the weld toe, two analysis are carried out viz. i) an incipient crack ii) a shallow crack with a depth equal to half the thickness of chord, the length of the crack is approximately 80 mm.

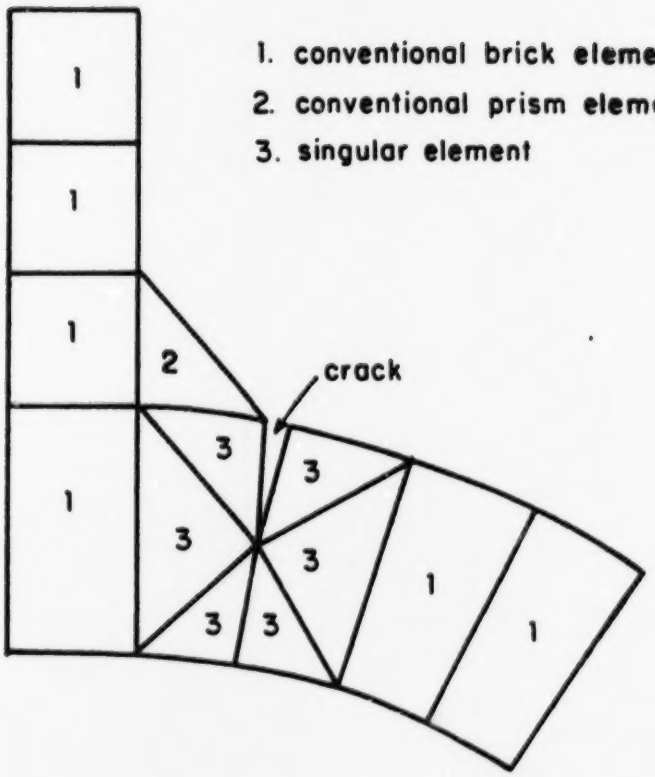

FIG. 5.3 SCHEMATIC ARRANGEMENT OF THREE TYPES OF ELEMENT AROUND CRACK FRONT (CROSS SECTION OF THE SHELL AROUND CRACK REGION)

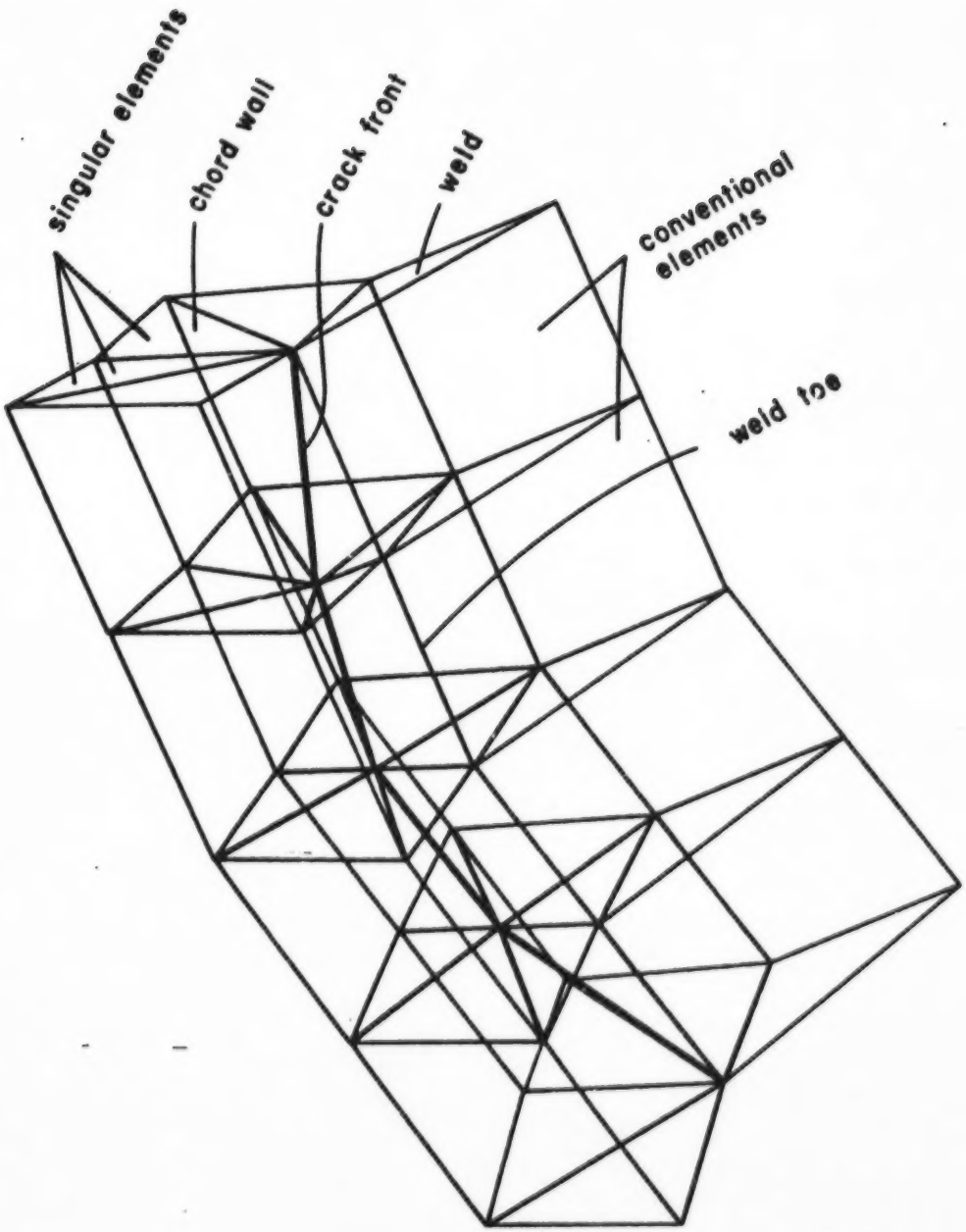

FIG. 5.4 FINITE ELEMENT DISCRETIZATION OF THE REGION IN FRONT OF THE WELD TOE CRACK

Singular elements which were discussed in the previous sections are used to model the crack near front region. Fig. 5.4 shows the discretised model of the crack region. For the analysis the entire region is considered to determine the stress redistribution for an axial load of 10^6N applied at the brace.

Fig. 5.5 shows the stress distribution along line 4 for all the three cases considered viz. i) joint without a crack, ii) joint with an incipient crack and iii) joint with crack depth equal to half the thickness of the chord at weld toe.

From this figure it is seen that in presence of an incipient crack with a very small depth, the stress near the weld toe region is as much as twice that of the joint without a crack and the stress magnitude rapidly decreases away from the crack front, but it is always greater than that of joint without a crack. The stress distribution in presence of a crack with a finite depth (in the present case equals to half the thickness of the chord) almost follow the pattern of the stress distribution of the joint with an incipient crack in the region away from the crack front. Near the crack front the stress decreases considerably, which is evident from the presence of free surface of the crack face.

The stress variation along the brace at saddle point is presented in Fig. 5.6 for the cases considered previously. The stress variation away from the weld toe at the brace is more or less same as that of joint without the crack. At the weld toe of the brace, the stress magnitude is considerably less than that of the joint without crack for the case of incipient crack. The stress magnitude near the weld toe,

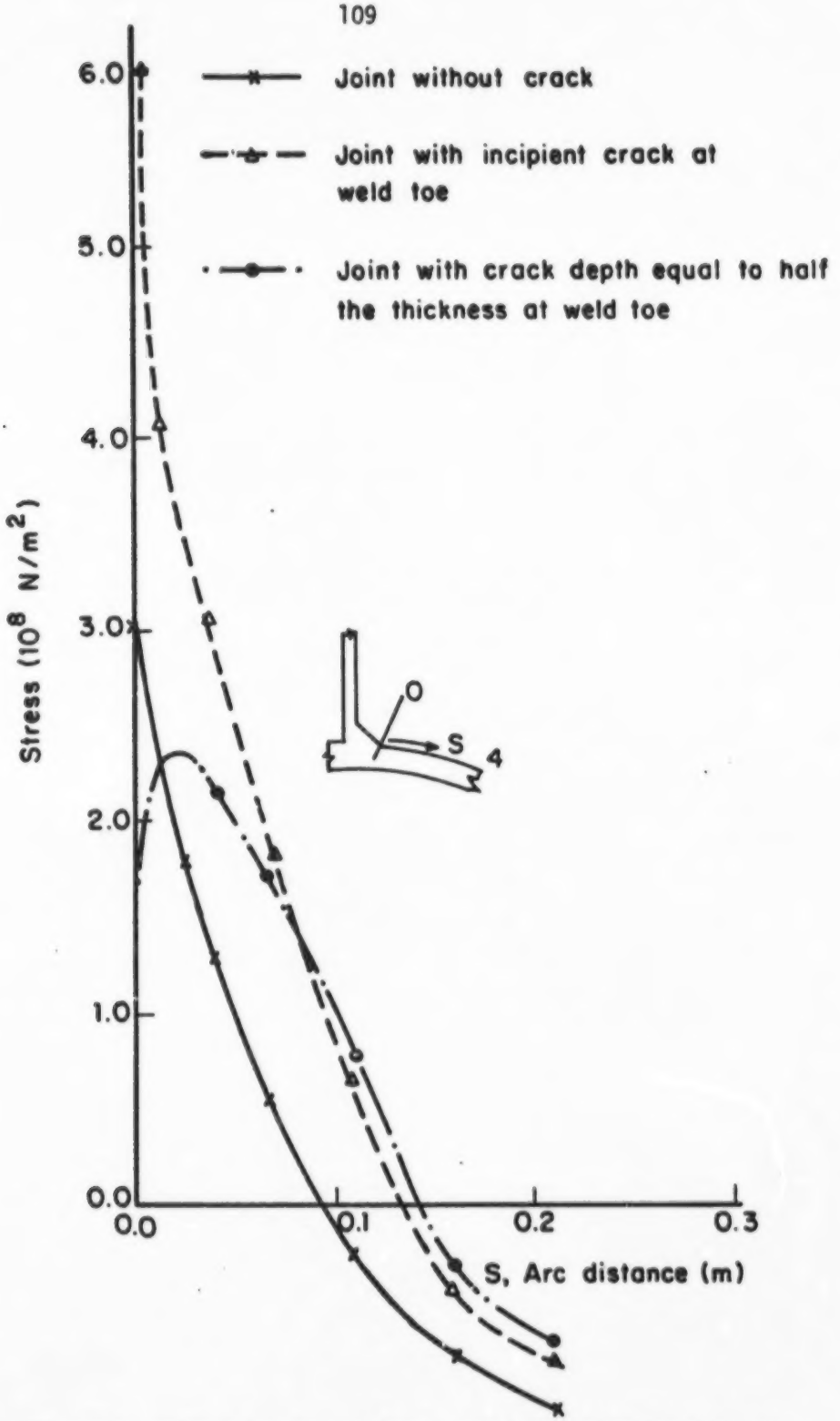

FIG. 5.5a STRESS VARIATION ALONG CHORD SURFACE AT SADDLE POINT IN PRESENCE OF SHALLOW WELD TOE CRACK DUE TO AXIAL LOAD (WITHOUT PLUG)

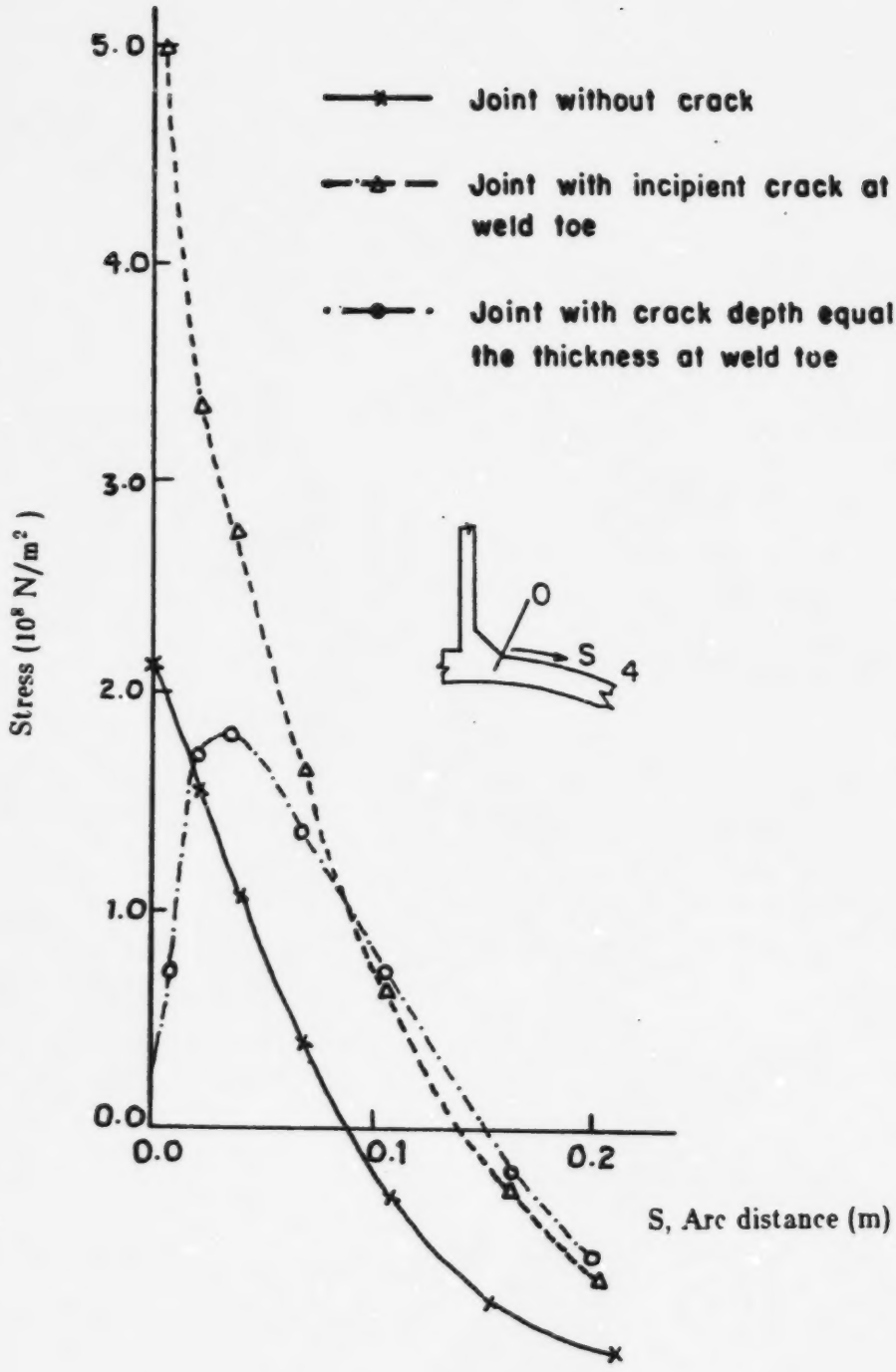

FIG. 5.5b STRESS VARIATION ALONG CHORD SURFACE AT SADDLE POINT IN PRESENCE OF SHALLOW WELD TOE CRACK DUE TO AXIAL LOAD (WITH PLUG)

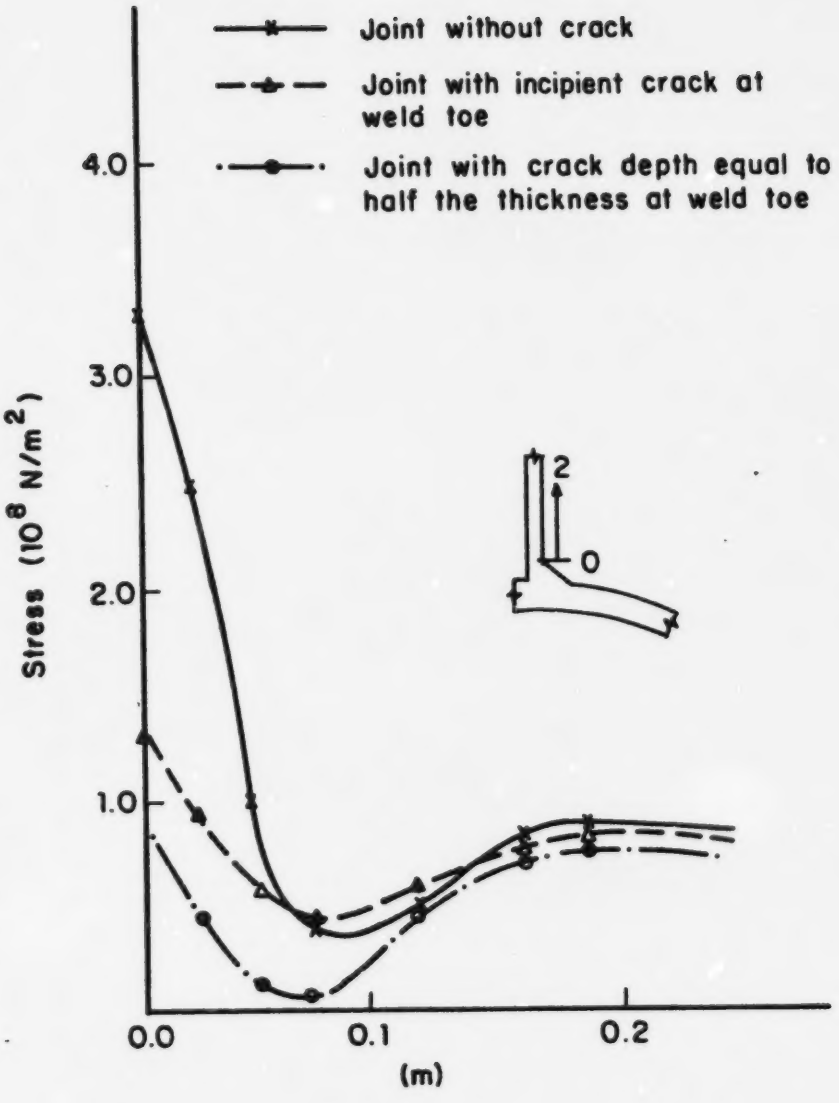

FIG. 5.6a STRESS VARIATION ALONG BRACE SURFACE AT SADDLE POINT IN PRESENCE OF SHALLOW WELD TOE CRACK DUE TO AXIAL LOAD. (WITHOUT PLUG)

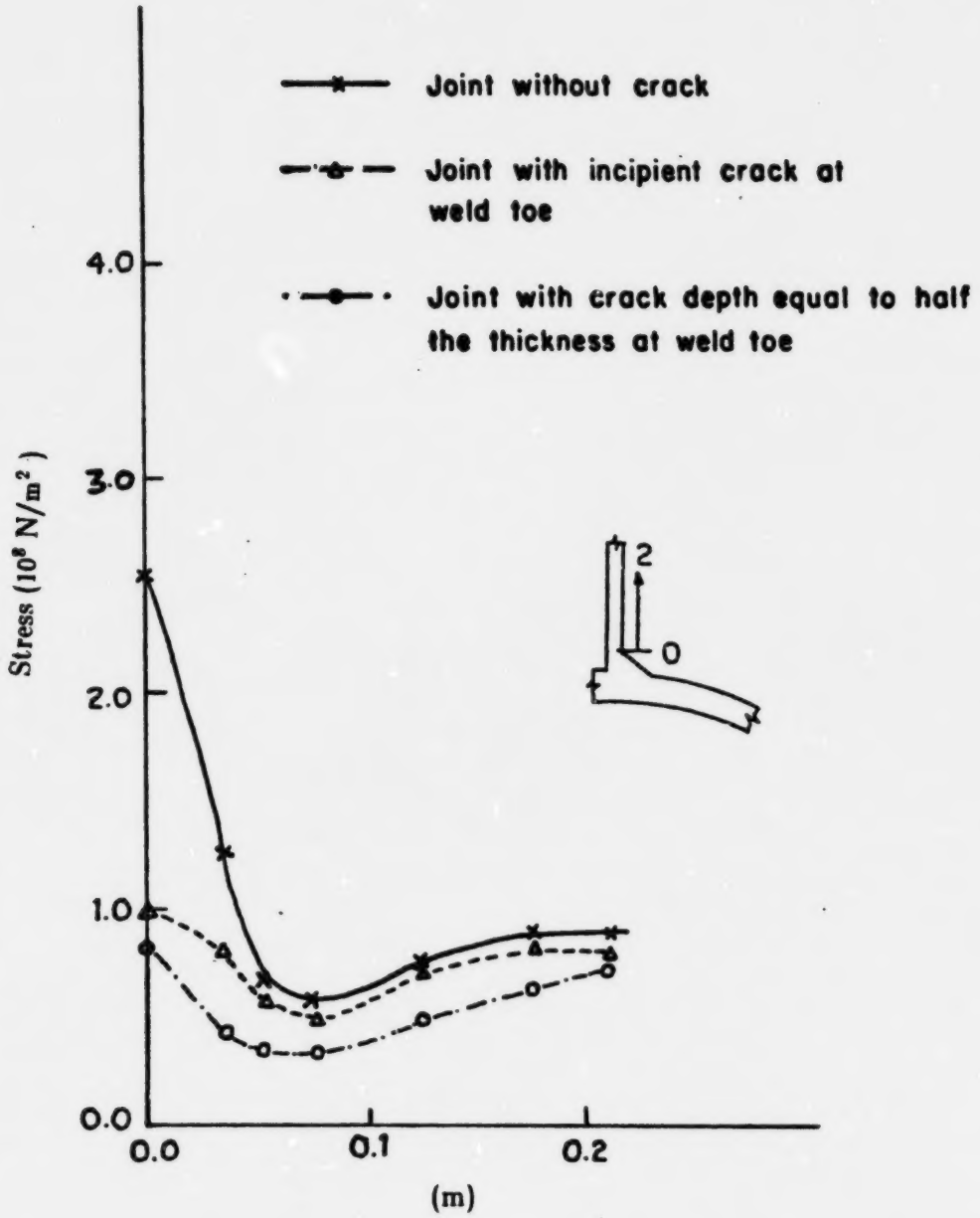

FIG. 5.6b STRESS VARIATION ALONG BRACE SURFACE AT SADDLE POINT IN PRESENCE OF SHALLOW WELD TOE CRACK DUE TO AXIAL LOAD (WITH PLUG)

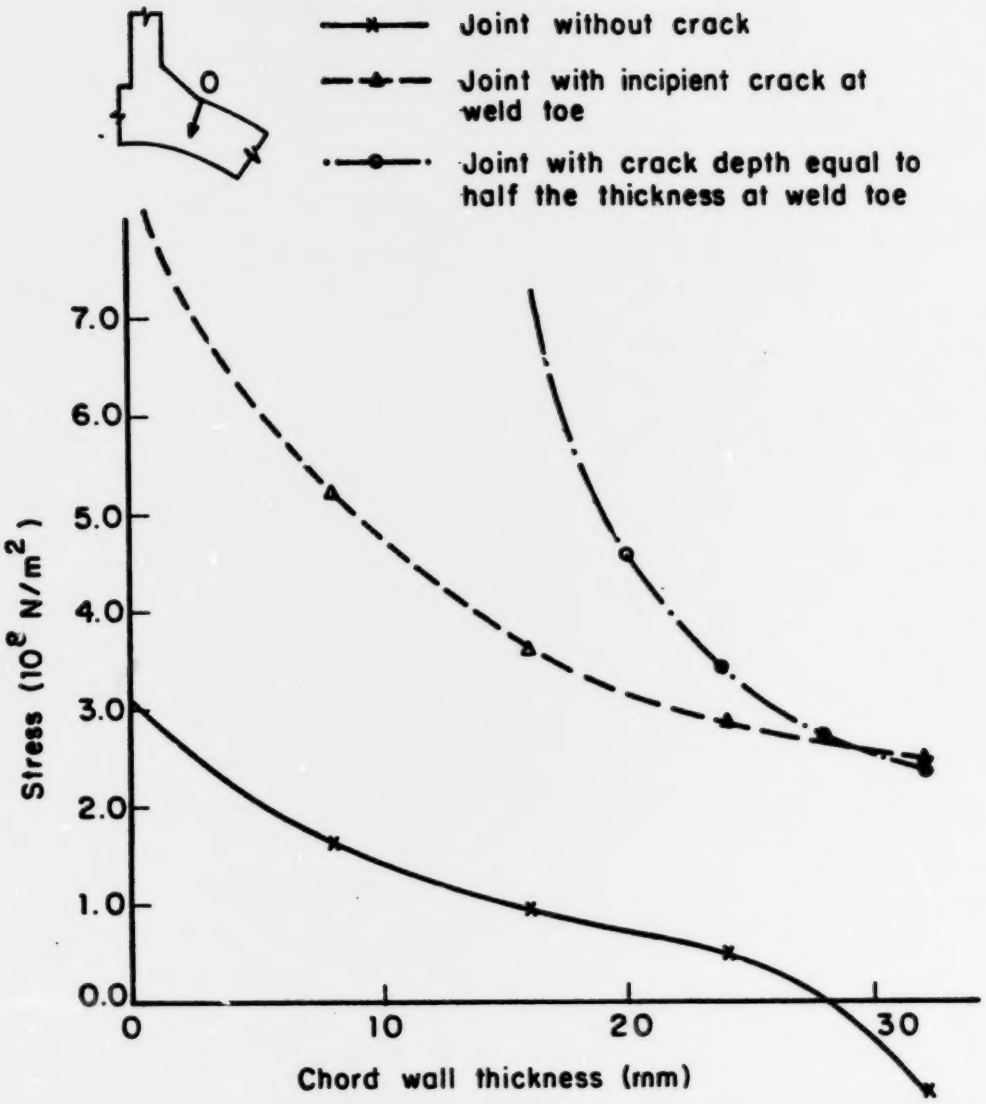

FIG. 5.7a THROUGH THICKNESS STRESS VARIATION IN FRONT OF SHALLOW WELD TOE CRACK AT SADDLE POINT DUE TO AXIAL LOAD (WITHOUT PLUG)

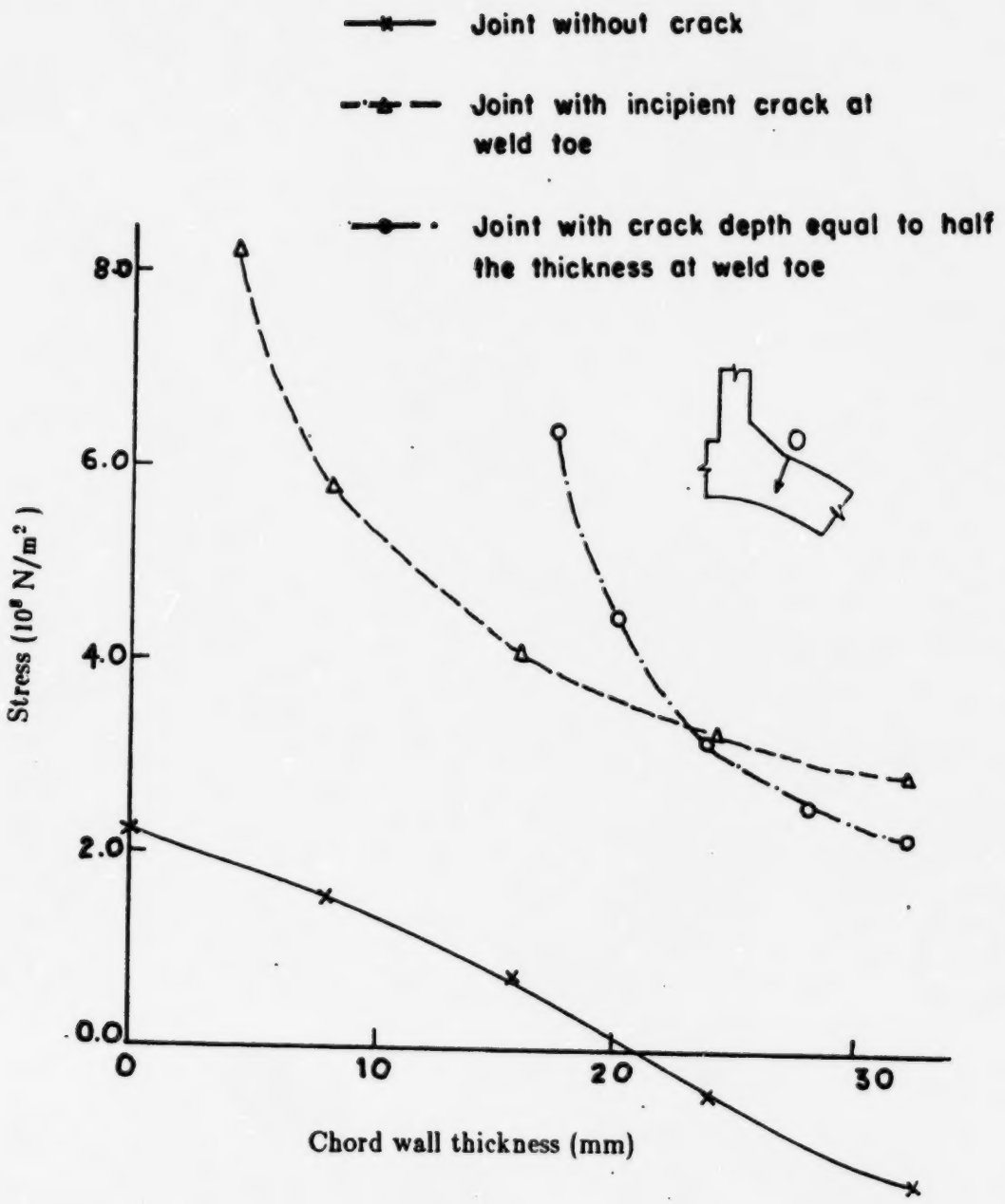

FIG. 5.7b THROUGH THICKNESS STRESS VARIATION IN FRONT OF SHALLOW WELD TOE CRACK AT SADDLE POINT DUE TO AXIAL LOAD (WITH PLUG)

for the case of finite depth crack, is very much less compared to the other two cases and is nearly same in regions away from the weld toe.

Fig. 5.7 shows the stress variation across the thickness of the chord at the weld toe (saddle point). For the joint without the crack, the stress is tensile at the outer surface and compressive at the inner surface. The presence of the crack changes the stress field into entirely tensile stress field.

The effects of shallow weld toe cracks at crown point on stress redistribution due to in-plane bending load of 10^5N at the brace are studied. The crack dimensions are same as in case of previous analysis. Fig. 5.8 shows the stress distribution along line 3 for both cracked and uncracked joints. In case of incipient crack, stresses along the chord surface are slightly greater than that of joint without crack. The stress distribution in presence of crack with depth equal to half the thickness, follows the same pattern as the incipient crack. Near the weld toe, the stress decreases due to the presence of free surface of the crack face. This agrees well with the phenomenon of hot spot strain drop observed during fatigue testing of the tubular joints, reported in the literature [51].

The stress variation along brace surface at the crown point is shown in Fig. 5.9. Near the weld toe region, the stress variation in presence of incipient crack is less than that of joint without crack. In case of finite depth crack, the magnitude of stress is higher than other two cases in the region away from the weld toe. Fig. 5.10 shows the through thickness stress variation across the chord wall in front of the weld toe crack at crown point. The stress across the thickness is much higher in case of cracked joints compared to the uncracked joint and is entirely tensile.

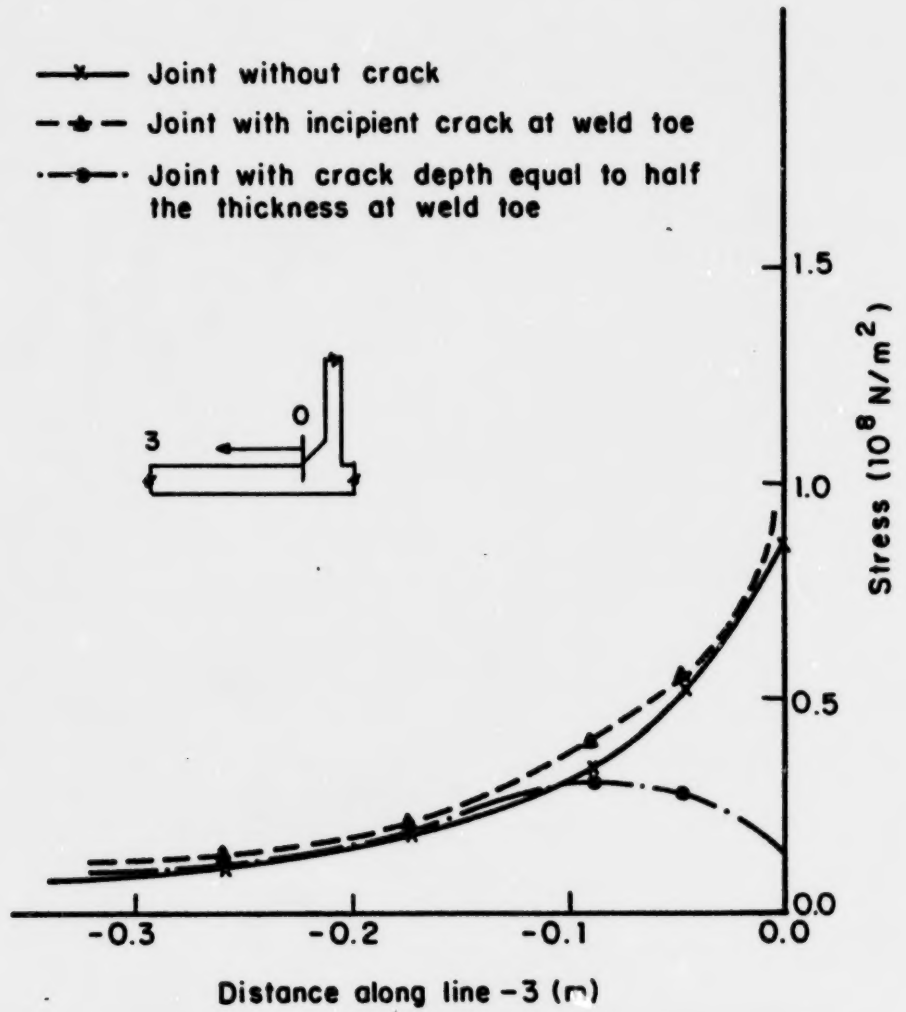

FIG. 5.8a STRESS VARIATION ALONG CHORD SURFACE AT CROWN POINT IN PRESENCE OF SHALLOW WELD TOE CRACK DUE TO IN-PLANE BENDING LOAD (WITHOUT PLUG)

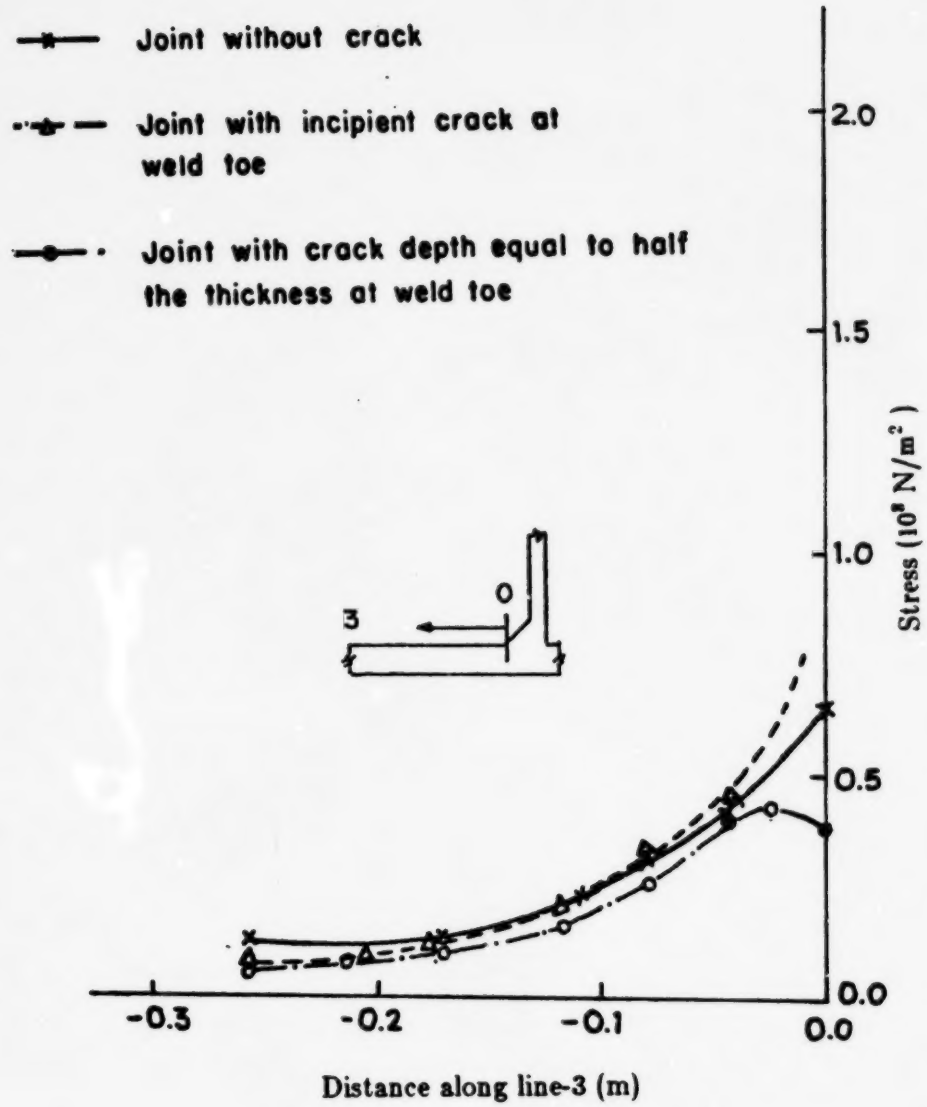

FIG. 5.8b STRESS VARIATION ALONG CHORD SURFACE AT CROWN POINT IN PRESENCE OF SHALLOW WELD TOE CRACK DUE TO IN-PLANE BENDING LOAD (WITH PLUG)

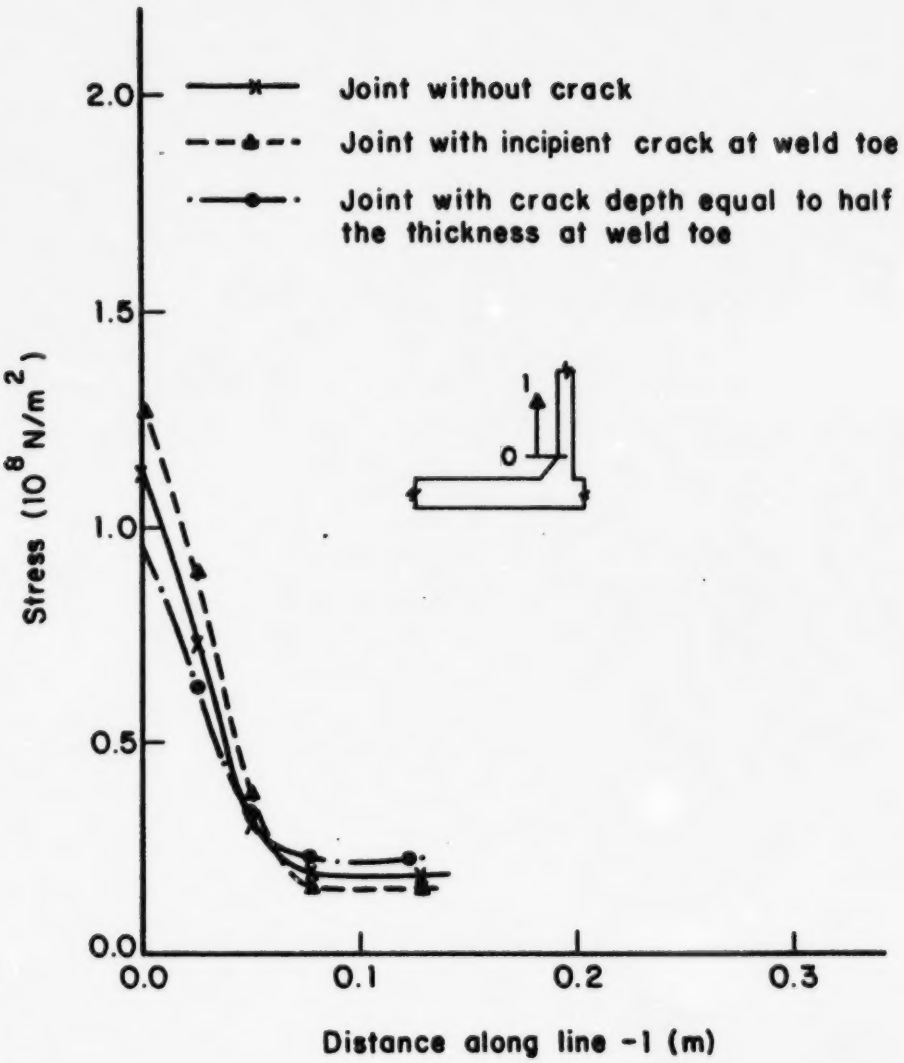

FIG. 5.9a STRESS VARIATION ALONG BRACE SURFACE AT CROWN POINT IN PRESENCE OF SHALLOW WELD TOE CRACK DUE TO IN-PLANE BENDING LOAD (WITHOUT PLUG)

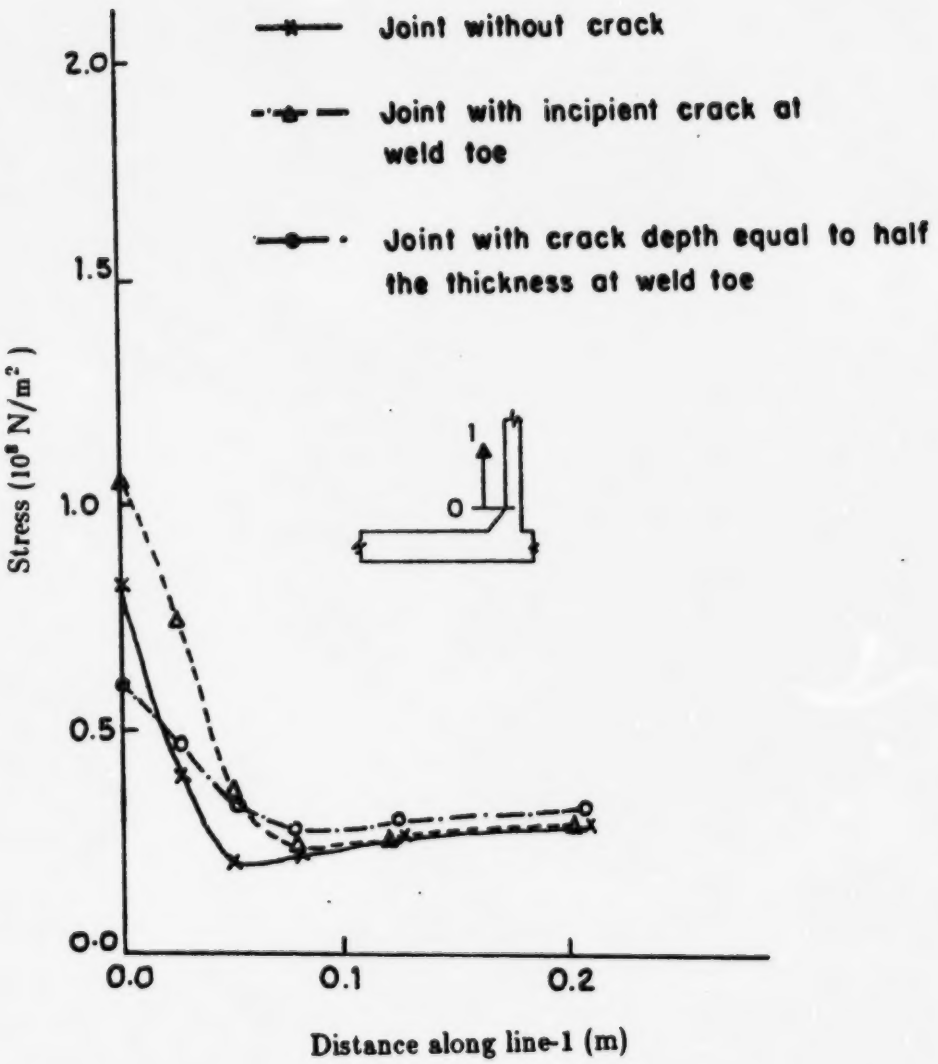

FIG. 5.9b STRESS VARIATION ALONG BRACE SURFACE AT CROWN POINT IN PRESENCE OF SHALLOW WELD TOE CRACK DUE TO IN-PLANE BENDING LOAD (WITH PLUG)

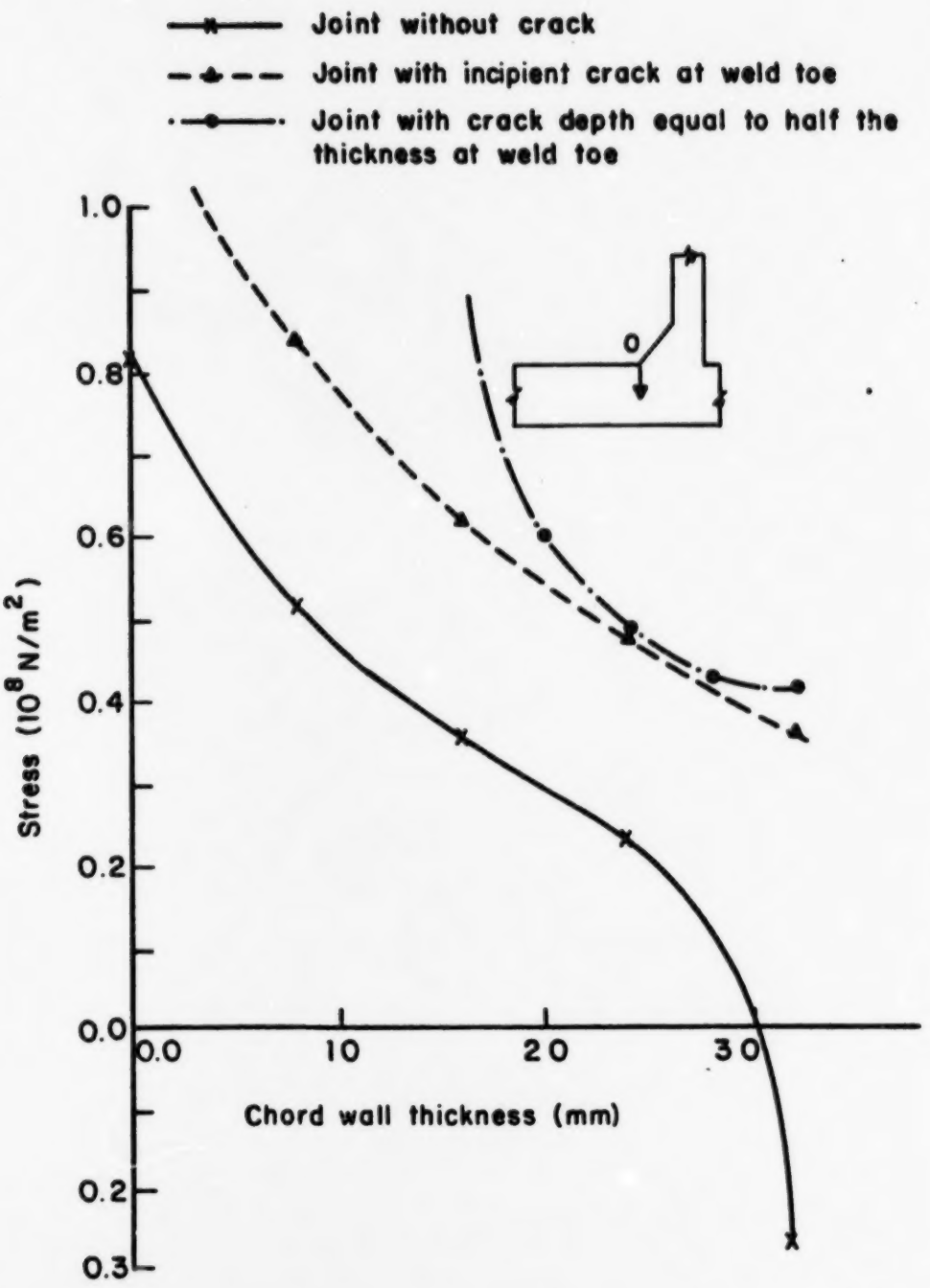

FIG. 5.10a THROUGH THICKNESS STRESS VARIATION IN FRONT OF SHALLOW WELD TOE CRACK AT CROWN POINT DUE TO IN-PLANE BENDING LOAD (WITHOUT PLUG)

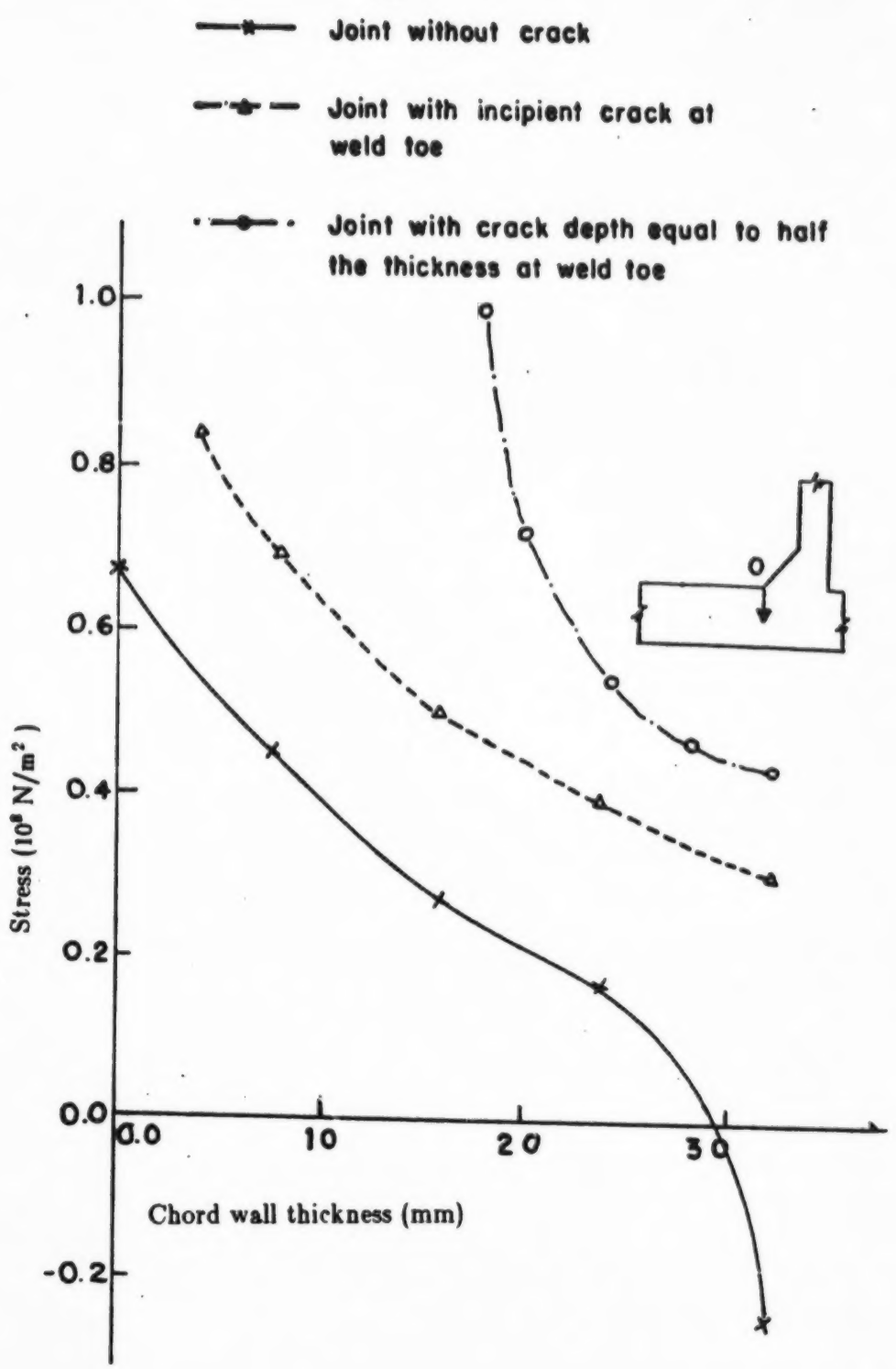

FIG. 5.10b THROUGH THICKNESS STRESS VARIATION IN FRONT OF SHALLOW WELD TOE CRACK AT CROWN POINT DUE TO IN-PLANE BENDING LOAD (WITH PLUG)

CHAPTER VI

6. CONCLUSIONS

The work described in this report utilizes the finite element program, together with a mesh generator to analyse the welded tubular T-joints.

Results using 2-dimensional and 3-dimensional finite element analyses are presented for axial load of 10^6N and 10^5 N in-plane bending load, applied at brace.

The analyses are done for joints, with and without plug stiffness.

The stress concentration factors in the chord side obtained from 2-dimensional analysis show good agreement with the measured values reported in the literature. Some difference has been observed between the brace side SCF's and the measured values, which can be justified due to the displaced brace/chord intersection. The modified SCF's on brace side, based on Irvine's recommendation, are comparable with the reported experimental values.

Using force and displacement methods, the brace-chord intersection region including weld at the saddle point is analysed for axial load case. The imposed boundary values at the plate-to-solid element transition zone are obtained from the 2-dimensional analysis.

The stresses obtained from the rezoned analysis differ from three dimensional analysis of the entire joint. The deviation in the stresses is due to the plate to solid transition boundary effect.

Three dimensional stress analyses of the entire joint are done having assumed an idealized shape of the weld reinforcement. For the chord side both two and three dimensional analyses give similar variation of stresses as reported in the literature. In the case of joint, without plug, the hot spot stress concentration factors at saddle point in the chord side is 20% higher than that obtained from two dimensional analysis. But in the brace side it is 3% higher than the two dimensional analysis results.

In the case of joint with plug, the stresses near the weld are less compared to the joint without plug. Because of the extra stiffness contribution from the plug, magnitude of the stress concentration is less compared to the joint without plug.

Along the weld surface, the stress decreases from chord weld toe up to certain point and then starts increasing and reaches a maximum value at the brace weld toe. This variation agrees well with the reported results.

A rapid decrease in stress across the weld leg is observed in contrast to the nearly constant value through the brace wall at the saddle point in case of axial load and at the crown point in case of in-plane bending.

Results using 3-dimensional finite element analyses of the cracked joint are presented for i) incipient and ii) shallow weld toe cracks, at saddle and crown points for axial and in-plane bending load cases respectively. The depth and length of shallow crack are assumed as half the thickness of chord wall and 80 mm respectively.

It is observed that in presence of incipient crack at saddle point, the stress near the weld toe due to axial loading is about twice that of the joint without a crack. In the case of shallow crack, the stresses away from the weld toe on the chord surface are slightly more compared to that due to incipient crack. But near the weld toe, the stresses decrease considerably due to the presence of free surface of crack face and are less than that of uncracked joint.

The stresses along the brace at saddle point, away from the weld toe, are approximately the same for all cases i.e. joints with incipient or shallow crack and without any crack. But near to weld toe, stress magnitude is lowest for joint with shallow crack and highest in the case of uncracked joint.

The trend of surface stress variation along the chord, in presence of cracks, at crown point due to in-plane bending is similar to that at saddle point due to axial loading. But along the brace side, the stress at weld toe in case of uncracked joint, is higher than that of joint with shallow crack but less than that of joint with incipient crack.

The stresses across the chord wall (in front of the cracks) are much higher than that of joint without crack at both saddle and crown points. At the vicinity of incipient and shallow cracks, the stresses are high and approximately of the same magnitude.

The reported formulation of problem to analyze the tubular joints with shallow weld toe crack can be utilized to determine the stress intensity factor and hence to predict the fatigue life of the joint using linear fracture mechanics approach.

REFERENCES

1. Hoffman, Robert E., "Interactive Graphics Finite Element Mesh Generation", Computing in Civil Engineering, pp. 700-713, 1983.

2. Bousquet, R. D. and Yates, D. N., "A Low Cost Interactive Graphics System for Large Scale Finite Element Analysis", Computers and Structures, Vol. 3, pp. 1321-1330, 1973.

3. Durocher, Lawrence L., "A Versatile Two-Dimensional Mesh Generator with Automatic Bandwidth Reduction", Computers and Structures, Vol. 10, pp. 561-575, 1979.

4. Felippa, Carlos A., "An Alphanumeric Finite Element Mesh Plotter", Int. Journal for Numerical Methods in Engineering, Vol. 5, pp. 217-236, 1972.

5. Adamek, James R., "An Automatic Mesh Generator Using Two and Three-Dimensional Isoparametric Finite Elements", Master's Thesis, Naval Postgraduate School, California, 1973.

6. William J. Gordon and Charles A. Hall, "Construction of Curvilinear Co-ordinate Systems and Application to Mesh Generation", Int. Journal for Numerical Methods in Engineering, Vol. 7, pp. 461-477, 1973.

7. Clough, Ray W. and Tocher, James L., "Finite Element Stiffness Matrices for Analysis of Plate Bending", Conference on Matrix Methods in Structural Mechanics, Wright-Patterson Air Force Base, Ohio, 1965.

8. Ahmad, S., Irons, Bruce M. and Zienkiewicz, O. C., "Analysis of Thick and Thin Shells Structures by Curved Finite Elements", Int. Journal for Numerical Methods in Engineering, Vol. 2, pp. 419-415, 1970.

9. Clough, Ray W. and Johnson, C. Phillip, "A Finite Element Approximation for the Analysis of Thin Shells", Int. Journal of Solids and Structures, Vol. 4, pp. 43-60, 1968.

10. Liaw, C. Y., Litton, R. W. and Reimer, R. B., "Improved Finite Elements for Analysis of Welded Tubular Joints", Proc. Offshore Technology Conference, Paper No. 2642, Houston, Texas, 1976.

11. Miller, C. D. and Trammell, J. H., "An Analytical and Experimental Study of Stiffened Tubular Joints with Multiple Branches", Proc. Offshore Technology Conference, Paper No. 2101, Houston, Texas, 1974.

12. Radenkovic, D., "Stress Analysis in Tubular Joints", Proc. of International Conf., Special and Plenary Sessions, STeel in Marine Structures, Paris, 1980.

13. Greimann, L. F., DeHart, R. C. and Blackstone, W. R., "Finite Element Analysis of Complex Joints", Proc. Offshore Technology Conference, Paper No. 1823, Houston, Texas, 1973.

14. Shiyekar, M. R., Kalani, M. and Belkune, R. M., "Stresses in Stiffened Tubular T Joint of an Offshore Structure", Proc. of the first Offshore Mechnics/Artic Engineering/Deepsea Systems Symposium, Vol. 1, New Orleans, 1982.

15. Robert, E. Hoffman, Earl and Wright, "The Accuracy of Different Finite Element Types of the Analysis of Complex, Welded Tubular Joints", Proc. of the Offshore Technology Conference, Houston, 1980.

16. Kassir, M. K. and Sih, G. C., "Three Dimensional Stress Distribution Around an Elliptical Crack Under Arbitary Loadings", Journal of Applied Mechanics, Vol. 33, No. 3, pp. 601-611, Sept. 1966.

17. Hartranft, R. J. and Sih, G. C., "The Use of Eigen Function Expansions in the General Solution of Three-Dimensional Crack Problems", Journal of Mathematics and Mechanics, Vol. 19, No. 2, pp. 123-138, Aug. 1969.

18. Sih, G. C., "A Review of the Three-Dimensional Stress Problem for a Cracked Plate", Int. Journal of Fracture Mechanics, Vol. 7, No. 1, pp. 39-61, 1971.

19. Tracey, D. M., "Finite Elements for Three Dimensional Elastic Crack Analysis", Nuclear Engineering and Design, North-Holland Publishing Company, No. 26, pp. 282-290, 1974.

20. Dennis M. Tracey, "Finite Elements for Determination of Crack Tip Elastic Stress Intensity Factors", Engineering Fracture Mechanics, Vol. 3, pp. 255-265, 1971.

21. Raju, I. S. and Newman, Jr. J. C., "Three-Dimensional Finite Element Analysis of Finite-Thickness Fracture Specimens", National Aeronautics and Space Administration Technical Note, May 1977.

22. Blackburn, W. S., and Hellen, T. K., "Calculation of Stress Intensity Factors in Three Dimensions by Finite Element Methods", Int. Journal for Numerical Methods in Engineering, Vol. 11, pp. 211-229, 1977.

23. Alwar, R. S. and Ramachandran, D. N., "Three-Dimensional Finite Element Analysis of Cracked Thick Plates in Bending", Int. Journal for Numerical Methods in Engineering, Vol. 19, pp. 293-303, 1983.

24. Stern Morris and Becker Eric B., "A Conforming Crack Tip Element with Quadratic Variation in the Singular Fields", Int. Journal for Numerical Methods in Engineering, Vol. 12, pp. 279-288, 1978.

25. Kuo-Kuang Hu, Chen-Ming J. Huang and Stuart E. Swartz, "Finite Element Model to Determine K_I", Journal of Engineering Mechanics, Vol. 109, No. 4, Aug. 1983.

26. William, M. L., "On the Stress Distribution at the Base of a Stationary Crack", Journal of Applied Mechanics, ASME, Vol. 24, 1957.

27. Bell, R. and Kirkhope, J., "Determination of Stress Intensity Factors for Weld Toe Defects", D.S.S. Contract OSU82-00233, CANMET, 1984.

28. Barsoum, R. S., "On the Use of Isoparametric Finite Elements in Liner Fracture Mechanics", Int. Journal of Numerical Methods Engineering, 10-1, 1976.

29. Scordelis, A. C. and Lo, K. S., "Computer Analysis of Cylindrical Shells", J. Am. Concr. Inst., 61, May 1964.

30. Irvine, N. M., "Comparison of the Performance of Modern Semi-empirical Parametric Equations for Tubular Joint Stress Concentraton Factors", Proc. of International Conf., Special and Plenary Sessions, Steel in Marine Structures, Paris, 1981.

31. Clayton, A. M., Martin, T., "Comparison of Stress Levels Obtained on Some Early Welded T-joint Tests", Interim Technical Report, 2/07, UKOSRP, 1980.

32. Wordsworth, A. C. and Smedly, G. P., "Stress Concentrations at Unstiffened Tubular Joints", Paper 31, European Offshore Steels Research Seminar, The Welding Institute, 1978.

33. Gibstein, M. B., "Parametric Stress Analysis of T-Joints", Paper 26, European Offshore Steel Reserch Seminar, The Welding Institute, 1978.

34. Kuang, A. B. et al, "Stress Concentration in Tubular Joints", Pet. Eng. Journal, pp. 287-299, Aug. 1977.

35. Marshall, P. W., "Connections for Welded Tubular Structures", Proc. of the Second International Conference on Welding of Tubular Structures, Boston, 1984.

36. Bell, R., Kirkhope, J. and Vosikovsky, O., "Stress Intensity Factors at Weld Toe Cracks", Proc. of the Specialty Conference on Computer Methods in Offshore Engineering, CSCE, Halifax, 1984.

37. Irvine, N. M., "Comparison of Stress Analysis Methods in the Region of Chord/Brace Intersection", Interim Technical Report, 2/08, UKOSRP, 1980.

38. Parkhouse, J. C., "Improved Modelling of Tube Wall Intersections Using Brick Elements", Proc. of Intc. Conference, Steel in Marine Structures, Paris, 1981.

39. Morgan, E. F., "Use of High Order Isoparametric Solid Finite Elements for the Stress Analysis of Welded Tubular Joints", Southwest Reserach Institute, Project 03-9217-001, Texas, 1979.

40. Clayton, A. M. and Parkhouse, J. G., "The Stress Analysis of a Large Diameter Brace T-joint", Interim Technical Report, 2/01, UKOSRP, 1980.

41. Dutta, D., Mang, F. and Wardenier, J., "Fatigue Behaviour of Welded Hollow Section Joints", CIDECT, Monograph, No. 7, Constrado, Croydon, 1982.

42. Shinners, C. D. and Abel, A., "The Fatigue Behaviour of Large Scale As-Welded and Stress Relieved Tubular T-joints", Proc. of the First Offshore Mechanics/Artic Engineering/Deepsea Systems Symposium, Vol. 1, New Orleans, 1982.

43. Trantina, G. G., deLorenzi, H. G. and Wilkening, W. W., "Three-Dimensional Elastic-Plastic Finite Element Analysis of Small Surface Cracks", Engineering Fracture Mechanics, Vol. 18, No. 5, pp. 925-938, 1983.

44. Albrecht Pedro and Yamada Kentaro, "Rapid Calculation of Stress Intensity Factors", Journal of the Structural Division, ASCE, Feb. 1977.

45. Cartwright, D. J. and Rooke, D. P., "Evaluation of Stress Intensity Factors", Journal of Strain Analysis, Vol. 10, No. 4, 1975.

46. Theocaris, P. S., Theotokoglou, E. E. and Tsamasphyros, G., "A Relaxation Technique for Evaluating Stress Intensity Factors by the Finite Element Method", Int. Journal for Numerical Methods in Engineering, Vol. 19, pp. 17-26, 1983.

47. Sahrmann, G. J. and Szaboo, B. A., "Analysis of Fatigue Crack and Growth in a Tubular Joint Weldment Using the P-Version of the Finite Element Method", Proc. Third Int. Offshore Mechanics and Arctic Engineering Symposium, New Orleans, Louisiana, 1984.

48. Dijkstra, O. D. and Back, J. de, "Fatigue Strength of Tubular T- and X- Joints", Proc. Offshore Tech. Conf., OTC 3696, Houston, Texas, 1980.

49. Claude J. Putot, Michel, L., Truchon and Quoc S. Nguyen, "Use of Fracture Mechnics in Tubular Connections Fatigue Crack Growth", Proc. Offshore Tech. Conf., OTC 3701, Houston, Texas, 1980.

50. Bathe, K. J., "Finite Element Procedures in Engineering Analysis", Prentice-Hall, Inc., New Jersey, 1982.

51. Back, de and Vaessen, G.H.G., "Fatigue and Corrosion Fatigue Behaviour of Offshore Steel Structures", ECSC Convention 7210-KB/6/602 J.7.1f/76, Final Report, Delft, April, 1981.